Title

Element Diffusion and Other Mixing in White Dwarf Stars

Permalink

https://escholarship.org/uc/item/7rg1j2qq

Author

Bauer, Evan

Publication Date

2019

Peer reviewed|Thesis/dissertation

UNIVERSITY of CALIFORNIA
Santa Barbara

Element Diffusion and Other Mixing in White Dwarf Stars

A dissertation submitted in partial satisfaction of the
requirements for the degree of

Doctor of Philosophy

in

Physics

by

Evan B. Bauer

Committee in charge:

Professor Lars Bildsten, Chair

Professor Omer Blaes

Professor Timothy Brandt

June 2019

The dissertation of Evan B. Bauer is approved:

Professor Omer Blaes

Professor Timothy Brandt

Professor Lars Bildsten, Chair

May 2019

Dedicated to the memory of Edna Eileen Bauer, 1926–2019

Acknowledgements

I'd like to start by thanking the astrophysics faculty at UCSB. Lars Bildsten has been a wonderfully supportive advisor. I am grateful for the dedication, patience, and enthusiasm that he always shared as he guided me through years of fascinating projects. I am also grateful to Omer Blaes, Ben Mazin, and Tim Brandt for serving on my advisory committee at various times and making themselves available to offer professional and academic advice throughout my time as a graduate student. Their individualized advice and varying perspectives have been invaluable in navigating the path toward completing this work. Peng Oh, Crystal Martin, and Gary Horowitz taught particularly memorable classes. I thank them for their insight and energy that made lectures and homework assignments stimulating puzzles rather than drudgery.

I also want to thank my fellow graduate students in the UCSB Physics program. It has been a privilege to work through graduate school with the friendship and support of Lucas Brady, Dan Ish, Michael Swift, Darren Valovcin, Kevin Singh, Blake Wilson, and many others. I also relied on the expertise of Bill Wolf and Jared Brooks for my first several years in the research group that would become my home. I couldn't have made the transition into astrophysics and computational work without their patient guidance. It has also been a pleasure to learn from and share an office with Griffin Hosseinzadeh, Stephanie Ho, Suoqing Ji, Jared Goldberg, and Will Schultz.

My graduate work has relied heavily on the team that develops and supports the `MESA` code base. I'm deeply grateful to the entire `MESA` team, and especially to Josiah Schwab, Bill Paxton, and Frank Timmes. I am inspired by the `MESA` team's commitment to open-source software and reproducibility as a cornerstone of computational science, and by the hard work and genius they apply in support of those ideals. I am grateful for the opportunity to make contributions to the `MESA` project as part of my graduate work. Josiah has also been a close collaborator, and he made crucial contributions to several portions of the work that appears in this dissertation.

I am grateful to many professors that inspired a love of physics and math during my time as an undergraduate at Baylor. Lance Littlejohn cheerfully welcomed me into classes in the math department long before I thought I could belong there. David Ryden, Edward Burger, Brian Raines, and Johnny Henderson taught delightful and challenging classes that always left students eager to continue learning. In the physics department, Lorin Matthews, Greg Benesh, Wickramasinghe Ariyasinghe, and many others provided outstanding instruction to my small cohort of physics majors. I am especially grateful to Kenichi Hatakeyama and Jay Dittmann, who found space for me to participate in projects with their research group. I thoroughly enjoyed the new experiences and challenges presented by the two summers of full-time research that I was able to pursue under their supervision. I would have been in no position to pursue graduate work in physics without the many hours they dedicated to mentoring me. Beyond the physics and math departments, I also received guidance and support from the Honors College at Baylor that shaped my thinking about academic work. Alden Smith, Scott Moore, Elizabeth and David Corey, Phillip Donnelly, Al Beck, and Thomas Hibbs each encouraged me to find joy in engaging with disciplines outside of my majors. The community that they built in the Honors College fostered a love of learning that transcended the confines of grades, majors, or required coursework.

Finally, I want to thank those who taught me before I even considered studying physics. My mother, Charlene Bauer, was my first teacher, but she went far beyond that. She dedicated years of her life to educating her children, and I will never be able to express my gratitude for everything she has done. My father, John Bauer, also invested a great deal of time and effort in guiding my education. I would also like to thank all those who partnered with my parents in my education, including Damian Efta, Mike Swehla, Rex Michel, Tom Slusher, and Brit Hopper. I'm especially grateful to Rick Silvey for his outstanding teaching that helped me discover an unexpected enjoyment of math in my first calculus courses, nudging me in the direction of considering physics as a major.

Curriculum Vitæ

Evan B. Bauer

Education

2019	Ph.D., Physics, University of California, Santa Barbara
2016	M.A., Physics, University of California, Santa Barbara
2013	B.A., University Scholar, Baylor University

Publications

"Modules for Experiments in Stellar Astrophysics (MESA): Binaries, Pulsations, and Explosions," Bill Paxton, Pablo Marchant, Josiah Schwab, **Evan B. Bauer**, et al. *The Astrophysical Journal Supplement Series* 220, 15 (2015)

"Electron Captures on ^{14}N as a Trigger for Helium Shell Detonations," **Evan B. Bauer**, Josiah Schwab, and Lars Bildsten *The Astrophysical Journal* 845, 97 (2017)

"Modules for Experiments in Stellar Astrophysics (MESA): Convective Boundaries, Element Diffusion, and Massive Star Explosions," Bill Paxton, Josiah Schwab, **Evan B. Bauer**, et al. *The Astrophysical Journal Supplement Series* 234, 34 (2018)

"Variability of Red Supergiants in M31 from the Palomar Transient Factory," Monika D. Soraisam, Lars Bildsten, Maria R. Drout, **Evan B. Bauer**, et al. *The Astrophysical Journal* 859, 73 (2018)

"Increases to Inferred Rates of Planetesimal Accretion due to Thermohaline Mixing in Metal-accreting White Dwarfs," **Evan B. Bauer** and Lars Bildsten *The Astrophysical Journal Letters* 859, L19 (2018)

"The Impact of White Dwarf Luminosity Profiles on Oscillation Frequencies," F. X. Timmes, Richard H. D. Townsend, **Evan B. Bauer**, Anne Thoul, C. E. Fields, and William M. Wolf *The Astrophysical Journal Letters* 867, L30 (2018)

"Polluted White Dwarfs: Mixing Regions and Diffusion Timescales," **Evan B. Bauer** and Lars Bildsten *The Astrophysical Journal* 872, 96 (2019)

Abstract

Element Diffusion and Other Mixing in White Dwarf Stars

by

Evan B. Bauer

White dwarf stars reveal signatures of material accreted from their surroundings. Making quantitative inferences about the processes that supply this material requires theoretical models of white dwarf surface structure. In this dissertation, I examine methods for building evolutionary white dwarf models that include element diffusion, convection, and thermohaline instability. Each of these mixing processes that occur at white dwarf surfaces has important implications for observable signatures of accreted material. Models that account for all types of surface mixing allow for inferences about accretion rates and composition of bodies that supply the material. The picture that emerges from models presented in this work is one of planetary systems supplying rocky debris at higher rates and from larger mass reservoirs than previously thought.

Contents

Chapter 1

Introduction

White dwarf stars (WDs) are the final evolutionary stage for the vast majority of initial stellar masses (Liebert, 1980; Fontaine et al., 2001; Hansen, 2004). Due to the strong gravity at their surfaces, isolated WDs develop stratified atmospheres with pure surface compositions and well-understood spectral features (Schatzman, 1945, 1948). When the surrounding environment of a WD contaminates its surface with heavy-element pollution, this makes the WD atmosphere an ideal spectroscopic laboratory for studying the composition of whatever supplies this polluting material (Vauclair et al., 1979). Though polluted white dwarf compositions were originally thought to originate from interstellar accretion, later observations ruled this out and instead indicated a connection to dusty debris disks (Graham et al., 1990; Koester et al., 1997; Zuckerman et al., 2003; Jura, 2003). Through decades of work on observed polluted WD systems, the emerging framework for explaining polluted WDs and their compositions points to debris from complex dynamics in planetary systems surrounding WDs (Jura & Young, 2014; Veras, 2016; Farihi, 2016). Understanding the structure of polluted WDs therefore provides a unique tool to study planetary systems that survive to the final stages of their host stars' evolution.

Interpretation of observed pollution in WDs requires detailed theoretical description of the structure and evolutionary properties of WDs. Static atmosphere models for WDs have provided much of the foundation for interpreting observations up to this point (Koester, 2009, 2010; Koester et al., 2014). In particular, detailed surface convection and element diffusion calculations have proven crucial to understanding the accretion rates for these systems. While these models have enabled a great deal of progress in identifying important trends, their usefulness can be limited by the fact that they require assuming a steady-state structure to connect observations to models. Static models struggle to account for time-dependent processes that may never reach a steady-state equilibrium, or processes that are dynamically coupled to the aspects of stellar structure that they can in turn depend upon. Thermohaline mixing is one such process, and consequently its importance had been overlooked in the context of WD pollution until recently. However, Deal et al. (2013) demonstrated that it can alter the understanding of mixing relevant for polluting metals in WD atmospheres, which in turn substantially modifies inferences about accretion rates and perhaps even the architecture of planetary systems needed to supply WD pollution.

The contents of this dissertation are aimed at expanding the set of theoretical tools and time-dependent evolutionary models available to enable further advancements in interpreting WD observations. These calculations must account for element diffusion and sedimentation along with the background structure and dynamical mixing processes present in WDs. Chapter 2 describes the fundamental physics and numerical methods that we employ for stellar evolution calculations that include element diffusion. Chapter 3 describes enhancements to these diffusion methods that specifically extend their applicability to regimes relevant for WDs. This chapter also provides a few brief diversions into important applications of element diffusion for WD structure and evolution calculations, including shell flashes and long-term sedimentation heating. Chapter 4 outlines an initial exploration of WD evolution models that account for element diffusion along with thermohaline mixing to quantify the regimes where either process might be expected to dominate. Chapter 5 then provides a more thorough investigation of models that account for the effects of all these relevant mixing processes and discusses the broad implications of the new inferences for accretion rates that these models require. This chapter also provides detailed tabulations of results intended to maximize the potential for connecting observations to the predictions of our evolutionary models. Chapter 6 explores a different topic related to WD evolution calculations: the reactions that trigger detonations in massive helium shells on WDs that accrete from from helium subdwarf companions.

1.1 Software

This work makes extensive use of the open-source software instrument `MESA` (Modules for Experiments in Stellar Astrophysics). We often refer to the instrument papers describing the `MESA` software capabilities using roman numerals: Paxton et al. (2011, MESA I), Paxton et al. (2013, MESA II), Paxton et al. (2015, MESA III), Paxton et al. (2018, MESA IV), and Paxton et al. (2019, MESA V). The `MESAstar` stellar evolution module is built on a number of fundamental physics modules that we summarize briefly here. The `MESA` equation of state (EOS) is a blend of the OPAL (Rogers & Nayfonov, 2002), SCVH (Saumon et al., 1995), PTEH (Pols et al., 1995), HELM (Timmes & Swesty, 2000), and PC (Potekhin & Chabrier, 2010) EOSes. Radiative opacities are primarily from OPAL (Iglesias & Rogers, 1993, 1996), with low-temperature data from Ferguson et al. (2005) and the high-temperature, Compton-scattering dominated regime by Buchler & Yueh (1976). Electron conduction opacities are from Cassisi et al. (2007). Nuclear reaction rates are from JINA REACLIB (Cyburt et al., 2010) plus additional tabulated weak reaction rates (Fuller et al., 1985; Oda et al., 1994; Langanke & Martínez-Pinedo, 2000). Screening is included via the prescription of Chugunov et al. (2007). Thermal neutrino loss rates are from Itoh et al. (1996). The `MESAbinary` module can include multiple instances of `MESAstar` models with mass transfer rates in Roche lobe overflowing binary systems determined using the prescription of Ritter (1988). Roche lobe radii are computed using the fit of Eggleton (1983).

1.2 Permissions and Attributions

1. The content of Chapter 2 is adapted and reproduced from Paxton et al. (2015) with permission from *The Astrophysical Journal Supplement Series*.

2. The content of Chapter 3 and Appendices A and B is adapted and reproduced from Paxton et al. (2018) with permission from *The Astrophysical Journal Supplement Series* and Josiah Schwab, who made substantial contributions to the content in Appendix B.

3. The content of Chapter 4 is adapted and reproduced from Bauer & Bildsten (2018) with permission from *The Astrophysical Journal Letters*.

4. The content of Chapter 5 and Appendix C is adapted and reproduced from Bauer & Bildsten (2019) with permission from *The Astrophysical Journal*.

5. The content of Chapter 6 is adapted and reproduced from Bauer et al. (2017) with permission from *The Astrophysical Journal* and Josiah Schwab, who contributed most of the content found in Section 6.1.1.

My graduate work has also afforded me opportunities to participate in exciting research efforts led by others (Soraisam et al., 2018; Timmes et al., 2018), but that work does not appear in this dissertation.

Chapter 2

Element Diffusion Methods for Stellar Evolution Models

`MESA`'s early implementation of microscopic element diffusion incorporated the approach used by Thoul et al. (1994) in their seminal work on understanding the sedimentation of helium in the solar interior. The fundamental starting point for this treatment of diffusion is the Boltzmann equation with the assumption of binary collisions where the particle's mean free path is much larger than the average particle spacing. This formalism, encoded in the Burgers equations (Burgers, 1969), assumes that ions interact with an effective potential that governs isolated interactions between only two particles at a time. For more strongly coupled plasmas, as $\Gamma \approx e^2/(\lambda_{\rm ion} k_{\rm B} T)$ exceeds unity (where $\lambda_{\rm ion} = (3/4\pi n_{\rm ion})^{1/3}$ is the mean inter-ion spacing, and $n_{\rm ion}$ is the total ion number density), it is no longer clear that this assumption remains valid. Later updates to `MESA` incorporated the work of Hu et al. (2011) on radiative levitation and incorporated the resistance coefficients calculated by Paquette et al. (1986a) for approaches to the denser plasma regime as $\Gamma \rightarrow 1$.

Here we describe `MESA`'s implementation of element diffusion and then discuss the path forward for diffusion implementations in the $\Gamma > 1$ regime, needed for accurate studies of diffusion in the interiors of white dwarfs or surfaces of neutron stars.

2.1 Methods in `MESAstar`

We now describe the formalism and assumptions underlying the approach to diffusion employed by `MESA`. This is followed by a discussion of the framework for numerical implementation of this formalism provided by Thoul et al. (1994) and key modifications present in the `MESA` diffusion routine.

2.1.1 Burgers Equations

The Burgers equations for diffusion in an ionized plasma are derived using the Boltzmann equation for the distribution function $F_s(\mathbf{x}, \boldsymbol{\xi}, t)$ for particles of type s

$$\frac{\partial F_s}{\partial t} + \sum_i \xi_i \frac{\partial F_s}{\partial x_i} + \sum_i \frac{f_{si}}{m_s} \frac{\partial F_s}{\partial \xi_i} = \left(\frac{dF_s}{dt} \right)_{\text{collision}}, \tag{2.1}$$

where x_i are the components of the position vector, ξ_i are the components of the velocity vector, f_{si} are components of the forces on particles of type s, and m_s is the mass for those particles. Throughout this section, the indices s and t refer to particle species, while i and j are used to index other quantities such as spatial components of vectors.

Burgers adopts the 13-moment approximation due to Grad (1949) as a closure scheme for taking moments of the Boltzmann equation. Burgers also assumes an approximately Maxwellian distribution function

$$F_s = \frac{n_s}{\pi^{3/2} a_s^3} \exp\left(\frac{-c_s^2}{a_s^2}\right)(1+\phi_s), \tag{2.2}$$

where $a_s = (2k_{\mathrm{B}}T/m_s)^{1/2}$, $c_{si} = \xi_i - u_{si}$ represents the components of the deviation of the velocity from the mean flow velocity $\mathbf{u}_s$ of the species, and

$$\phi_s = \sum_{i,j} B_{sij} c_{si} c_{sj} + \sum_i C_{si}\left(c_s^2 - \frac{5}{2}a_s^2\right) c_{si} \tag{2.3}$$

is the small deviation ($\phi_s \ll 1$) from the Maxwellian distribution. The coefficients B_{sij} and C_{si} are defined such that the distribution function has a total of 13 free parameters corresponding to the 13 moments of the closure scheme (see Burgers, 1969).

Burgers derives the collision integrals ($S_{st}^{(l)}$) and cross-sections ($\Sigma_{st}^{(lj)}$) that result from taking moments of the right hand side of the Boltzmann equation

$$S_{st}^{(l)} = 2\pi \int_0^\infty (1 - \cos^l \chi_{st}) b\, db, \tag{2.4}$$

$$\Sigma_{st}^{(lj)} = \frac{4\pi}{\pi^{3/2}} \int_0^\infty dv \, \exp\left(\frac{-v^2}{\alpha_{st}^2}\right) \frac{v^{2j+3}}{\alpha_{st}^{2j+4}} S_{st}^{(l)}, \tag{2.5}$$

where $\alpha_{st}^2 = 2k_{\mathrm{B}}T/\mu_{st}$, $\mu_{st} = m_s m_t/(m_s + m_t)$, v represents the relative velocity of colliding particles, and the angle of deviation χ_{st} is a function of both v and the impact parameter b that depends on the physics of the two-particle interaction between colliding particles in the gas. Burgers then defines the dimensionless coefficients z_{st}, z'_{st}, z''_{st}, and

z'''_{st}, along with resistance coefficients (K_{st}) in terms of the collision integrals:

$$\begin{aligned} K_{st} = K_{ts} &= \frac{2}{3} n_s n_t \mu_{st} \alpha_{st} \Sigma^{(11)}_{st}, \\ \Sigma^{(12)}_{st}/\Sigma^{(11)}_{st} &= \frac{5}{2}(1 - z_{st}), \\ \Sigma^{(13)}_{st}/\Sigma^{(11)}_{st} &= \frac{25}{4} - \frac{25}{2} z_{st} + \frac{5}{2} z'_{st}, \\ \Sigma^{(22)}_{st}/\Sigma^{(11)}_{st} &= z''_{st}, \\ \Sigma^{(23)}_{st}/\Sigma^{(11)}_{st} &= z'''_{st}. \end{aligned} \tag{2.6}$$

In the “single-fluid picture” the diffusion velocities are defined with reference to the mean velocity of the gas as a whole ($\mathbf{u}$), rather than with respect to the mean species velocity ($\mathbf{u}_s$):

$$u_{si} = \frac{1}{n_s} \int d\boldsymbol{\xi}\, \xi_i F_s, \quad \mathbf{u} = \frac{1}{\rho} \sum_s \rho_s \mathbf{u}_s, \quad \mathbf{w}_s = \mathbf{u}_s - \mathbf{u}. \tag{2.7}$$

Burgers defines residual heat flow vectors

$$r_{si} = \left(\frac{m_s}{2 n_s k_{\mathrm{B}} T} \int d^3\boldsymbol{\xi}\, (\xi_i - u_i) |\boldsymbol{\xi} - \mathbf{u}|^2 F_s \right) - \frac{5}{2} w_{si}. \tag{2.8}$$

As shown in section 18 of Burgers (1969) if we assume $|\mathbf{w}_s| \ll a_s$ and the absence of magnetic fields, the basic equations of diffusion are

$$\nabla p_s - \rho_s \mathbf{g} - \rho_{es} \mathbf{E} = \sum_{t \neq s} K_{st} (\mathbf{w}_t - \mathbf{w}_s) + \sum_{t \neq s} K_{st} z_{st} \frac{m_t \mathbf{r}_s - m_s \mathbf{r}_t}{m_s + m_t}, \tag{2.9}$$

$$
\begin{aligned}
\frac{5}{2} n_s k_\mathrm{B} \nabla T = & -\frac{2}{5} K_{ss} z''_{ss} \mathbf{r}_s - \frac{5}{2} \sum_{t \neq s} K_{st} z_{st} \frac{m_t}{m_s + m_t} (\mathbf{w}_t - \mathbf{w}_s) \\
& - \sum_{t \neq s} K_{st} \left[\frac{3m_s^2 + m_t^2 z'_{st}}{(m_s + m_t)^2} + \frac{4}{5} \frac{m_s m_t}{(m_s + m_t)^2} z''_{st} \right] \mathbf{r}_s \\
& + \sum_{t \neq s} K_{st} \frac{m_s m_t}{(m_s + m_t)^2} \left(3 + z'_{st} - \frac{4}{5} z''_{st} \right) \mathbf{r}_t,
\end{aligned}
\tag{2.10}
$$

where $\mathbf{E}$ is the quasi-static electric field and ρ_{es} is the average charge density of species s. These equations are still general, with the form of the resistance coefficients not yet fully specified. The physics of the particular types of interactions within ideal gases is fully contained in the coefficients K_{st}, z_{st}, z'_{st}, z''_{st}, and z'''_{st}.

For ionized gases, the resistance coefficients require evaluation of collision integrals that diverge for a pure Coulomb potential. However, since the two-particle interaction potential is only truly applicable on short length scales, an integration cutoff or screened potential is commonly adopted. Burgers chooses to calculate resistance coefficients using a pure Coulomb potential truncated at the Debye radius

$$
R_\mathrm{D} = \left(4\pi \sum_s \frac{n_s Z_s^2 e^2}{k_\mathrm{B} T} \right)^{-1/2}, \tag{2.11}
$$

which is assumed to be much larger than the inter-ion spacing. Indeed, for a plasma of one species, $R_\mathrm{D}/\lambda_\mathrm{ion} = (3\Gamma)^{-1/2}$. Applying this form of interaction to the collision integrals, the $l = 1$ integrals defined in Equation (2.4) can be evaluated (Baalrud &

Daligault, 2014)

$$S_{st}^{(1)} = \frac{2\pi R_{\rm D}^2 \alpha_{st}^4}{\Lambda_{st}^2 v^4} \ln \left[1 + \Lambda_{st}^2 \left(\frac{v}{\alpha_{st}} \right)^4 \right], \tag{2.12}$$

where $\Lambda_{st} = \mu_{st}\alpha_{st}^2 R_{\rm D}/(Z_s Z_t e^2)$. In order to perform the integral in Equation (2.5), Burgers notes that the dependence of $S_{st}^{(l)}$ on v inside the logarithmic term is weak, so that we can replace v^2 there with its average value $\langle v^2 \rangle = 3k_{\rm B}T/\mu_{st}$. Assuming a very dilute plasma, so that $\Lambda_{st}^2 \langle v^2 \rangle^2 / \alpha_{st}^4 \gg 1$, Burgers then writes

$$S_{st}^{(1)} \approx \frac{4\pi R_{\rm D}^2 \alpha_{st}^4}{\Lambda_{st}^2 v^4} \ln \left(\frac{3k_{\rm B} T R_{\rm D}}{Z_s Z_t e^2} \right), \tag{2.13}$$

and the final result for the resistance coefficients follows as

$$K_{st} \approx \frac{16\sqrt{\pi}}{3} \frac{n_s n_t Z_s^2 Z_t^2 e^4}{\mu_{st} \alpha_{st}^3} \ln \left(\frac{3k_{\rm B} T R_{\rm D}}{Z_s Z_t e^2} \right), \tag{2.14}$$

$$z_{st} = \frac{3}{5}, \qquad z'_{st} = \frac{13}{10}, \qquad z''_{st} = 2, \qquad z'''_{st} = 4. \tag{2.15}$$

With these coefficients now fully specified, Burgers diffusion equations along with constraints such as charge neutrality and current neutrality form a closed set of equations, which can be solved for $\mathbf{w}_s$, $\mathbf{r}_s$, $\mathbf{E}$, and $\mathbf{g}$ from the input of a stellar profile.

2.1.2 `MESA` Implementation

The diffusion routine originally implemented in `MESA` was based on the work of Thoul et al. (1994). They start with the Burgers equations, written in a compact notation following Noerdlinger (1977, 1978) that is equivalent to Equations (2.9) and (2.10) in one dimension. However, the approach of Thoul et al. (1994) differs from Burgers' original treatment in one important respect: the resistance coefficients are based on a modified result for the collision integrals. They follow Equation (2.15) for the various z_{st} coefficients, which uses a pure Coulomb potential with a cutoff at the Debye length, but the K_{st} coefficients were derived from an alternative fitting of the Coulomb logarithms introduced by Iben & MacDonald (1985). For these coefficients, they define $\lambda = \max(R_{\mathrm{D}}, \lambda_{\mathrm{ion}})$, and use

$$K_{st} = \frac{16\sqrt{\pi}}{3} \frac{n_s n_t Z_s^2 Z_t^2 e^4}{\mu_{st} \alpha_{st}^3} \frac{1.6249}{2} \ln \left[1 + 0.18769 \left(\frac{4 k_{\mathrm{B}} T \lambda}{Z_s Z_t e^2} \right)^{1.2} \right]. \tag{2.16}$$

This expression is a fit to the numerical results of Fontaine & Michaud (1979), motivated by white dwarf conditions where Burgers' approximations for dealing with Equation (2.12) are not valid ($\Gamma > 1$). Since this fit focuses on the strong coupling regime, and differs from Equation (2.14), these results can be incorrect in the limit of a dilute plasma as we discuss later. Nevertheless, Thoul et al. (1994) elected to use Equation (2.16) under all conditions, since it provides an approximately correct solution in a convenient closed form.

Using Equations (2.9) and (2.10) along with the constraints of current neutrality ($\sum_s \rho_{es} w_s = 0$) and local mass conservation ($\sum_s \rho_s w_s = 0$), Thoul et al. (1994) express an entire closed system of equations in a dimensionless matrix form suitable for numerical evaluation:

$$\frac{p}{K_0} \left(\alpha_i \frac{d \ln p}{dr} + \nu_i \frac{d \ln T}{dr} + \sum_{\substack{j=1 \\ j \neq \mathrm{e}}}^{S} \gamma_{ij} \frac{d \ln C_j}{dr} \right) = \sum_{j=1}^{2S+2} \Delta_{ij} W_j, \tag{2.17}$$

where S is the total number of species in the gas (including electrons) and $C_j = n_j/n_\mathrm{e}$ is the concentration of the jth species. Consult Thoul et al. (1994) for definitions of K_0, α_i, ν_i, γ_{ij}, and Δ_{ij}. The definition of W_j is

$$W_j = \begin{cases} w_j & \text{for } j = 1 \ldots S, \\ r_j & \text{for } j = S+1 \ldots 2S, \\ K_0^{-1} n_\mathrm{e} e E & \text{for } j = 2S+1, \\ K_0^{-1} n_\mathrm{e} m_\mathrm{p} g & \text{for } j = 2S+2. \end{cases} \tag{2.18}$$

This is the vector containing the unknown quantities solved for after specifying K_0, α_i, ν_i, γ_{ij}, and Δ_{ij}. The routine provided by Thoul et al. (1994) inverts Equation (2.17) for one term in the left hand side at a time so as to find the “generalized diffusion coefficients,” which can be used to construct diffusion velocities or contributions from pressure, temperature, or concentrations individually.

2.1.3 Modified Coefficients and Radiative Levitation

Hu et al. (2011) extend the methods of Thoul et al. (1994) by introducing some key modifications. First, they include an extra force term due to radiative levitation, so that Equation (2.9) becomes

$$\frac{dp_s}{dr} + \rho_s(g - g_{\mathrm{rad},s}) - n_s \bar{Z}_s e E = \sum_{t \neq s} K_{st}(w_t - w_s) + \sum_{t \neq s} K_{st} z_{st} \frac{m_t r_s - m_s r_t}{m_s + m_t} \ , \tag{2.19}$$

where $g_{\mathrm{rad},s}$ refers to the radiative acceleration on species s. $\bar{Z}_s$ is the average charge of species s, allowing an account of partial ionization so that $n_s \bar{Z}_s e = \rho_{es}$. They do not modify Equation (2.10).[1]

---

[1] As written in equation (3) of Hu et al. (2011), their expression has two errors in the first term on

In contrast to Thoul's original routine, Hu et al. (2011) use the resistance coefficients from Paquette et al. (1986a), which were generated based on substantial improvements to Fontaine & Michaud (1979). In evaluating the collision integrals, Paquette et al. (1986a) use a screened Coulomb potential of the form

$$V_{st}(r) = \bar{Z}_s \bar{Z}_t e^2 \frac{\exp(-r/\lambda)}{r}, \tag{2.20}$$

where, once again, $\lambda = \max(R_\mathrm{D}, \lambda_\mathrm{ion})$. As we note below, this choice of λ makes a substantial difference in strongly coupled plasmas, where the Debye radius no longer corresponds to a distance at which other nearby charged particles can significantly screen the Coulomb field. After setting up the algebra for a matrix solution very similar to that of Thoul et al. (1994), Hu et al. (2011) solve for the vector W_j (as defined in Equation 2.18) appearing in the equation

$$\frac{p}{K_0}\left(-\frac{\alpha_i m_i g_{\mathrm{rad},i}}{k_\mathrm{B} T} + \alpha_i \frac{d\ln p}{dr} + \nu_i \frac{d \ln T}{dr} + \sum_{\substack{j=1 \\ j\neq \mathrm{e}}}^{S} \gamma_{ij} \frac{d \ln C_j}{dr} \right) = \sum_{j=1}^{2S+2} \Delta_{ij} W_j. \tag{2.21}$$

Many of the quantities appearing in this equation are defined differently than in Thoul et al. (1994); see Hu et al. (2011) for details. We can also solve this equation directly for the vector W_j to obtain

$$\frac{W_{2S+1}}{W_{2S+2}} = \frac{K_0^{-1} n_\mathrm{e} e E}{K_0^{-1} n_\mathrm{e} m_\mathrm{p} g} = \frac{eE}{m_\mathrm{p} g}, \tag{2.22}$$

the strength of the electric field relative to gravity.

---

the right hand side of the first line: the sign is wrong, and it is missing resistance coefficients K_{ij}. Since neither of these errors propagates into later sections of the paper, it appears that both are simply typos, and otherwise their expression matches Equation (2.10) exactly.

2.2 Analytic Expression for the Electric Field

In some simple cases, Burgers equations can be solved to yield an analytic expression for the electric field, providing a useful test for `MESA`. Starting directly with his diffusion equations, Burgers (1969) arrives at the following expressions for a pure plasma of electrons along with one species of ions (charge Ze):

$$\frac{\nabla p_{\mathrm{e}} + n_{\mathrm{e}} e\mathbf{E}}{ZK_0} = \mathbf{w} + \frac{3}{5}\mathbf{r}_{\mathrm{e}}, \tag{2.23}$$

$$\frac{5}{2}\frac{n_{\mathrm{e}} k_{\mathrm{B}} \nabla T}{ZK_0} = -\frac{3}{2}\mathbf{w} - \left(\frac{2}{5}\frac{K_{\mathrm{ee}} z''_{\mathrm{ee}}}{K_{\mathrm{ie}}} + z'_{\mathrm{ie}}\right)\mathbf{r}_{\mathrm{e}}, \tag{2.24}$$

where $\mathbf{w} = \mathbf{w}_{\mathrm{i}} - \mathbf{w}_{\mathrm{e}}$. For a plasma with only one ion species in diffusion equilibrium, the constraints of current neutrality and local mass conservation give $\mathbf{w} = 0$. In the case of a pure hydrogen plasma, $p = 2p_{\mathrm{e}}$, and in hydrostatic equilibrium $\nabla p_{\mathrm{e}} = \nabla p/2 = \rho\mathbf{g}/2$. Hence, we can solve the above set of equations to find

$$e\mathbf{E} = -\frac{1}{2}m_{\mathrm{p}}\mathbf{g} - \frac{3}{2}\left(\frac{2}{5}\frac{K_{\mathrm{ee}} z''_{\mathrm{ee}}}{K_{\mathrm{ie}}} + z'_{\mathrm{ie}}\right)^{-1} k_{\mathrm{B}}\nabla T. \tag{2.25}$$

The coefficient for the temperature gradient term depends directly on the nature of the resistance coefficients in the Burgers formalism, so different models of Coulomb collisions in ionized plasma will lead to different results for the electric field.

As a slight generalization of Equation (2.25) in one dimension, we write

$$\frac{eE}{m_{\mathrm{p}} g} = \frac{1}{2} - \alpha_e \frac{k_{\mathrm{B}}}{m_{\mathrm{p}} g}\frac{dT}{dr}. \tag{2.26}$$

If we calculate the coefficient α_e using the Burgers' formalism with Equations (2.15) and

(2.16), we find

$$\alpha_e = \frac{3}{2}\left(\frac{2}{5}\frac{K_{\rm ee}z''_{\rm ee}}{K_{\rm ie}} + z'_{\rm ie}\right)^{-1} = 0.804 \tag{2.27}$$

A comparable analytic expression for the electric field is provided by Roussel-Dupré (1981), who applies a Boltzmann-Fokker-Planck approach to finding diffusion coefficients for trace elements in hydrogen plasma. His treatment of diffusion is more precise than the Burgers' formalism, but has the limitation of only being applicable in the case of nearly pure hydrogen with a diffusing trace element. His result for the electric field matches the form of Equation (2.26) with the coefficient $\alpha_e = 0.703$. This provides another useful point of comparison in the specific case of nearly pure hydrogen plasmas. Below we use this analytic expression as a test of the updated resistance coefficients employed by Hu et al. (2011).

2.3 Results and Comparisons

We have constructed several simple `MESA` test cases in order to illustrate the effects of radiative levitation and different resistance coefficients. Where possible, we compare `MESA` output to corresponding analytic expressions.

2.3.1 Electric Fields

By default, `MESA` uses the resistance coefficients provided by Paquette et al. (1986a), but it can also use the resistance coefficients defined by Iben & MacDonald (1985), given here in Equation (2.16). In the case of a pure hydrogen star, the coefficients given in Equation (2.16) lead directly to Equation (2.27), so these coefficients are especially useful in performing simple comparisons of `MESA` output to a corresponding analytic expression. Due to the complicated numerical methods used to obtain the resistance coefficients of Paquette et al. (1986a), it is not possible to write down a directly corresponding closed form analytic expression for the electric field, but results based on these more precise calculations compare favorably to those of Roussel-Dupré (1981) in the case of a pure hydrogen plasma. Starting with the `MESA` test suite, we constructed a solar mass pure hydrogen star, and we ran just long enough to turn on the diffusion routine and gather output for electric and gravitational fields. For such a star, we can compare `MESA` results for the electric field directly to the analytic expression given in Equation (2.26), with $\alpha_e = 0.804$ in the solution of Burgers (1969) and $\alpha_e = 0.703$ for Roussel-Dupré (1981).

Figure 2.1 plots the result of Equation (2.26) for both values of α_e, along with the results from the diffusion routine (Equation 2.22) for each type of resistance coefficients available in `MESA`. As expected, the curve calculated from the `MESA` diffusion routine output using the resistance coefficients of Iben & MacDonald (1985) closely matches the analytic expression with $\alpha_e = 0.804$ as calculated by Burgers (1969) using his similar coefficients. When using the more detailed numerical calculations for the resistance coefficients provided by Paquette et al. (1986a), the diffusion routine output closely resembles the more precise analytic calculation given by Roussel-Dupré (1981).

The Sun provides another interesting test case for comparing the effects of using

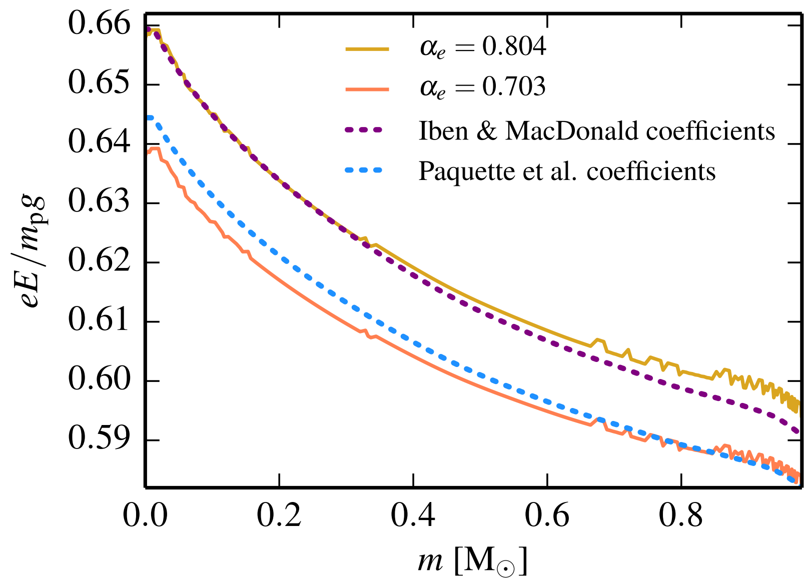

Figure 2.1: Comparison of electric field strengths relative to gravity in a pure hydrogen star ($M = 1.0\,\mathrm{M}_\odot$, $T_\mathrm{eff} = 5.74 \times 10^3\,\mathrm{K}$, $L = 0.576\,\mathrm{L}_\odot$) with nuclear burning artificially suppressed in the `MESA` routine to avoid any helium contamination. Solid lines represent the analytic expression given by Equation (2.26) for two different values of the coefficient α_e. Dashed lines represent output from the `MESA` diffusion routine as described in Equation (2.22), with the only difference being the resistance coefficients used to solve the Burgers equations.

different resistance coefficients. An example solar model from the `MESA` test suite was run with different choices of the resistance coefficients. Figure 2.2 shows a slight difference between the electric field strengths relative to gravity given by the Paquette et al. (1986a) coefficients and those by Iben & MacDonald (1985).

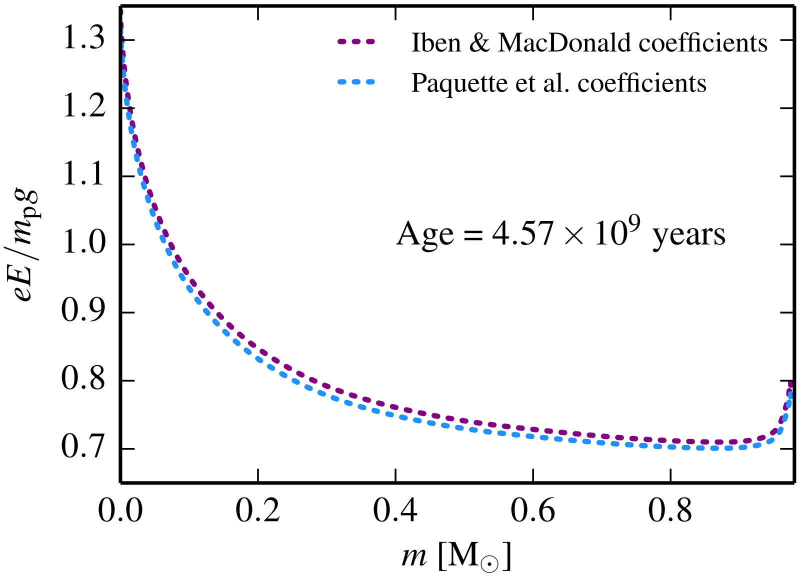

Figure 2.2: Comparison of electric field strengths relative to gravity using different resistance coefficients in a solar model.

2.3.2 Gravitational Fields

The `MESA` diffusion routine treats both the electric field and local gravitational acceleration as unknown quantities. `MESA` records the quantity W_{2S+2} (Equation 2.18), used to calculate the gravitational acceleration from the diffusion routine:

$$g_{\rm diff} = \frac{K_0 W_{2S+2}}{n_{\rm e} m_{\rm p}}. \tag{2.28}$$

This expression for $g_{\rm diff}$ is independent of the simpler expression for local gravitational acceleration $g_{\rm gauss} = Gm/r^2$. Figure 2.3 compares $g_{\rm gauss}$ and $g_{\rm diff}$ for a typical profile found using the example solar model from the `MESA` test suite. In Figure 2.3 a profile from a star of larger mass ($M = 1.5\,{\rm M}_\odot$) shows disagreement between the gravity outputs in the convective core because the diffusion solver is designed to ignore diffusion in convective regions. The diffusion output variables can therefore be wrong in such regions, but they have no impact on the stellar structure. The effects of diffusion in convective regions are completely overwhelmed by convective mixing and are therefore inconsequential.

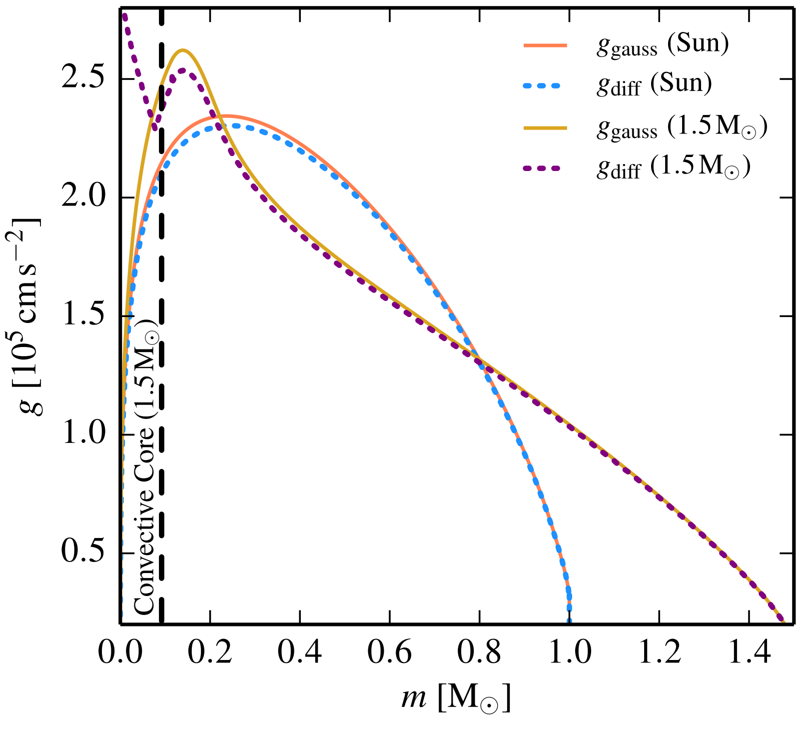

Figure 2.3: Comparison of gravitational fields obtained from $g_{\rm diff}$ and $g_{\rm gauss}$ in two `MESA` test suite cases. The two lines representing the Sun (age $= 4.57\,{\rm Gyr}$) show good agreement, while the two lines representing a $1.5\,{\rm M}_\odot$ star disagree in regions with large convective flux where diffusion is inconsequential.

2.3.3 Radiative Levitation

`MESA`'s implementation of radiative levitation is based on Hu et al. (2011). Figure 2.4 shows an abundance profile of a subdwarf B star model produced by `MESA`, where radiative levitation is responsible for the presence of ^{56}Fe, ^{58}Ni, and other metals near the surface (as also seen in figure 3 of Hu et al., 2011).

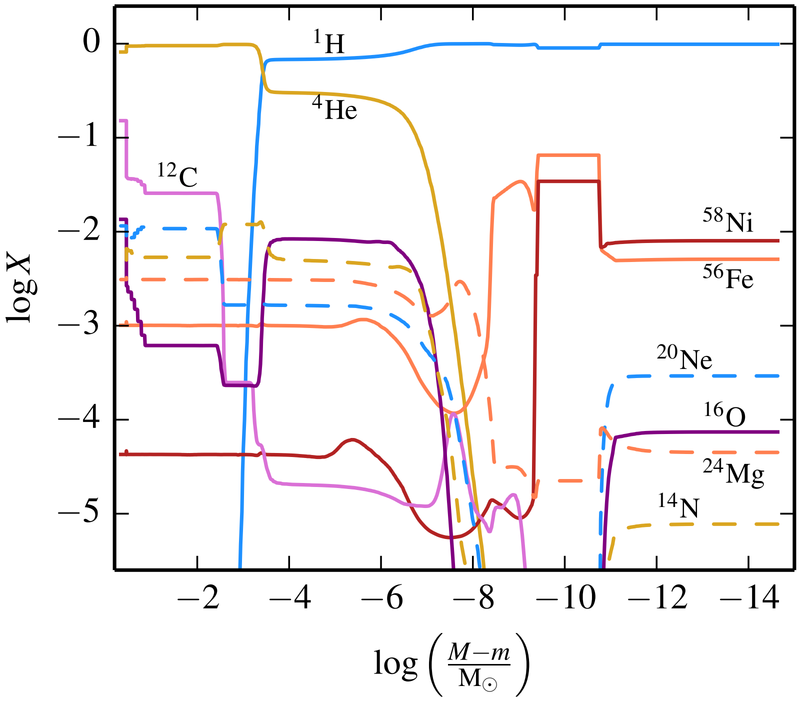

Figure 2.4: Abundance profile of a subdwarf B star model ($M = 0.462\,\mathrm{M}_\odot$, $T_{\mathrm{eff}} = 2.67 \times 10^4\,\mathrm{K}$, $L = 1.12\,\mathrm{L}_\odot$, age $= 5\,\mathrm{Myr}$) showing the effects of radiative levitation with a layer of ^{56}Fe/^{58}Ni at the surface.

2.3.4 White Dwarf Sedimentation

In a cooling WD, diffusion governs sedimentation over long timescales. The assumptions behind the formalism of the Burgers equations do not hold under white dwarf conditions:

- The Burgers equations assume all particle species satisfy an ideal gas equation of state. In the context of a degenerate WD both electrons and ions violate this assumption.
- The very dense, strongly coupled ($\Gamma > 1$) conditions of a WD call into question the validity of the two-particle scattering picture used to calculate the ion resistance coefficients.

Nevertheless, for lack of a better option, previous studies have relied on the Burgers equations with the coefficients of Paquette et al. (1986a). For example, see Córsico et al. (2002).

Figure 2.5 shows an abundance profile produced by `MESA` for a CO WD after 4 Gyr of evolution, where diffusion governs sedimentation in the outer layers. The vertical lines in Figure 2.5 mark the outer boundaries of regions where the two concerns listed above become significant. Nearly all of the WD resides inside at least one of these regimes, and much of the interesting diffusion sedimentation occurs inside regions that are both significantly coupled and highly degenerate. Thus, improvements to the treatment of diffusion are clearly necessary before we are able to describe diffusion in WDs adequately. This `MESA` run turns off diffusion for $\Gamma \geq 50$, where we expect strong coupling to substantially modify the underlying equations.

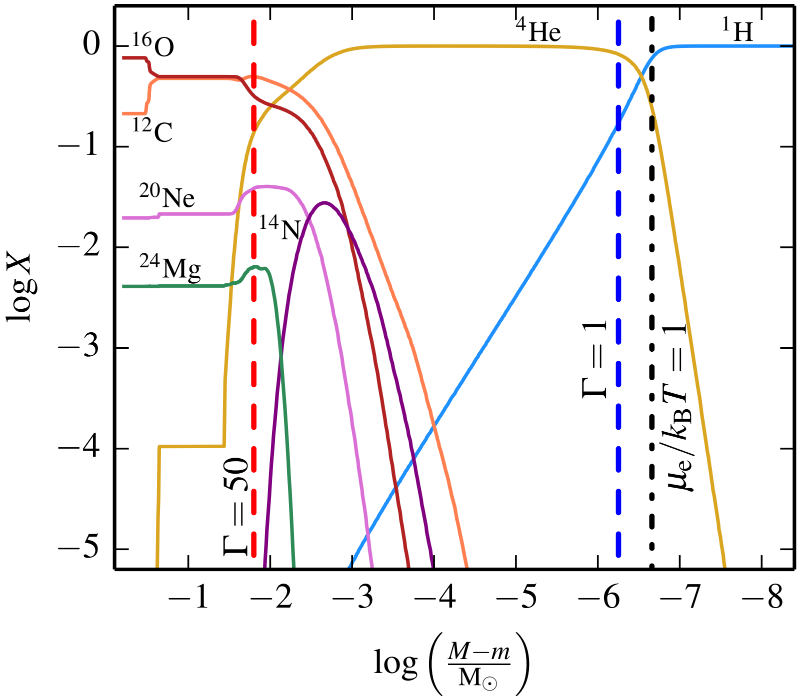

Figure 2.5: Abundance profile of a CO WD ($M = 0.611\ M_\odot$, $T_{\rm eff} = 5.16 \times 10^3\,$K, $L = 9.29 \times 10^{-5}\,L_\odot$) after 4 Gyr of WD evolution. The region left of the blue, dashed line is the interior of the WD, where $\Gamma \geq 1$. Left of the red, dashed line $\Gamma \geq 50$, and diffusion has been turned off for this region. The electrons are an ideal gas to the right of the black dot-dash line.

2.4 Expanding the Domain of Validity

The validity of the Boltzmann approach becomes questionable as $\Gamma > 1$ and the ions become a liquid. Bildsten & Hall (2001) estimated the diffusion coefficient in this liquid regime by using the Stokes-Einstein relation. However, for a broad-based code such as `MESA`, we need to implement diffusion into the $\Gamma > 1$ regime in a manner that allows for a smooth transition between coupling regimes.

Paquette et al. (1986a) successfully described diffusion in a regime of intermediate coupling through the use of screened potentials, which are a way to account for the collective nature of interactions in a dense plasma. Though there is no rigorous reason to expect that a formalism based on the two-particle scattering picture should work well as $\Gamma \to 1$, their comparison to simulations verified that this description of diffusion is very accurate for $\Gamma \lesssim 1$.

Can these approximations be extrapolated to the strongly coupled regime of $\Gamma > 1$? Baalrud & Daligault (2013) provide a method for numerically calculating resistance coefficients using a hypernetted chain (HNC) approximation from effective potentials. Figure 2.6 compares their HNC results (diamonds) to their Molecular Dynamics (MD) simulations of a one-component plasma (OCP, circles) for the self-diffusion coefficient D^*, defined by

$$D^* = \frac{D}{\lambda_{\text{ion}}^2 \omega_p}, \tag{2.29}$$

where ω_p is the plasma frequency and $D = 2D_{ss}^{(2)}$ (the factor of 2 in this definition ensures that if we redefine species s in terms of two subspecies s_1 and s_2, then $D = D_{s_1 s_2}^{(2)}$). The general expression for the interdiffusion coefficient is

$$D_{st}^{(2)} = \frac{n_s n_t}{n_s + n_t} \frac{k_{\text{B}} T}{K_{st}(1 - \Delta)}, \tag{2.30}$$

where the $1 - \Delta$ term in the denominator accounts for a second order correction that can be defined using

$$\Delta = \frac{(2\Sigma_{st}^{(12)} - 5\Sigma_{st}^{(11)})^2 / \Sigma_{st}^{(11)}}{55\Sigma_{st}^{(11)} - 20\Sigma_{st}^{(12)} + 4\Sigma_{st}^{(13)} + 8\Sigma_{st}^{(22)}}. \tag{2.31}$$

For reference, we also include a direct fit of Daligault & Murillo (2005) to the MD data of Ranganathan et al. (2003), given by

$$D^* = 0.0028 + 0.00525\left(\frac{173}{\Gamma} - 1\right)^{1.154}. \tag{2.32}$$

The agreement between the HNC and MD simulations shows that the HNC does a better job of accounting for correlation physics in strongly coupled plasmas than a simple screened Coulomb potential and allows for a surprising (and still physically unexplained) extension of the Burgers formalism into the strongly coupled regime. This recent work allows us to go into the large Γ limit with the Burgers formalism, but the question remains as to how we obtain diffusion coefficients in a reliable manner.

The self-diffusion coefficients from the two options in `MESA` are shown in Figure 2.6 and correlate with the MD data better than expected for the high Γ regime. In particular, the agreement is much better than that shown in figure 2 of Baalrud & Daligault (2013) for either "cutoff" or "screened" Coulomb methods. The reason for this agreement is that both `MESA` implementations use the inter-ion spacing rather than the Debye length once $\Gamma > 1/3$, which yields favorable scalings in the high Γ limit. Iben & MacDonald (1985) constructed their fitting formula based on a few numerical results for $\Gamma > 1$. Paquette et al. (1986a) also showed that their formalism can be extended to $\Gamma > 1$ as long as the inter-ion spacing is used rather than the Debye radius for the screening length.

Though `MESA` does not yet provide the capability of implementing resistance coefficients based on the HNC method, we may attempt this in the future by means of a table similar to that provided for the coefficients of Paquette et al. (1986a). For a more thor-

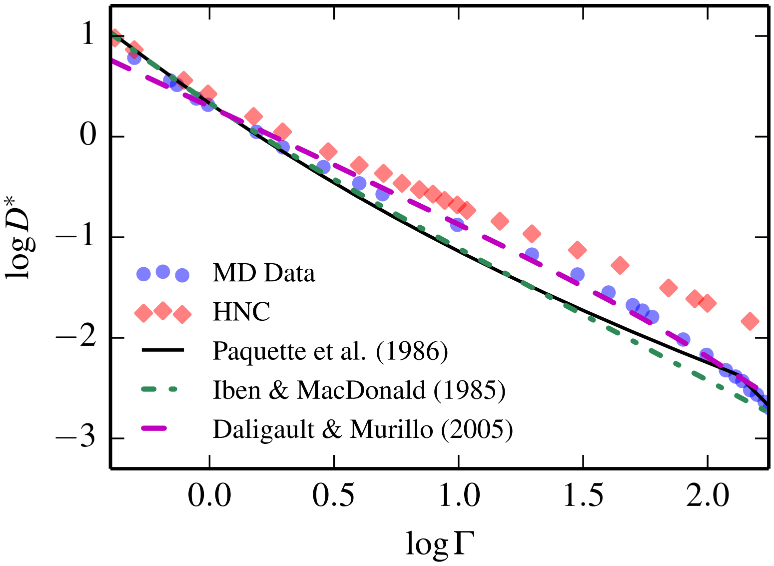

Figure 2.6: Compilation of the self-diffusion coefficients obtained from different methods. "MD Data" and "HNC" points are taken from Baalrud & Daligault (2013). The solid black line is the result of the `MESA` calculation using the coefficients of Paquette et al. (1986a). The dashed green line is the result of the calculation using the resistance coefficients from the original routine of Thoul et al. (1994) based on the fit to the Coulomb logarithm found in Iben & MacDonald (1985), given here in Equation (2.16). The dashed purple line represents the fit to MD data given here in Equation (2.32).

ough discussion of these methods and the likely path of application to mixtures, consult Beznogov & Yakovlev (2014). We will also need to correctly account for the electron degeneracy and the non-ideal equation of state for the ions, both of which modify the electrostatic field needed to correctly determine the forces that drive diffusion. This is the topic of the next chapter.

Chapter 3

Enhancing the Diffusion Framework for White Dwarfs

Chapter 2 describes in detail the original implementation of element diffusion in `MESA`. There are limitations to those methods, namely: (1) electron degeneracy was not properly accounted for in the diffusion equations, and (2) strong Coulomb interaction introduced theoretical uncertainties for the diffusion coefficients. These two issues are especially important when modeling diffusion in WDs. Here we describe the impact of degeneracy and present new methods to incorporate its effects. We also discuss recent updates to diffusion coefficients and potential approaches for further improvements.

3.1 Degeneracy

The approach to diffusion presented in Chapter 2 assumes all particles obey the ideal gas law. Electron degeneracy pressure can significantly modify the EOS and violate this assumption.

For a plasma species s (i.e., electrons and ions) with partial pressure P_s, mass density ρ_s, charge density ρ_{es}, number density n_s, and temperature T, the Burgers (1969) equations for diffusion are

$$\frac{\mathrm{d}P_s}{\mathrm{d}r} + \rho_s g - \rho_{es} E = \sum_{t \neq s} K_{st}(w_t - w_s) + \sum_{t \neq s} K_{st} z_{st} \frac{m_t r_s - m_s r_t}{m_s + m_t}, \tag{3.1}$$

$$\begin{aligned} \frac{5}{2} n_s k_\mathrm{B} \frac{\mathrm{d}T}{\mathrm{d}r} = &- \frac{2}{5} K_{ss} z''_{ss} r_s - \frac{5}{2} \sum_{t \neq s} K_{st} z_{st} \frac{m_t}{m_s + m_t}(w_t - w_s) \\ &- \sum_{t \neq s} K_{st} \left[\frac{3m_s^2 + m_t^2 z'_{st}}{(m_s + m_t)^2} + \frac{4}{5} \frac{m_s m_t}{(m_s + m_t)^2} z''_{st} \right] r_s \\ &+ \sum_{t \neq s} K_{st} \frac{m_s m_t}{(m_s + m_t)^2} \left(3 + z'_{st} - \frac{4}{5} z''_{st} \right) r_t. \end{aligned} \tag{3.2}$$

The resistance coefficients K_{st}, z_{st}, z'_{st}, and z''_{st} are defined in Equation (2.6). With S representing the total number of plasma species, we must solve for $2S + 2$ unknowns: S diffusion velocities (w_s), S heat flow vectors (r_s), the electric field (E), and the gravitational acceleration (g). The Burgers equations above for each species provide $2S$ equations, so we can close the system with two additional constraints, which are no net flow of mass or electric current due to diffusion,

$$\sum_s \rho_s w_s = 0 \ , \tag{3.3}$$

$$\sum_s \rho_{es} w_s = 0 \ . \tag{3.4}$$

This gives a total of $2S+2$ equations.

When electrons are degenerate, Equation (3.1) is difficult to apply since $\mathrm{d}P_\mathrm{e}/\mathrm{d}r$ no longer takes a simple analytic form. Moreover, the temperature term appearing on the left hand side of Equation (3.2) clandestinely assumes an ideal gas law. Burgers (1969) defines the temperature for each species as $T_s \equiv P_s/n_s k_\mathrm{B}$ and assumes thermal equilibrium between all species so that $T \equiv T_s$. The quantities P_s and n_s are defined in terms of moments of a Maxwellian distribution function, but the Fermi-Dirac distribution function for electrons no longer reduces to a Maxwellian form when they are degenerate, and hence $T_\mathrm{e} \neq P_\mathrm{e}/n_\mathrm{e} k_\mathrm{B}$. If the electrons remain in thermal equilibrium with their surroundings while failing to satisfy an ideal-gas relation for their temperature, the Burgers treatment assigns an incorrect temperature to degenerate electrons for the $\mathrm{d}T/\mathrm{d}r$ term in Equation (3.2).

Furthermore, the approach to diffusion described in Chapter 2 follows Thoul et al. (1994) in rearranging and rescaling all equations into one matrix system with units convenient for solving numerically,

$$\frac{P}{K_0}\left(\alpha_i \frac{\mathrm{d}\ln P}{\mathrm{d}r} + \nu_i \frac{\mathrm{d}\ln T}{\mathrm{d}r} + \sum_{\substack{j=1 \\ j\neq \mathrm{e}}}^{S} \gamma_{ij} \frac{\mathrm{d}\ln C_j}{\mathrm{d}r}\right) = \sum_{j=1}^{2S+2} \Delta_{ij} W_j \ . \tag{3.5}$$

The sum on the left hand side skips the electron index because $C_\mathrm{e} \equiv 1$ by construction, and so we save resources by not evaluating its gradient unnecessarily. Here, indices $i = 1, 2, \ldots S$ encode the S equations given by Equation (3.1), indices $i = S+1, S+2, \ldots, 2S$ encode the S equations given by Equation (3.2), and indices $i = 2S+1, 2S+2$ encode the 2 constraints of no current or mass flux. For definitions of the various coefficients and matrices in Equation (3.5), consult Chapter 2 and Thoul et al. (1994). We repeat a few particularly relevant definitions here. First, let $C_s = n_s/n_\mathrm{e}$ denote the species concentration, where n_e is the electron number density. Second, define the total concentration as $C = \sum_s C_s$. Then the quantity α_i appearing in Equation (3.5) above is defined as

$$\alpha_i = \begin{cases} C_i/C & i = 1, 2, \ldots S, \\ 0 & i = S+1, \ldots 2S+2. \end{cases} \tag{3.6}$$

The term $\alpha_i \,\mathrm{d}\ln P/\mathrm{d}r$ in Equation (3.5) is meant to capture contributions of the driving terms $\mathrm{d}P_s/\mathrm{d}r$ in Equation (3.1). But this correspondence only holds if the ratio of the partial pressure P_s for species s to the total pressure P is given by

$$\frac{P_s}{P} = \frac{C_s}{C} = \frac{n_s/n_\mathrm{e}}{\sum_t n_t/n_\mathrm{e}} = \frac{n_s}{n}, \tag{3.7}$$

where n is the total number density. This holds as long as all pressures are ideal-gas. However, once electron degeneracy modifies the equation of state, P does not scale linearly with n, and so Equation (3.7) fails for all species in the plasma. This means the α_i term no longer accurately represents the information in the Burgers equations for the diffusion velocity of any species.

Moreover, the prefactor P/K_0 in Equation (3.5) also assumes ideal gas for each species.

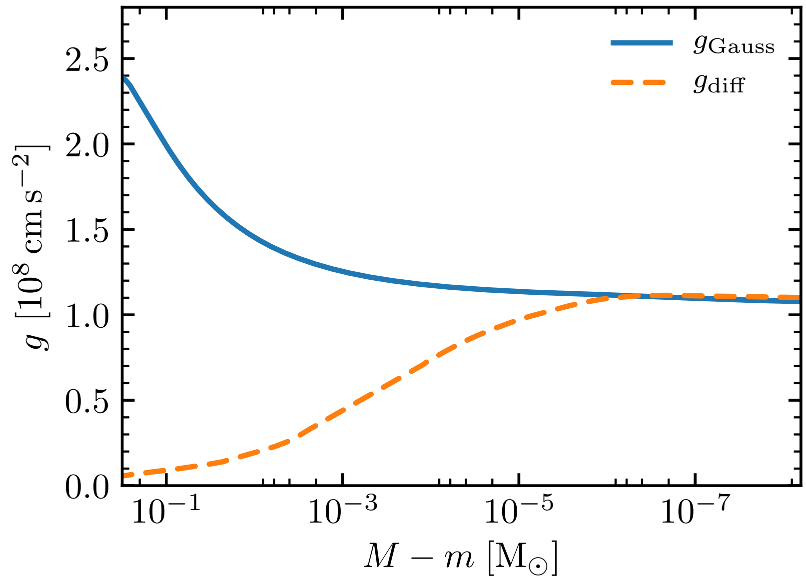

Figure 3.1: The gravitational acceleration reported by the diffusion routine described in Chapter 2 compared with $g_{\rm Gauss} = Gm/r^2$ for a $0.6\,{\rm M}_\odot$ `MESA` WD model.

The quantity $K_0 = 1.144 \times 10^{-40}(T/10^7\,{\rm K})^{-3/2}n_{\rm e}^2$ simply scales out some of the information common to all diffusion coefficients in the units used for Equation (3.5). Thoul et al. (1994) assume an ideal gas to simplify the prefactor in Equation (3.5) to

$$\frac{P}{K_0} = 2.00\frac{(T/10^7\,{\rm K})^{5/2}}{(\rho/100\,{\rm g\,cm^{-3}})}\left(\sum_s C_s\right)\left(\sum_s A_s C_s\right), \tag{3.8}$$

where A_s is the mass of species s in atomic mass units. This scaling was propagated into the `MESA` diffusion routine described in Chapter 2. Since ideal gas pressure can be significantly smaller than total pressure when electrons are degenerate, this prefactor for Equation (3.5) is systematically too small for degenerate plasmas. This can result in diffusion velocities that are many orders of magnitude smaller than obtained by a proper solution.

We can verify that there are problems in the degenerate regime by looking at the local gravitational acceleration $g_{\rm diff}$, which is solved for simultaneously with the diffusion velocities in the diffusion routine described by Chapter 2. `MESA` also reports the gravitational acceleration independent of the diffusion routine, $g_{\rm Gauss} = Gm/r^2$. For a `MESA` WD model, layers below the surface quickly become degenerate, and the difference between $g_{\rm diff}$ and $g_{\rm Gauss}$ is significant (Figure 3.1). This reflects the fact that the solutions given by the diffusion routine scale with a pressure that is far too small in the interior.

3.2 New Methods

We now describe new methods that have been introduced to avoid the limitations discussed in Section 3.1.

3.2.1 Recasting the Burgers Equations

The problems with Equation (3.5) demonstrated in Figure 3.1 can be circumvented by solving the Burgers equations directly as presented in Equations (3.1) and (3.2). When avoiding the rescaling of the Burgers equations that was originally adopted from Thoul et al. (1994), no limitations on the form of total pressure are present.

To that end, we recast the diffusion solver into the form given in Appendix A. This form closely follows the general approach presented by Thoul et al. (1994) for arranging the full set of equations into a single matrix equation, but enters the Burgers equations into that matrix structure without rescaling any quantities. We therefore avoid making any additional ideal-gas assumptions beyond those already present in the Burgers equations.

3.2.2 Resolving the Degeneracy Problem

Electron degeneracy makes it difficult to evaluate the term $\mathrm{d}P_s/\mathrm{d}r$ in Equation (3.1) in the case of electrons, but it is possible to form a closed set of diffusion equations that makes no explicit reference to this equation for the electrons. Even in many applications involving WDs, each ion species can be treated as approximately ideal, and hence Equation (3.1) remains useful for ions. We are then left with just two problematic equations out of the system of $2S+2$ equations: Equations (3.1) and (3.2) for the electrons.

For the $S-1$ species of ions in the system, we can write $S-1$ Equations (3.1) in the form

$$\begin{aligned} n_s k_\mathrm{B} T \frac{\mathrm{d}\ln T}{\mathrm{d}r} + n_s k_\mathrm{B} T \frac{\mathrm{d}\ln n_s}{\mathrm{d}r} + n_s A_s m_\mathrm{p} g - n_s \bar{Z}_s e E \\ = \sum_{t\neq s} K_{st}(w_t - w_s) + \sum_{t\neq s} K_{st} z_{st} \frac{A_t r_s - A_s r_t}{A_s + A_t}, \end{aligned} \tag{3.9}$$

where $\bar{Z}_s$ is the average charge of species s obtained using Paquette et al. (1986b). Taking this together with S Equations (3.2) and the two constraints on current and mass flux, we have a total of $2S+1$ equations. If we drop g as an unknown and treat it as a fixed input to the diffusion routine in `MESA` using $g = Gm/r^2$, we are left with $2S+1$ unknowns. This gives a closed system of diffusion equations with no explicit reference to the problematic Equation (3.1) for electrons. This is the form of diffusion equations described in Appendix A.

The thermal diffusion terms (those including $\mathrm{d}T/\mathrm{d}r$ in Equation 3.2) still contain ideal-gas assumptions as described in Section 3.1. Fortunately, in WD cores where strong electron degeneracy occurs, electron conduction leads to efficient thermal transport, resulting in small temperature gradients. With $\mathrm{d}T/\mathrm{d}r \ll T/H$, where $H = P/\rho g$ is the local scale height, the heat flow vectors (representing kinetic energy carried along a temperature gradient by diffusing particles) become negligible: $r_s \ll w_t$ for all w_t. Thus for WD interiors the system of diffusion equations can be simplified by dropping the S heat flow terms, removing the need for the S Equations (3.2). Indeed, according to Iben & MacDonald (1985) and Paquette et al. (1986b), thermal diffusion leads only to small corrections to the diffusion velocities for degenerate WD interiors.

Therefore, following Iben & MacDonald (1985), we provide options for neglecting thermal diffusion in electron degenerate regions, setting $r_s = 0$ and dropping Equation (3.2) for each species. Equation (3.9) then simplifies to the following $S - 1$ equations that no longer depend on r_s for the ions:

$$\frac{1}{n_s}\sum_t K_{st}(w_t - w_s) + \bar{Z}_s eE = A_s m_{\mathrm{p}} g + k_{\mathrm{B}} T \frac{\mathrm{d}\ln T}{\mathrm{d}r} + k_{\mathrm{B}} T \frac{\mathrm{d}\ln n_s}{\mathrm{d}r}, \tag{3.10}$$

which matches Equation (10) from Iben & MacDonald (1985). Together with the 2 constraints, this leaves a simplified set of $S+1$ equations for $S+1$ unknowns: S diffusion velocities w_s and the electric field E.

Thermal diffusion terms tend to enhance gravitational settling velocities (Iben et al., 1992). This can be seen in Figure 3.2 for a $1.25\,\mathrm{M}_{\odot}$ star on the MS, where the solvers that include thermal diffusion speed the sedimentation of ^{16}O away from the surface relative to the solver that neglects thermal diffusion. `MESA` also provides options for smoothly transitioning between diffusion velocities obtained with and without thermal diffusion (averaging between the two solutions in a blending region as a function of electron degeneracy parameter). By default, this transition region occurs when the electron chemical potential is near $\mu_{\mathrm{e}} \sim k_{\mathrm{B}}T$, but it is left to the user to decide on an appropriate range of electron degeneracy over which thermal diffusion should be shut off, if at all. The effect of blending between solvers with and without thermal diffusion is to suppress the thermal enhancements to diffusion velocities, smoothly pushing the enhancements to zero as electrons reach a degeneracy threshold. The implementation for the simplified set of diffusion Equations (3.10) and the smooth turn-off of thermal diffusion terms as a function of degeneracy are described in Appendix A.

In order to confirm that we recover the correct behavior on the MS, we compare results obtained with different diffusion routines for a $1.25\,\mathrm{M}_{\odot}$ star in Figure 3.2. Here the results based on Thoul et al. (1994) are valid, since no significant departures from ideal-gas behavior are present near the surface. The results obtained with the new scheme are in agreement.

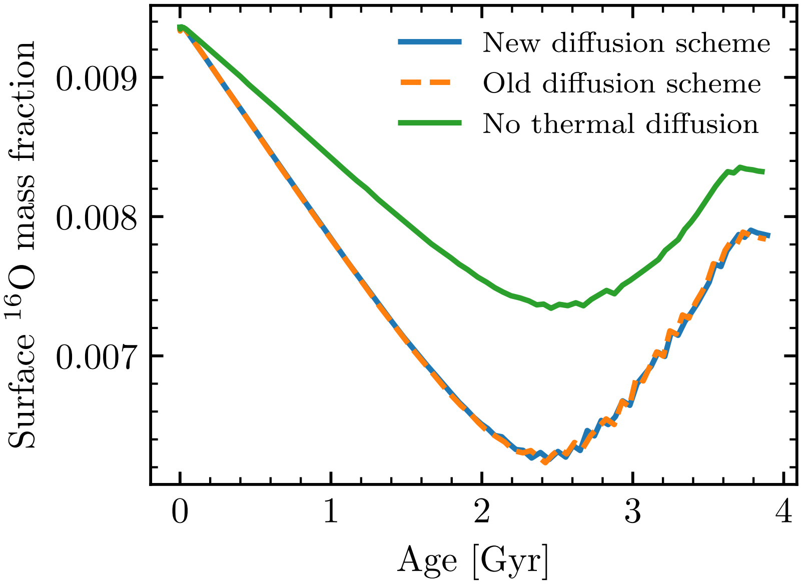

Figure 3.2: Surface ^{16}O mass fraction of a $1.25\,\mathrm{M}_{\odot}$ star over its MS lifetime. It first decreases as diffusion causes sedimentation. Then it increases after the small surface convection zone begins to grow, catching the receding ^{16}O and mixing it back toward the surface.

3.2.3 Diffusive Equilibrium

MESA II and Chapter 2 show abundance profiles for WDs that have reached diffusive equilibrium in their outer layers. Figure 23 of MESA II compares the diffusive tails of H and He to an analytic expression from Althaus et al. (2003) and finds good agreement. However, Althaus et al. (2003) note that their analytic expression for diffusive equilibrium follows Arcoragi & Fontaine (1980) in assuming an ideal gas, and the equilibrium abundance profiles from their evolutionary models deviate from the analytic expression due to the inclusion of electron degeneracy. Similarly, the He layer of the WD model shown in Figure 2.5 is partially degenerate, and hence the driving forces for diffusion should be modified in this region.

For a fully-ionized isothermal ideal gas the electric field that serves as one of the driving forces for diffusion in Equation (3.9) takes the form $eE = [A/(Z+1)]m_{\rm p}g$. In contrast, in the limit of strong electron degeneracy, the electric field approaches $eE = (A/Z)m_{\rm p}g$. When He is the background material, the electric-to-gravitational force ratio $eE/m_{\rm p}g$ increases from 4/3 to 2. In this limit, any trace isotopes with $A/Z = 2$ see no net sedimentation force ($ZeE - Am_{\rm p}g = 0$), while H with $A/Z = 1$ sees a significant upward sedimentation force ($ZeE - Am_{\rm p}g > 0$). This extra buoyant force on H in a degenerate He background pushes the diffusive tail further toward the surface relative to the ideal-gas case, as shown in Figure 3.3. With the proper handling of electron degeneracy described in Section 3.2, our `MESA` models now agree with the time-dependent diffusion models shown in Figure 18 of Althaus et al. (2003).

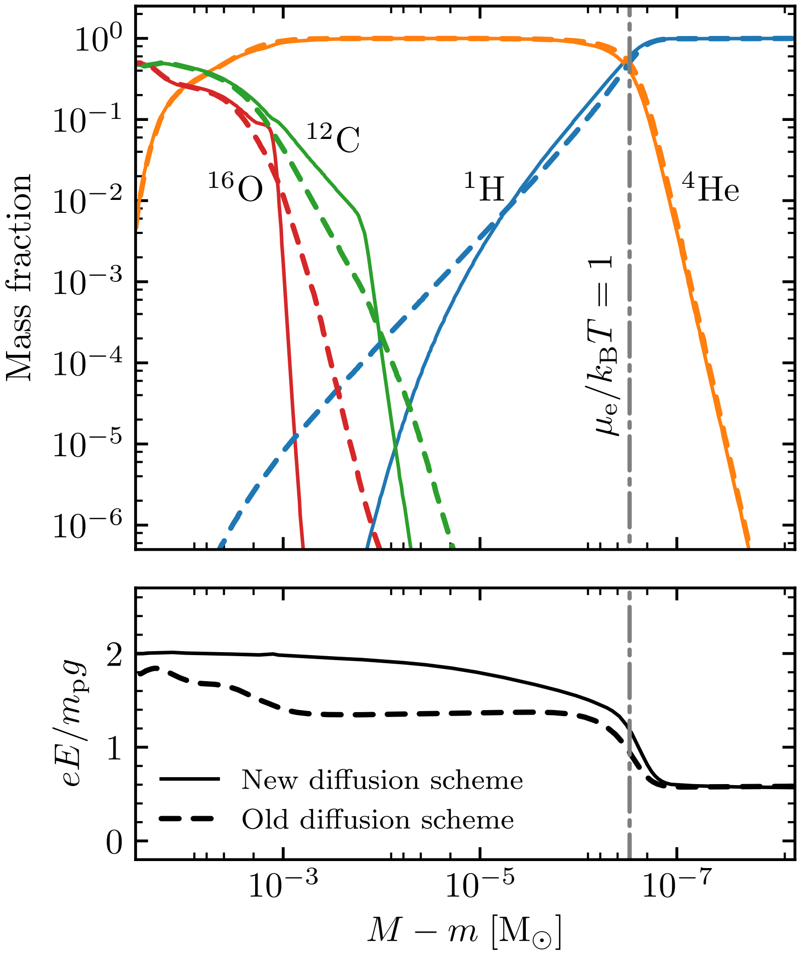

Figure 3.3: Abundance profiles in $0.6\,\mathrm{M}_\odot$ `MESA` WD models at $T_{\rm eff} = 5,000\,\mathrm{K}$ after evolving for 4 Gyr to approach diffusive equilibrium in the outer layers. The old equations assume an ideal gas; the new equations include the effects of electron degeneracy.

3.2.4 Radiative Levitation

Radiative levitation is included as an optional extra term. The Burgers equations are modified with a extra forcing term by taking $\rho_s g \rightarrow \rho_s(g - g_{\mathrm{rad},s})$, as shown in Equation (2.19). Our implementation continues to follow Hu et al. (2011) but no longer employs their matrix structure for the Burgers equations; details of how the $g_{\mathrm{rad},s}$ terms are handled with the updated diffusion schemes can be found in Appendix A.

3.3 Updated Diffusion Coefficients

The Paquette et al. (1986a) diffusion coefficients have served as the standard for stellar diffusion problems. The scattering cross-sections for these coefficients are calculated using a screened Coulomb potential

$$V_{12}(r) = \frac{\bar{Z}_1 \bar{Z}_2 e^2}{r} \exp(-\lambda/r) \ , \tag{3.11}$$

with the screening length chosen as $\lambda = \max(\lambda_{\mathrm{D}}, \bar{a}_{\mathrm{i}})$, where λ_{D} is the Debye length, $\bar{a}_{\mathrm{i}} = (3/4\pi n_{\mathrm{i}})^{1/3}$ is the average interionic distance, and n_{i} is the ion density. This choice is a crude but effective way to handle the strongly coupled regime; as shown in Chapter 2, this yields reasonable agreement with diffusion coefficients calculated from molecular dynamics.

Stanton & Murillo (2016) provide updated collision integrals for screened Coulomb interactions and suggest improvements to the treatment of screening length. They provide fitting functions and tables that can be used with any choice of screening length. In `MESA` we follow their suggested screening prescription. The electron screening length is given by a Thomas-Fermi approximation that accounts for non-relativistic degeneracy:

$$\lambda_{\mathrm{e}} = \left(\frac{4\pi e^2 n_{\mathrm{e}}}{\sqrt{(k_{\mathrm{B}}T)^2 + \left(\frac{2}{3}E_{\mathrm{F}}\right)^2}} \right)^{-1/2} , \tag{3.12}$$

where $E_{\mathrm{F}} = \hbar^2(3\pi^2 n_{\mathrm{e}})^{2/3}/2m_{\mathrm{e}}$ is the electron Fermi energy. The direct inclusion of degeneracy increases λ_{e}. The ion screening lengths are the Debye lengths for each species,

$$\lambda_i = \left(\frac{4\pi \bar{Z}_i^2 e^2 n_i}{k_{\mathrm{B}}T} \right)^{-1/2} . \tag{3.13}$$

To prevent ions from screening below the inter-ionic spacing, Stanton & Murillo (2016) introduce an approximate ion-sphere for each species $a_i \equiv (3\bar{Z}_i/4\pi n_{\mathrm{e}})^{1/3}$, and define an ion-sphere coupling parameter

$$\Gamma_i \equiv \frac{(\bar{Z}_i e)^2}{a_i k_{\mathrm{B}}T}. \tag{3.14}$$

Their net effective screening length is then

$$\lambda_{\mathrm{eff}} \equiv \left[\frac{1}{\lambda_{\mathrm{e}}^2} + \sum_i \frac{1}{\lambda_i^2} \left(\frac{1}{1+3\Gamma_i} \right) \right]^{-1/2} . \tag{3.15}$$

This construction enforces a minimum on the screening length at approximately the ion-sphere radius a_i for each species, similar to the strict minimum at $\bar{a}_{\mathrm{i}}$ set by Paquette et al. (1986a). Stanton & Murillo (2016) point out that this adjustment to the ion screening length is physically motivated by the ion pair distribution functions in a strongly coupled plasma, where the occupation probability within the ion-sphere radius is negligible, and hence no ions are present to provide screening beneath that cutoff.

The proper handling of degeneracy in the electron screening length makes it unnecessary to impose any particular minimum there, so there is no longer any ad hoc appeal to a universal minimum screening length.

For repulsive Coulomb potentials of the form in Equation (3.11), Stanton & Murillo (2016) provide fits and tables of collision integrals and coefficients that we now use to calculate the resistance coefficients K_{st} for inclusion in the Burgers equations in `MESA`. They do not provide fits for attractive potentials, and Paquette et al. (1986a) note that interactions with these potentials behave significantly differently from those with repulsive potentials when screened. Hence, `MESA` continues to use the Paquette et al. (1986a) coefficients for electron-ion terms, and adopts Stanton & Murillo (2016) for all ion-ion coefficients. In any case, it is evident from Equation (2.14) that the resistance coefficients approximately follow $K_{st} \propto \mu_{st}^{1/2}$, where μ_{st} is the reduced mass of particles s and t; so, electron-ion resistance coefficients are generally negligible compared to the ion-ion terms.

The calculations of Paquette et al. (1986a) overestimate the electron-ion resistance coefficients in the case where electrons are degenerate. This is because diffusion and resistance coefficients are generally calculated assuming that the velocity distributions of all particles are Maxwellian, and the coefficients roughly scale as $K_{st} \propto v_s^{-2} v_t^{-2}$. When the electrons become degenerate, their characteristic kinetic energies are of order $E_{\rm F} \gg k_{\rm B}T$, and so their velocity distribution skews toward larger velocities. This results in smaller resistance coefficients K_{st}, overestimating the impact of electron-ion drag. However, the overestimate results in coefficients that remain negligible compared to ion-ion terms, and no attempt is made to correct it in `MESA`.

For repulsive potentials, the coefficients from Stanton & Murillo (2016) generally agree with those of Paquette et al. (1986a) to within a few percent. In strongly coupled WD interiors the Stanton & Murillo (2016) coefficients lead to $\sim 10\%$ shorter diffusion timescales due to a screening length that is allowed to be somewhat smaller than the minimum value imposed by Paquette et al. (1986a): $\lambda_{\rm eff} < \bar{a}_{\rm i}$. Future prospects for further improvements to diffusion coefficients include the recent progress on effective potential methods from Daligault et al. (2016) and Shaffer et al. (2017).

3.4 Diffusion-Induced Flashes on He WDs

Diffusion-induced H shell flashes on low-mass ($M \lesssim 0.4\,{\rm M}_\odot$) He WDs are known to alter their cooling times (Althaus & Benvenuto, 2000; Althaus et al., 2001) and seismic properties (Althaus et al., 2013). Istrate et al. (2016a,b) use `MESA` to model this process, generating tables of cooling timescales and comparing `MESA` models with those of Althaus et al. (2013).

Figure 3.4 shows an exploration of the H shell flash domain for a large grid of $Z = 0.02$ `MESA` models over a range of He-core and H-envelope masses. Here the envelope mass is defined as the total mass of H-rich material ($X > 0.01$) at the surface at the beginning of the WD cooling track. Lines show the minimum envelope masses for which H shell flashes occur given various diffusion prescriptions.

For a given core mass, there is a range of envelope masses that exhibit shell flashes only

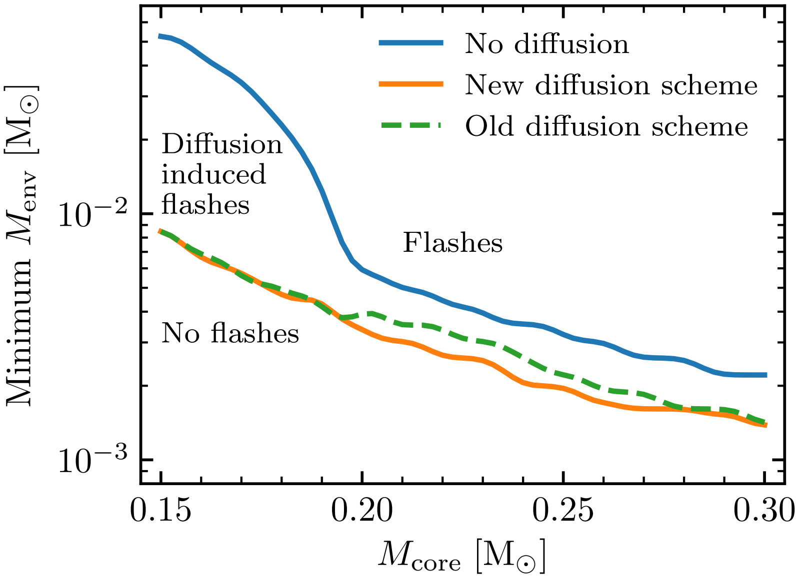

Figure 3.4: Minimum envelope mass M_{env} for which a H shell flash occurs on a He WD core mass M_{core} for $Z = 0.02$ `MESA` models with and without diffusion. The regime for the phenomenon of diffusion-induced flashes lies between the boundaries for models with and without diffusion.

if diffusion is included, but this range depends on the diffusion prescription. The two lower lines for models including diffusion in Figure 3.4 differ only in the handling of electron degeneracy in the diffusion scheme. This illustrates the importance of properly handling degeneracy as described in Section 3.2, since the diffusion-induced flashes are typically ignited by CNO burning in the diffusive tail of H that reaches into the partially degenerate He layers. WDs in this mass range often experience cycles of many H flashes, depleting H incrementally until insufficient H remains to ignite another flash. The disagreement between diffusion prescriptions on the minimum envelope mass for flashes is therefore significant, as this will determine the total number of flashes and final H mass that sets the ultimate cooling timescale for an object.

To explore the full range of parameters presented in Figure 3.4, our WD models were built by artificially stripping the H envelope down to a specific mass coordinate above the He core of a $1.0\,\mathrm{M}_\odot$ model ascending the RGB. For a discussion of `MESA` models including proto-WD formation and the resulting H envelope masses, see Istrate et al. (2016b).

3.5 Heating from ^{22}Ne Settling

In the strongly degenerate limit, $eE/m_\mathrm{p}g \approx 2$ for C/O WD cores. For an isotope where $A/Z \neq 2$, the electric and gravitational fields result in a net force that drives diffusion. For ^{22}Ne in cooling WD interiors, this force is $F = ZeE - Am_\mathrm{p}g \approx -2m_\mathrm{p}g$, causing ^{22}Ne to sediment toward the center and deposit energy as it moves deeper into the gravitational potential (Bildsten & Hall, 2001; Deloye & Bildsten, 2002; García-Berro et al., 2008, 2010). This heating can prolong the WD cooling timescale, especially at late times when the WD is very dim and radiates away the energy slowly. This effect may be especially important for explaining WD luminosity functions in old and metal-rich open clusters such as NGC 6791, where abundant ^{22}Ne is available in WD interiors to provide heating.

`MESA` now offers an option to include this heating term in the energy equation (see Appendix B.6) when diffusion is enabled. The specific rate at which energy is deposited is

$$\epsilon_{22} = \frac{|F|v_{22}}{(Am_\mathrm{p})/X_{22}} = (22m_\mathrm{p}g - 10eE)\,\frac{X_{22}v_{22}}{22m_\mathrm{p}}. \tag{3.16}$$

The ^{22}Ne diffusion velocity (v_{22}) and electric field are calculated in the diffusion routine and then used to evaluate the above heating term. Note that the updates to diffusion

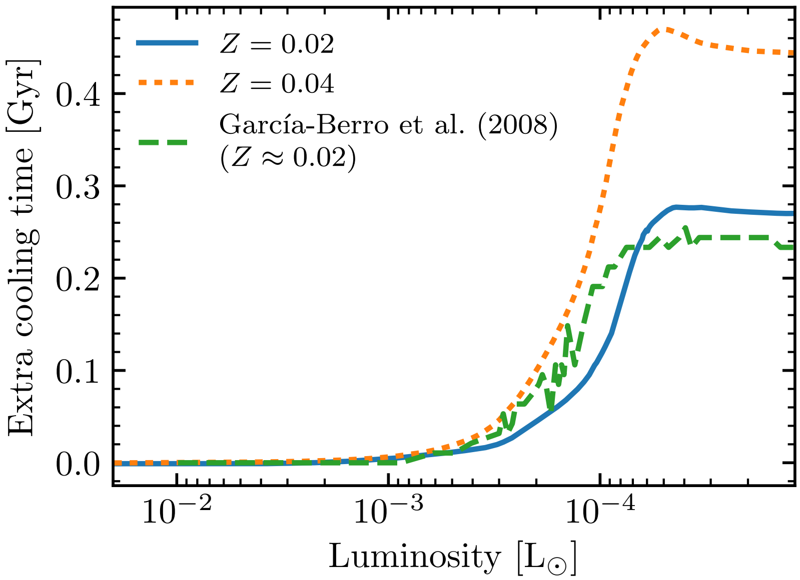

Figure 3.5: Extra cooling time required to reach a given luminosity for $0.6\,M_\odot$ WD models including heating from ^{22}Ne settling, relative to models neglecting this heating. For comparison, we also show a result from García-Berro et al. (2008) for a $0.6\,M_\odot$ WD with an Oxygen-dominated core composition. Figure B.6 shows the same quantity including other physical processes such as crystallization for the same $Z = 0.02$ WD model shown here.

described in Section 3.2 are essential for correctly calculating both the diffusion velocity and magnitude of the driving force in the degenerate interior of the WD.

Figure 3.5 shows the delay in WD cooling from introducing ϵ_{22} into $0.6\,M_\odot$ models. These models turn off diffusion for $\Gamma > 175$, so ϵ_{22} is only active in material for which crystallization has not yet occurred. The time-delays shown in Figure 3.5 are in good agreement with those shown by Deloye & Bildsten (2002) and García-Berro et al. (2008) for comparable cases.

Chapter 4

Increases to Inferred Rates of Planetesimal Accretion due to Thermohaline Mixing in Metal-accreting White Dwarfs

Despite the short sedimentation timescales for metals that should lead to pure hydrogen atmospheres, a large fraction ($25 - 50\%$) of DA white dwarfs (WDs) show signatures of atmospheric metal pollution (Zuckerman et al., 2003). Though radiative levitation can prevent some element settling in WDs with $T_{\rm eff} \gtrsim 20,000\,{\rm K}$ (Chayer et al., 1995a,b; Chayer, 2014), more than 25% of WDs can only be explained with ongoing accretion providing a continued supply of metals to the surface (Koester et al., 2014). Many of these WDs are thought to be actively accreting debris from disrupted planetesimals that are perturbed within the WD tidal radius, and some show anomalous infrared emission indicative of an accreting disk (Jura, 2003; Farihi et al., 2009; Girven et al., 2012; Vanderburg et al., 2015; Farihi, 2016). Detailed atmosphere models for mixing and metal sedimentation allow for inferences of accretion rates and compositions (Vauclair et al., 1979; Dupuis et al., 1992, 1993; Koester & Wilken, 2006; Koester, 2009), and thus these objects serve as unique laboratories for observing the interior bulk composition of planetesimals around WDs (Zuckerman et al., 2007; Gänsicke et al., 2012; Dufour et al., 2012; Koester et al., 2014; Jura & Young, 2014).

Much recent work in this field has relied on the assumption of equilibrium between accretion and diffusive sedimentation. The large mean molecular weight of accreted material compared to the hydrogen atmosphere can lead to additional mixing due to the thermohaline instability (Deal et al., 2013; Wachlin et al., 2017), though see Koester (2015) for a critique of its efficacy. In this chapter, we perform time-dependent stellar evolution calculations using `MESA`. Our models that account for diffusion and thermohaline mixing indicate that both mechanisms are essential for understanding the range of observed parameters for polluted WDs. Our work spans a large range of effective temperatures and accretion rates, allowing new accretion inferences for hydrogen atmosphere WDs with $T_{\rm eff} \lesssim 20,000\,{\rm K}$.

In Section 4.1, we discuss standard diffusion calculations and their relation to sedimentation in `MESA` models. In Section 4.2, we examine conditions for thermohaline instability in layers containing accreted metals and explore the impact of thermohaline mixing in our `MESA` models. In Section 4.3, we present the resulting implications for observed polluted WDs with hydrogen atmospheres. We find that WDs with $T_{\rm eff} \gtrsim 10,000\,{\rm K}$ require accretion rates several orders of magnitude larger than previously inferred, with the largest as high as $\dot{M}_{\rm acc} \approx 10^{13}\,{\rm g\,s^{-1}}$ when accounting for thermohaline mixing. In Section 4.4, we discuss avenues for extending and refining the grid of models.

4.1 Gravitational Sedimentation

In accretion-diffusion equilibrium, the observed metal abundances in the outer convective zone of a polluted WD are simply related to those in the accreted material. The timescale for convective mixing is rapid, so accreted material is quickly distributed throughout the convection zone. The observable mass fraction of an accreted pollutant $X_{{\rm cvz},i}$ is then related to the accretion rate $\dot{M}_i$ for that pollutant by (cf. Vauclair et al. 1979; Dupuis et al. 1993; Koester 2009)

$$M_{\rm cvz}\frac{dX_{{\rm cvz},i}}{dt} = \dot{M}_i - \frac{X_{{\rm cvz},i}M_{\rm cvz}}{\tau_{{\rm diff},i}} \ , \tag{4.1}$$

where the sedimentation time for element i is

$$\tau_{{\rm diff},i} \equiv \frac{M_{\rm cvz}}{4\pi r^2 \rho v_{{\rm diff},i}} \ , \tag{4.2}$$

and $v_{{\rm diff},i}$ is the downward sedimentation velocity of the accreted pollutant at the base of the surface convection zone, at density ρ and radius r, where it sinks away from the fully mixed surface region.

Assuming $\tau_{\text{diff},i}$, $\dot{M}_i$, and M_{cvz} are time independent, Equation (4.1) gives

$$X_{\text{cvz},i}(t) = X_{\text{cvz},i}(0)\, e^{-t/\tau_{\text{diff},i}} + \frac{\dot{M}_i}{M_{\text{cvz}}} \tau_{\text{diff},i} \left(1 - e^{-t/\tau_{\text{diff},i}}\right) \ , \tag{4.3}$$

and for $t \gg \tau_{\text{diff},i}$ the mass fraction approaches the equilibrium value

$$X_{\text{eq},i} = \frac{\dot{M}_i}{M_{\text{cvz}}} \tau_{\text{diff},i} \ . \tag{4.4}$$

Since sedimentation timescales in hydrogen WD atmospheres are short ($\tau_{\text{diff}} \sim$ days – 10^4 years, Koester 2009), Equation (4.4) is typically used to infer elemental accretion rates from observed abundances assuming $X_{\text{obs},i} = X_{\text{eq},i}$. A total accretion rate can be found simply by adding the individual contributions of each observed pollutant ($\dot{M}_{\text{acc}} \equiv \sum_i \dot{M}_i$), or by scaling to a fiducial composition when other elements are not directly observed but are expected to be present (e.g. $\dot{M}_{\text{acc}} = \dot{M}_{\text{Ca}}/X_{\text{acc,Ca}}$).

The theoretical ingredients for the preceding calculation are diffusion timescales and surface convection zone masses (Koester & Wilken, 2006; Koester, 2009). We calculate these as part of time-dependent WD evolutionary models with hydrogen atmospheres using `MESA` version 10398. In particular, our treatment of diffusion is based on a complete time-dependent solution of the Burgers equations for diffusion (Burgers, 1969), adapted to be appropriate for any degree of electron degeneracy in WDs as described in detail in Chapter 3. This treatment yields diffusion velocities for each species in the plasma everywhere in the stellar model. Our results for diffusion timescales and convection zone masses in WDs with hydrogen atmospheres are comparable to those of Koester (2009).[1]

---

[1] Most recent tables found at http://www1.astrophysik.uni-kiel.de/~koester/astrophysics/astrophysics.html.

The convection prescription for our models is ML2 (Bohm & Cassinelli, 1971) with $\alpha_{\rm MLT} = 0.8$. Our settings for surface boundary conditions rely on either a grey iterative procedure ($T_{\rm eff} > 9,000\,{\rm K}$) described in MESA II, or the WD atmosphere tables in `MESA` ($T_{\rm eff} < 9,000\,{\rm K}$), which are adapted from Rohrmann et al. (2012). Diffusion coefficients are those of Stanton & Murillo (2016) as implemented in Chapter 3, which produce comparable results to those of Paquette et al. (1986a). More details are presented in the next chapter. For WDs with no surface convection zone ($T_{\rm eff} \gtrsim 15,000\,{\rm K}$), we take the surface region in which to evaluate $X_{\rm cvz}$ and $M_{\rm cvz}$ to be everywhere above the photosphere in the model (optical depth $\tau_{\rm Ross} = 2/3$), with $\tau_{\rm diff}$ evaluated at the photosphere. See Gänsicke et al. (2012) for a thorough discussion justifying this choice.

The upper panel of Figure 4.1 shows that a `MESA` model of an accretion episode with constant $\dot{M}_{\rm acc} = 9.2 \times 10^8\,{\rm g\,s^{-1}}$ (accreted mass fractions $X_{\rm Fe} = 0.307$, $X_{\rm O} = 0.295$, $X_{\rm Mg} = 0.199$, $X_{\rm Si} = 0.153$, $X_{\rm Ca} = 0.046$) agrees with the prediction of Equation (4.3) when thermohaline mixing is not considered. This model is tuned to match the observed properties of G29-38 presented by Xu et al. (2014), including $T_{\rm eff} = 11,820\,{\rm K}$, $\log g = 8.4$, and the abundances presented in their Table 3. Our `MESA` model has diffusion timescales on the order of 1-2 years, roughly a factor of 5 longer than those reported by Xu et al. (2014) due to a larger surface convection zone in the `MESA` model ($M_{\rm cvz} = 6 \times 10^{-14}\,M_\odot$). This difference arises because convection zone depths are very sensitive to $T_{\rm eff}$ around the temperature for G29-38, and our models show growth of the surface convection zone slightly sooner as the WD cools compared to those of Koester (2009) in this regime.

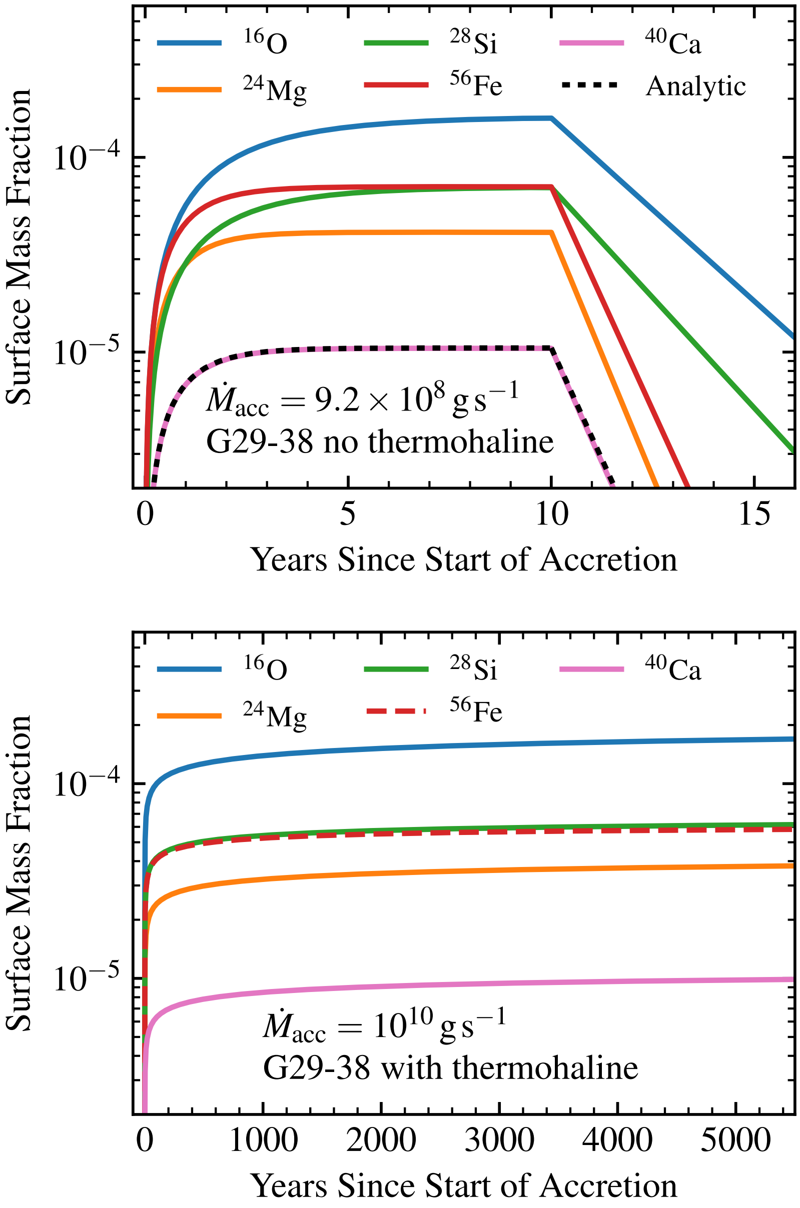

Figure 4.1: *Upper Panel:* `MESA` model of G29-38 matching observed abundances (Xu et al., 2014) after accreting earth-like composition at a total rate of $\dot{M}_{\rm acc} = 9.2 \times 10^8\,{\rm g\,s^{-1}}$ for 10 years to approach equilibrium surface abundances. Accretion ceases after 10 years to illustrate the exponential decay of observable pollution governed by diffusion in the absence of accretion. No thermohaline mixing is included in this model. *Lower Panel:* `MESA` model of G29-38 including thermohaline mixing accreting metals in the ratios observed at the WD surface at $\dot{M}_{\rm acc} = 10^{10}\,{\rm g\,s^{-1}}$ for 5,000 years to approach observed surface abundances.

Hence, we infer an accretion rate that is 40% larger than the value Xu et al. (2014) report, but we find excellent agreement with their relative diffusion timescales and composition of the accreted material.

4.2 Thermohaline Instability

Deal et al. (2013) and Wachlin et al. (2017) have noted that thermohaline mixing may significantly alter the accretion rates inferred from observed abundances in polluted WDs. Koester (2015) argued against the efficacy of this instability for a few cases. Here we show the regime in which it operates and its overall impact, which can be large.

4.2.1 Onset of the Instability Beneath the Convection Zone

Thermohaline instability can occur when fluid is stable to convection according to the Ledoux criterion, but has an inverted mean molecular weight gradient:

$$\nabla_T - \nabla_{\rm ad} < \frac{\varphi}{\delta}\nabla_\mu < 0 \ , \tag{4.5}$$

where $\nabla_T = (\partial \ln T/\partial \ln P)$ is the temperature gradient, $\nabla_{\rm ad} = (\partial \ln T/\partial \ln P)_s$ is the adiabatic temperature gradient, $\nabla_\mu = (\partial \ln \mu/\partial \ln P)$ is the mean molecular weight gradient, $\varphi = (\partial \ln \rho/\partial \ln \mu)_{P,T}$, and $\delta = -(\partial \ln \rho/\partial \ln T)_{P,\mu}$. A fluid satisfying Equation (4.5) alone is not guaranteed to experience thermohaline instability; the double-diffusive nature of the instability requires that microscopic particle transport between fluid elements be slow compared to thermal transport so that perturbed elements maintain their composition long enough for the instability to grow. This extra condition is (Baines & Gill, 1969; Brown et al., 2013; Garaud, 2018):

$$\frac{(\varphi/\delta)\nabla_\mu}{\nabla_T - \nabla_{\rm ad}} > \frac{\kappa_\mu}{\kappa_T} \ , \tag{4.6}$$

where κ_μ and κ_T are the particle and thermal diffusivities.

The mean molecular weight gradient is inverted in the radiative zone beneath the outer convective layer of these polluted WDs. Heat is carried there via radiative diffusion, so

$$\kappa_T = \frac{4acT^3}{3\kappa\rho^2 C_P} \ . \tag{4.7}$$

We use the diffusion coefficients of oxygen or iron in hydrogen as representative of the particle diffusivity relevant for the mean molecular weight of a fluid element:

$$\kappa_\mu \approx D_{\rm H,O} \text{ or } D_{\rm H,Fe} \ . \tag{4.8}$$

We obtain these coefficients from the same routines based on Stanton & Murillo (2016) that we use to calculate coefficients for element diffusion (see Chapter 3).

Figure 4.2 shows the quantities relevant for evaluating the criterion for thermohaline instability given in Equation (4.6) for the G29-38 `MESA` model. The metallicity (Z) profile for the model is unstable according to Equation (4.6), and the result of enabling thermohaline mixing will be to mix a significant amount of the metals deeper into the star. A significantly larger accretion rate is then required to match the observed surface pollution in G29-38, similar to the results of Wachlin et al. (2017).

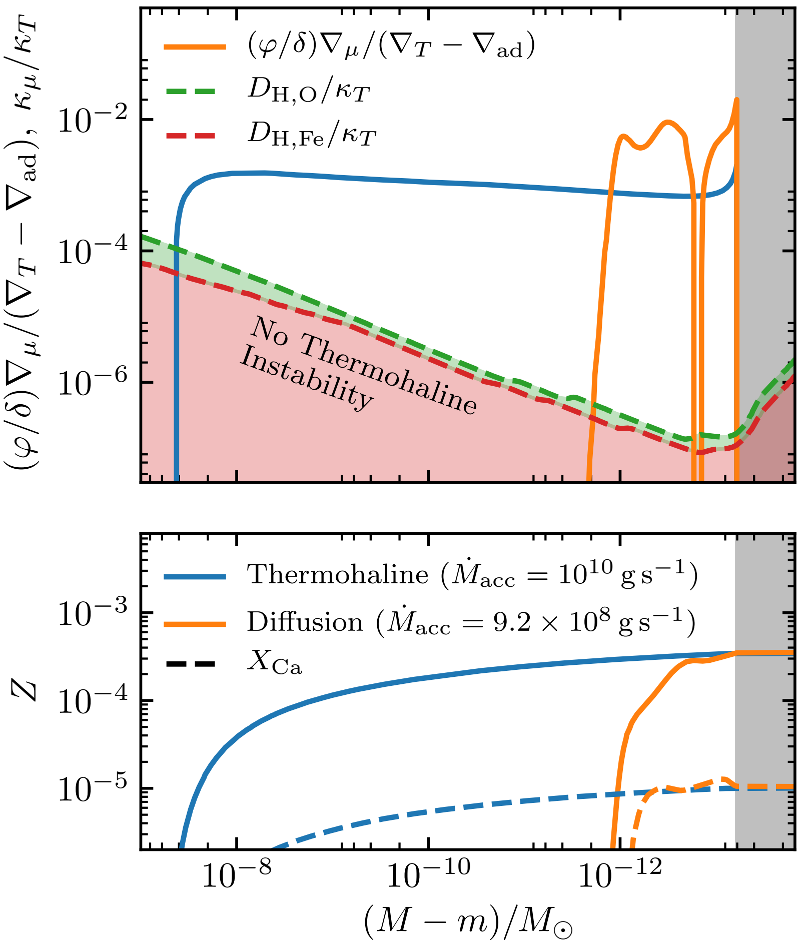

Figure 4.2: Profiles of quantities relevant to the onset of thermohaline instability in G29-38 models. The lower panel shows the metallicity profile with (blue) and without (orange) thermohaline mixing enabled according to Equation (4.9) with $\alpha_{\rm th} = 1$, for the same models as shown in Figure 4.1. The upper panel shows the quantities necessary for evaluating the inequality given by Equation (4.6) in both cases, confirming that these profiles are thermohaline unstable. The gray shaded region represents the convective envelope.

4.2.2 Outcomes when Thermohaline Mixing is Included

The default thermohaline mixing treatment in `MESA` (see MESA II) follows Kippenhahn et al. (1980) in defining the mixing coefficient:

$$D_{\rm th} = \alpha_{\rm th} \kappa_T \frac{3}{2} \frac{(\varphi/\delta)\nabla_\mu}{\nabla_T - \nabla_{\rm ad}} \ , \tag{4.9}$$

where $\alpha_{\rm th}$ is a dimensionless efficiency parameter that should be near unity. `MESA` also offers options for using more recent treatments of thermohaline mixing due to Traxler et al. (2011) and Brown et al. (2013), which attempt to constrain free parameters by calibrating effective 1D prescriptions to 3D simulations.

Figure 4.3 shows the surface Ca mass fraction in polluted $0.6\,M_\odot$ ($\log g = 8.0$) WD models after accreting bulk earth material (McDonough, 2001) at $\dot{M}_{\rm acc} \in (10^4, 10^{12})\,{\rm g\,s^{-1}}$ for many diffusion timescales. These `MESA` models include element diffusion at all times. The upper panel includes models with thermohaline mixing according to Equation (4.9) (several values of $\alpha_{\rm th}$) and also according to Brown et al. (2013). These results suggest that Equation (4.9) reasonably captures the net effects of thermohaline mixing on pollution for efficiencies in the range $1 < \alpha_{\rm th} < 10$, though note that Vauclair & Théado (2012) have argued that more mixing should occur near the limit of instability to convection ($\nabla_\mu \sim \nabla_T - \nabla_{\rm ad}$). We elect to employ the treatment of Equation (4.9) with $\alpha_{\rm th} = 1$ for the models presented in the remainder of this work. Our choice of mixing prescription thus represents a reasonable but conservative estimate of the magnitude and total impact of thermohaline mixing for pollution.

The lower panel of Figure 4.3 shows the Ca pollution for models at several differ-

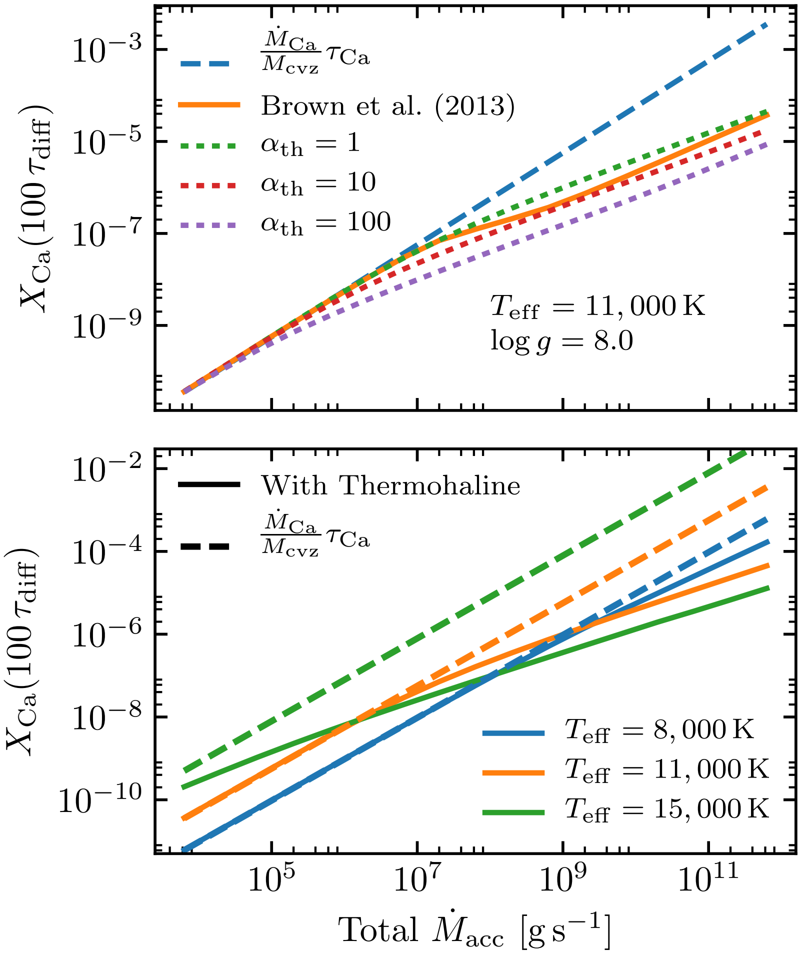

Figure 4.3: Surface Ca mass fraction after 100 diffusion timescales as a function of total metal accretion rate for a $0.6\,M_\odot$ ($\log g = 8.0$) WD models accreting metals in bulk earth ratios. The upper panel shows several thermohaline prescriptions for a $T_{\rm eff} = 11,000\,{\rm K}$ WD. The lower panel shows the WD at several temperatures for the thermohaline prescription of Equation (4.9) with $\alpha_{\rm th} = 1$.

ent values of $T_{\rm eff}$ using the thermohaline prescription of Equation (4.9) with $\alpha_{\rm th} = 1$. Models with thin surface convection zones ($T_{\rm eff} = 11,000\,{\rm K}; 15,000\,{\rm K}$) experience significant dilution of surface metals due to thermohaline mixing, while models with larger surface convection zones ($T_{\rm eff} = 8,000\,{\rm K}$) distribute accreted metals to an extent that ∇_μ is rarely large enough to drive significant thermohaline mixing beneath the convection zone. In this case, diffusive sedimentation governs the timescale for settling and observed equilibrium abundances.

Unlike models with only element diffusion, those with thermohaline mixing do not approach a true equilibrium composition on a short timescale. Instead, they approach a quasi-steady state composition near the surface for timescales represented in Figure 4.3 ($\sim 100\,\tau_{\rm diff}$), but these quasi-steady abundances may vary by factors of a few if accretion continues over very long timescales ($\sim$Myr) as the thermohaline mixing region continues to extend deeper into the hydrogen envelope. Thermohaline mixing ceases to extend inward only when it encounters the diffusive tail of helium near the base of the hydrogen envelope. The ∇_μ from this helium tail counteracts that from metals mixing inward, preventing any further thermohaline instability. For the hydrogen envelopes in our $M = 0.6\,M_\odot$ WD models ($M_{\rm H} \approx 10^{-6}\,M_\odot$), the thermohaline mixing encounters the helium layer only after long periods ($\sim$Myr) of sustained high accretion rates ($\dot{M}_{\rm acc} \gtrsim 10^{10}\,{\rm g\,s^{-1}}$). Hence, this effect is not significant for the models we present in this work, but it may be important for WDs with much thinner hydrogen envelopes ($M_{\rm H} \lesssim 10^{-8}\,M_\odot$), where it could lead to higher observed surface pollution by preventing thermohaline mixing that would otherwise occur.

4.3 Accretion Rates and Compositions

In order to show the impact of our work on inferring accretion rates, we built an interpolating tool to map observed Ca abundances to total metal accretion rates for `MESA` runs that include thermohaline mixing and diffusion. The `MESA` runs used for this interpolation consist of 12 different WD models ($M = 0.6\,M_\odot$, $\log g = 8.0$) in the temperature range $T_{\rm eff} \in (6000, 20500)\,{\rm K}$, each accreting bulk earth composition (McDonough, 2001) for 100 diffusion timescales at 17 rates in the range $\dot{M}_{\rm acc} \in (10^4, 10^{12})\,{\rm g\,s^{-1}}$, with diffusion enabled along with thermohaline mixing according to Equation (4.9) with $\alpha_{\rm th} = 1$. At fixed $T_{\rm eff}$, a given observed Ca abundance corresponds to a unique value of total $\dot{M}_{\rm acc}$ (as seen in the lines in the lower panel of Figure 4.3), and we interpolate between results from `MESA` runs at different $T_{\rm eff}$ to yield a result for $\dot{M}_{\rm acc}$ as a function of $T_{\rm eff}$ and observed Ca abundance. Figure 4.4 shows the results of this procedure for inferring total $\dot{M}_{\rm acc}$ for the 38 polluted hydrogen atmosphere WDs given in Table 1 of Koester & Wilken (2006).

Figure 4.4 also compares against `MESA` calculations assuming only diffusion governs the equilibrium state, where we use Equation (4.4) to infer $\dot{M}_{\rm acc}$, and assume bulk earth abundances for the accreted material. For objects with $T_{\rm eff} > 10,000\,{\rm K}$, the inferred accretion rate can increase by several orders of magnitude when accounting for thermohaline mixing, confirming the earlier work of Deal et al. (2013) and Wachlin et al. (2017).

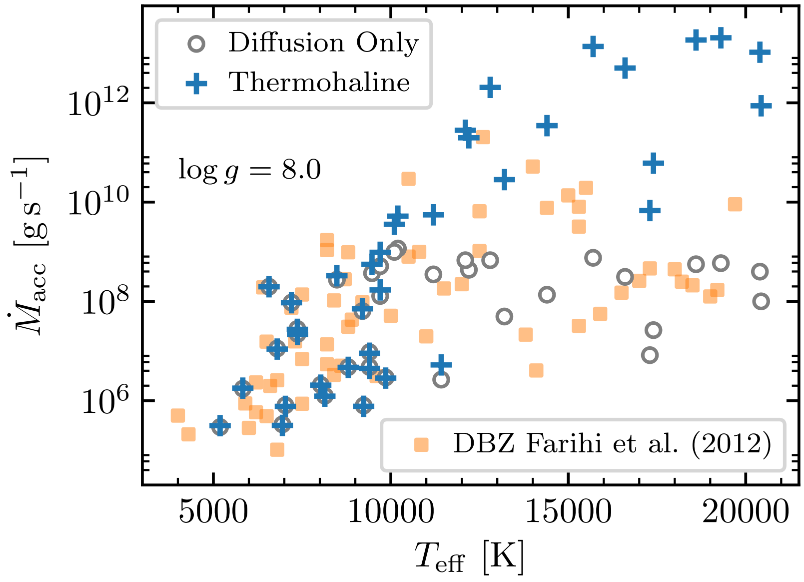

Figure 4.4: Accretion rates inferred with (blue crosses) and without (open circles) thermohaline mixing from the observed Ca abundances for the 38 WDs given in Table 1 of Koester & Wilken (2006), assuming $\log g = 8.0$ and bulk earth composition in the accreting material. The orange points show the rates inferred for He atmosphere WDs by Farihi et al. (2012) for comparison.

Our models assume that the observed Ca is only a fraction of the total metals being accreted. This is important because all accreted metals participate in determining the ∇_μ that drives thermohaline mixing. This should be justified, since Ca is often the most easily identifiable element in spectra even when other metals are present, and for the objects in which many metals are identified, compositions appear roughly consistent with bulk earth (Gänsicke et al., 2012; Jura & Young, 2014; Xu et al., 2014). In this chapter, our inferences are limited by the fact that all input models have a mass of $0.6\,M_\odot$ ($\log g = 8.0$), which is not always consistent with the observed WDs. More `MESA` runs are necessary to build a tool that can interpolate over $\log g$ as well as $T_{\rm eff}$. However, we do not expect the small corrections due to different $\log g$'s to lead to qualitative changes in the several orders of magnitude effect seen in Figure 4.4.

For objects where multiple pollutants are observed, it should be possible to estimate relative accreted abundances, but there are two distinct regimes. For low accretion rates or thick convective envelopes where the thermohaline instability is not excited, the equilibrium state of each element is separately governed by Equation (4.4), so that the inferred relative abundance is related to observations by

$$\frac{X_{\rm obs,1}}{X_{\rm obs,2}} = \frac{\tau_{\rm diff,1} X_{\rm acc,1}}{\tau_{\rm diff,2} X_{\rm acc,2}}\ . \tag{4.10}$$

However, when thermohaline mixing dominates over diffusion, the diffusion timescales play no role. Instead the mixing coefficient $D_{\rm th}$ applies equally to all elements, resulting in the observed relative abundances of metals matching the ratios in the accreted material.

Returning to `MESA` models of G29-38, when thermohaline mixing is included, we achieve a good match to observed pollution with an accretion rate of $\dot{M}_{\rm acc} \gtrsim 10^{10}\,{\rm g\,s^{-1}}$ (depending on thermohaline efficiency), higher than the value $\dot{M}_{\rm acc} \approx 3 \times 10^{9}\,{\rm g\,s^{-1}}$ suggested by Wachlin et al. (2017). The significant thermohaline mixing also means that the best match to observed composition is achieved with a model that accretes metals in the same ratios as those observed at the photosphere, with no correction for relative diffusion timescales. Whereas the model without thermohaline mixing matches bulk earth composition remarkably well, models of G29-38 with thermohaline mixing imply a significantly more oxygen rich composition of the accreted material.

4.4 Conclusions and Next Steps

Our `MESA` models indicate that inferred accretion rates in polluted WDs with hydrogen dominated atmospheres of $T_{\rm eff} \gtrsim 10,000\,{\rm K}$ require systematic increases due to thermohaline mixing, often by several orders of magnitude. These higher rates can be tested, especially via X-ray observations (Farihi et al., 2018). Very thin hydrogen envelopes ($M_{\rm H} \lesssim 10^{-8}\,M_\odot$) are not considered in the models presented here, but are often poorly constrained. Such thin envelopes could impose a systematic effect on inferences by lessening the impact of thermohaline mixing, with smaller inferred accretion rates as the result. We have also assumed bulk earth composition, so objects that are very rich in Ca relative to other metals could also be revised downward.

Models that include significant corrections due to thermohaline mixing also show very different surface abundance ratios than those that only include diffusive sedimentation.

Diffusion leads to a correction to observed compositions due to different sedimentation timescales for each element, while models where thermohaline mixing dominates over diffusion show metal ratios that match the accreted material.

We do not expect the thermohaline instability to play as large of a role on WDs with helium atmospheres due to their much thicker convective envelopes that distribute accreted metals much deeper into the star. Preliminary `MESA` runs with helium atmosphere WD models indicate that thermohaline mixing is unimportant for those with $T_{\rm eff} \lesssim 15,000\,{\rm K}$ due to their thick ($M_{\rm cvz} \gtrsim 10^{-6}\,M_{\odot}$) convective envelopes. Hotter He atmosphere WDs may require some accretion rate corrections due to thermohaline mixing, but we expect the effect to remain modest. As predicted by Deal et al. (2013), our results in Figure 4.4 appear to resolve the discrepancy between inferred accretion rates in helium and hydrogen atmospheres that is seen in the work of Farihi et al. (2012).

The high accretion rates implied by our calculations here may pose problems for models that deliver accreted metals to the WD surface via Poynting-Robertson drag (Rafikov, 2011a). Models of runaway accretion events due to other disk processes have been proposed to account for high inferred accretion rates in helium atmosphere WDs (Rafikov, 2011b; Metzger et al., 2012), but it is unclear if these can account for the highest rates suggested in Figure 4.4.

Further work is necessary to extend our `MESA` models to cover the entire range of $\log g$ relevant to all observed polluted WDs. The next chapter will present this along with more details from `MESA` models for surface convection zone masses and individual diffusion timescales for many elements, as well as models for WDs with helium atmospheres. Surface mixing regions in polluted WDs may also be modified by convective overshoot (Tremblay et al., 2015; Kupka et al., 2018), and `MESA` models have the potential for including this effect as well.

Chapter 5

Polluted White Dwarfs: Mixing Regions and Diffusion Timescales

A large fraction (25%–50%) of isolated white dwarf (WD) atmospheres show signatures of polluting metals (Zuckerman et al., 2003; Koester et al., 2014). Heavy element sedimentation timescales are short (Schatzman, 1945, 1948), and this implies recent or ongoing accretion of observed heavy elements (Vauclair et al., 1979; Koester et al., 2014). Polluted WD spectra are often accompanied by infrared emission from a dust disk (Koester et al., 1997; Farihi et al., 2009; Girven et al., 2012; Farihi, 2016), and the predominant model for the origin of this dust is debris from disrupted planetesimals (Jura, 2003; Jura & Young, 2014; Vanderburg et al., 2015). Models for WD surface mixing allow inferences of the composition of these planetesimals and the rates at which WDs accrete this material (Koester & Wilken, 2006; Koester, 2009; Dufour et al., 2010, 2012; Koester et al., 2011; Farihi et al., 2013; Raddi et al., 2015).

While many have relied on elemental sedimentation timescales to make inferences about polluted WD accretion, recent work has revealed that thermohaline instability is active and substantially modifies the inferred accretion rate $\dot{M}_{\rm acc}$ (Deal et al., 2013; Wachlin et al., 2017). Our work in Chapter 4 greatly expanded the range of $T_{\rm eff}$ explored for polluted WD models accounting for thermohaline mixing. In Chapter 4, we found that some DA WDs must accrete bulk earth composition at rates as large as $\dot{M}_{\rm acc} = 10^{13}\,{\rm g\,s^{-1}}$ for our models to match observed surface metal abundances.

In this chapter, we build on the results of Chapter 4 with further examination of the surface mixing processes relevant for heavy element pollution. We construct models that include these processes using the stellar evolution code `MESA`. We use `MESA` version 10398 unless otherwise stated. For models that include thermohaline mixing, we use `MESA` version 11191 (see Section 5.3.1 for a description of the relevant changes to the code that motivate using this version). `MESA` inlists and other input files necessary to reproduce our `MESA` models are available online at `https://doi.org/10.5281/zenodo.2541235`. In Section 5.1, we describe the hydrogen-dominated surface convection zones that metals first encounter when they accrete onto DA WDs. In Section 5.2, we quantify the individual element diffusion timescales for sedimentation beneath the convection zones in our `MESA` models, and provide tabulated results. In Section 5.3, we examine other forms of mixing that can be relevant in non-convective regions. These include a greatly refined and expanded treatment of thermohaline mixing (Section 5.3.1), as well as convective overshoot (Section 5.3.2). Our results confirm the findings of Chapter 4 that earth composition accretion rates approaching $\dot{M}_{\rm acc} = 10^{13}\,{\rm g\,s^{-1}}$ are necessary to match observed calcium abundances in DA WDs with $T_{\rm eff} \gtrsim 15,000\,{\rm K}$. We close with discussion and conclusions in Sections 5.4 and 5.5.

5.1 Surface Convection Zones in Pure Hydrogen

Polluting metals quickly mix into the WD surface convection zone, so that the base of this fully mixed region is where the gravitational sedimentation rate must be evaluated (Vauclair et al., 1979; Koester, 2009). Here we quantify the total mass, $M_{\rm cvz}$, in the surface convective layers of our `MESA` WD models with pure hydrogen atmospheres and compare to previous work.

To facilitate comparison to the work of Koester (2009, 2010), we adopt the ML2 convection prescription (Bohm & Cassinelli, 1971) with $\alpha_{\rm MLT} = 0.8$. This value of $\alpha_{\rm MLT}$ is similar to those calibrated against 3D convection by Tremblay et al. (2013, 2015), but it should be noted that the calibrated values show some variation with $T_{\rm eff}$. The depth of the surface convection zone is also sensitive to the surface boundary condition of the model. We find that the gray iterative atmosphere procedure in `MESA` (see MESA II) provides values of $M_{\rm cvz}$ in good agreement with Koester (2009) for $T_{\rm eff} \gtrsim 9,000\,{\rm K}$. At lower effective temperatures, we switch to the pre-computed DA WD atmosphere tables adapted from Rohrmann et al. (2012). When using these tables, `MESA` models attach to boundary conditions given at the optical depth $\tau_{\rm Ross} = 25$, so the tables are not suitable for WDs with very shallow convection zones that do not extend to $\tau_{\rm Ross} > 25$. Fortunately, the gray iterative atmosphere procedure is adequate for all cases of shallow convection zones, and it is only necessary to switch to the tables for cooler WDs with large convection zones. For the remainder of this work, we use models that switch from gray atmosphere boundary conditions to the WD atmosphere tables below $T_{\rm eff} = 9,000\,{\rm K}$.

Figure 5.1 shows a comparison of the mass of the surface convection zone between `MESA` WD models and the DA models of Koester (2009, 2010).[1] For hotter WDs where no surface convection is present ($T_{\rm eff} \gtrsim 15,000\,{\rm K}$), the mass exterior to the photosphere is the relevant parameter for pollution mixing calculations, so we show this value as well. The tables of Koester (2009) give whichever is larger of mass in the surface convection zone and mass exterior to the photosphere. The hydrogen ionization transition that drives convection results in a steep change in the convection zone mass around $10,000\,{\rm K} \lesssim T_{\rm eff} \lesssim 13,000\,{\rm K}$. We see small disagreements in the exact location of this feature, and otherwise are in excellent agreement with Koester (2009). Although the disagreement in mass at fixed $T_{\rm eff}$ can be up to an order of magnitude, the steep slope of the curve in this region means that small variations of $T_{\rm eff}$ within typical observational uncertainties can bring these values into agreement.

---

[1] Most recent tables found at `http://www1.astrophysik.uni-kiel.de/~koester/astrophysics/astrophysics.html`.

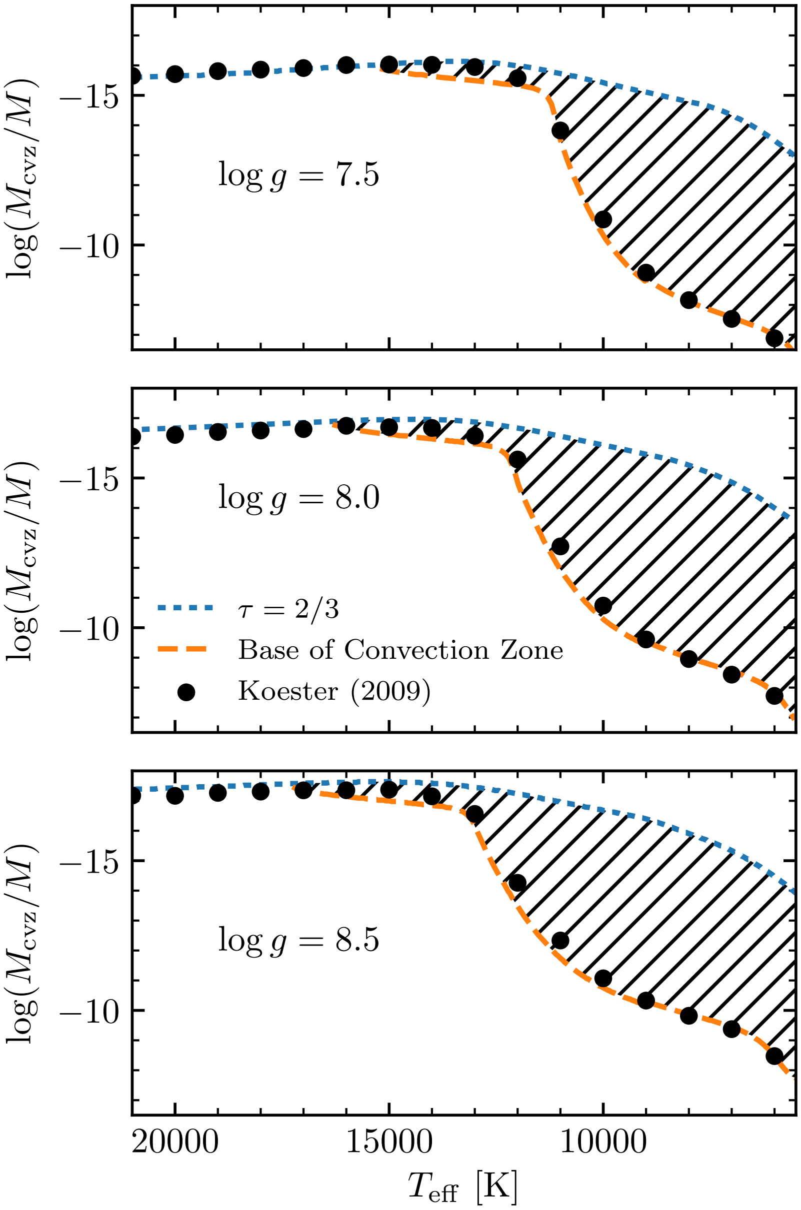

Figure 5.1: Comparison of the convection zone masses (orange lines) in nearly pure hydrogen atmospheres of `MESA` WD models of mass $0.38\,M_\odot$, $0.60\,M_\odot$, and $0.90\,M_\odot$ to those given by Koester (2009, black points) for $\log g = 7.5$, 8.0, and 8.5. The blue lines show the location of the photosphere in the `MESA` models, and the hatched regions indicate the fully mixed convection zones extending out to the photosphere.

5.2 Diffusion Timescales

With the structure of `MESA` WD models and convection zone masses established, diffusion timescales can now be calculated for all trace heavy elements. These timescales are essential to inferring accretion rates and compositions from observations of trace elements in the photosphere. Section 2 of Chapter 4 shows the equations relating these diffusion timescales to accretion rates and observable surface abundances. Here we only repeat a few key definitions for convenience. When no other mixing occurs beneath the surface convection zone, the sedimentation timescale for trace element i is

$$\tau_{\mathrm{diff},i} \equiv \frac{M_{\mathrm{cvz}}}{4\pi r^2 \rho v_{\mathrm{diff},i}} \ , \tag{5.1}$$

where r is the radius, ρ is the density, and $v_{\mathrm{diff},i}$ is the sedimentation velocity of element i evaluated at the base of the surface convection zone where it sinks away from the fully mixed surface region. An approximate expression for $v_{\mathrm{diff},i}$ for a trace diffusing element is given later in Equation (5.3), but in general our `MESA` models calculate diffusion velocities from a full solution of the Burgers equations (Burgers, 1969) as described in Chapters 2 and 3. For a constant accretion rate $\dot{M}_i$ of species i over timescales much longer than $\tau_{\mathrm{diff},i}$, the surface mass fraction approaches the equilibrium value

$$X_{\mathrm{eq},i} = \frac{\dot{M}_i}{M_{\mathrm{cvz}}} \tau_{\mathrm{diff},i} \ . \tag{5.2}$$

For observational inferences, it is assumed that this equilibrium state has been reached, so that the elemental accretion rate can be derived from the observed mass fraction as $\dot{M}_i = X_{\mathrm{obs},i} M_{\mathrm{cvz}} / \tau_{\mathrm{diff},i}$. We denote the total accretion rate as $\dot{M}_{\mathrm{acc}} \equiv \sum_i \dot{M}_i$.

5.2.1 `MESA` Diffusion Results

The diffusion velocities necessary to calculate diffusion timescales using Equation (5.1) are readily available from `MESA` models. We obtain these by simply introducing a polluting metal (e.g. ^{40}Ca) accreting at a rate of $\dot{M}_{\rm acc} = 10^7\,{\rm g\,s^{-1}}$. After accretion takes place for many diffusion timescales, so that the abundance in the surface convection zone has reached equilibrium, we calculate the diffusion timescale using Equation (5.1) along with the diffusion velocity reported by `MESA` from the solution of the Burgers equations. These diffusion calculations include thermal diffusion and properly account for any degree of electron degeneracy as described in Chapter 3.

Diffusion calculations according to the Burgers equations rely on coefficients calculated using a binary scattering formalism. The well-established coefficients of Paquette et al. (1986a) are based on a screened Coulomb potential treatment for calculating binary Coulomb collision cross sections. Recent updates to `MESA` (see Chapter 3) have included options for using the coefficients of Stanton & Murillo (2016), who provide an improvement upon this method with a more sophisticated treatment of screening. Table 5.1 shows some comparisons for diffusion timescales in a $0.6\,M_\odot$ WD including calculations using the coefficients of Paquette et al. (1986a). In general, both sets of coefficients give similar results except for the deepest convection zones, where the increased Coulomb screening due to electrons in the calculations of Stanton & Murillo (2016) allows for faster diffusion.

Table 5.1: Comparison of `MESA` and Koester (2009) results for the mass of the surface convection zone and diffusion timescales for ^{40}Ca on a $0.6\,M_\odot$ WD. The models of Koester (2009) adopt a fixed value of $\log g = 8.0$, so we include a column for $\log g$ from the `MESA` model to note how it varies slightly about this value as the WD cools. Columns labeled with $D_{\rm Paq}$ refer to diffusion calculations using the coefficients of Paquette et al. (1986a), and those labeled $D_{\rm SM}$ refer to calculations using the coefficients of Stanton & Murillo (2016). Columns labeled with Z_2+1 or Z_2-1 refer to calculations for which the charge of ^{40}Ca is taken to be 1 larger or smaller than the value given by the ionization calculations based on Paquette et al. (1986b).

$T_{\rm eff}$ [K]	$\log(M_{\rm cvz}/M)$		$\log g$	$\log(\tau_{\rm diff}/{\rm yr})$ for ^{40}Ca						
	Koester	`MESA`	`MESA`	Koester	`MESA`		`MESA` (Z_2+1)		`MESA` (Z_2-1)	
				($D_{\rm Paq}$)	($D_{\rm Paq}$)	($D_{\rm SM}$)	($D_{\rm Paq}$)	($D_{\rm SM}$)	($D_{\rm Paq}$)	($D_{\rm SM}$)
6000	-7.722	-7.8094	8.0342	4.2924	4.2449	4.13	4.2977	4.1827	4.1835	4.0684
7000	-8.432	-8.5222	8.0306	3.7125	3.7107	3.6139	3.7662	3.6695	3.6473	3.5513
8000	-8.954	-8.9849	8.0272	3.3303	3.4113	3.3372	3.4674	3.3923	3.3616	3.2908
9000	-9.607	-9.517	8.0238	2.8725	3.0408	2.9957	3.1009	3.0531	2.9715	2.9304
10000	-10.738	-10.251	8.0202	1.9997	2.476	2.4679	2.5493	2.5371	2.3884	2.3852
11000	-12.715	-11.872	8.0164	0.4845	1.1984	1.2236	1.3214	1.3478	1.0337	1.0566
12000	-15.618	-14.698	8.0127	-1.6941	-1.0767	-1.071	-0.81118	-0.80264	-1.5571	-1.5573
13000	-16.408	-16.103	8.0094	-2.359	-1.9677	-1.9629	-1.7151	-1.7073	-2.4523	-2.4534
14000	-16.672	-16.292	8.006	-2.6305	-2.0968	-2.0931	-1.8252	-1.8185	-2.5713	-2.5734
15000	-16.698	-16.43	8.0026	-2.6277	-2.1953	-2.1926	-1.9216	-1.9159	-2.6857	-2.6887
16000	-16.744	-16.622	7.9991	-2.622	-2.3333	-2.3318	-2.0573	-2.0526	-2.8272	-2.8312
17000	-16.634	-16.836	7.9953	-2.4688	-2.4941	-2.4939	-2.2153	-2.2119	-2.9901	-2.9952
18000	-16.586	-16.787	7.9914	-2.4213	-2.469	-2.4694	-2.1889	-2.1862	-2.9668	-2.9724
19000	-16.538	-16.703	7.9872	-2.3804	-2.4182	-2.4191	-2.1374	-2.1352	-2.9171	-2.9231
20000	-16.439	-16.644	7.983	-2.3077	-2.3847	-2.3862	-2.1033	-2.1015	-2.8849	-2.8913

Table 5.1 also shows comparisons to the diffusion timescales given by Koester (2009, see link in Footnote 1 for the most up-to-date diffusion timescale results), which employ the coefficients of Paquette et al. (1986a). When using these same coefficients, the `MESA` timescale results agree well as long as the convection zone depth is comparable. For $T_{\rm eff} \gtrsim 11,000\,{\rm K}$, the convection zone depths differ by up to an order of magnitude between `MESA` and Koester (2009), and the diffusion timescales disagree accordingly. Table 5.2 gives `MESA` diffusion timescales for ten commonly observed elements, using the coefficients of Stanton & Murillo (2016).

Table 5.2: `MESA` diffusion timescales for the $0.6\,M_{\odot}$ WD model calculated using the coefficients of Stanton & Murillo (2016). Supplemental tables for other WD masses are available at `https://doi.org/10.5281/zenodo.2541235` (Bauer, 2019).

$T_{\rm eff}$ [K]	$\log(M_{\rm cvz}/M)$	$\log(\tau_{\rm diff}/{\rm yr})$									
		^{12}C	^{16}O	^{23}Na	^{24}Mg	^{27}Al	^{28}Si	^{40}Ca	^{48}Ti	^{52}Cr	^{56}Fe
6000	-7.8094	4.2573	4.3303	4.0949	4.0564	4.001	3.8702	4.13	4.0304	3.931	3.89
7000	-8.5222	3.8338	3.9012	3.646	3.6249	3.4721	3.4464	3.6139	3.5067	3.4046	3.4617
8000	-8.9849	3.5523	3.6214	3.3551	3.3105	3.1875	3.1688	3.3372	3.1957	3.0915	3.185
9000	-9.517	3.2304	3.2723	2.9774	2.935	2.8664	2.8485	2.9957	2.8552	2.7713	2.8289
10000	-10.251	2.7752	2.7551	2.4842	2.4591	2.2849	2.3975	2.4679	2.3434	2.3276	2.3132
10500	-10.928	2.3481	2.2194	1.9873	1.8792	1.8257	1.973	1.9514	1.8086	1.9119	1.8567
11000	-11.872	1.7424	1.552	1.2795	1.0427	1.2254	1.3768	1.2236	1.1432	1.233	1.184
11500	-13.147	0.744	0.5792	0.2153	0.1798	0.3899	0.5494	0.2203	0.3178	0.2846	0.2136
12000	-14.698	-0.552	-0.7081	-1.3172	-0.8501	-0.6347	-0.6532	-1.071	-0.8808	-0.9153	-0.9472
12500	-15.953	-1.6971	-1.9663	-2.124	-1.6439	-1.6901	-1.7108	-1.8661	-1.9454	-1.9789	-2.0115
13000	-16.103	-1.9121	-2.0535	-2.2121	-1.74	-1.8271	-1.8073	-1.9629	-2.0423	-2.0772	-2.1094
13500	-16.203	-1.9954	-2.1254	-2.2838	-1.809	-1.9515	-1.8764	-2.0319	-2.1114	-2.1462	-2.1785
14000	-16.292	-2.0585	-2.1858	-2.3321	-1.87	-2.0932	-1.9374	-2.0931	-2.1725	-2.2074	-2.2272
15000	-16.43	-2.1621	-2.2885	-2.4473	-1.9693	-2.2683	-2.0368	-2.1926	-2.2721	-2.3071	-2.3393
16000	-16.622	-2.3042	-2.4307	-2.5896	-2.1081	-2.6023	-2.1757	-2.3318	-2.4114	-2.4464	-2.4786
17000	-16.836	-2.4658	-2.5932	-2.7529	-2.2694	-2.8193	-2.3373	-2.4939	-2.5737	-2.6088	-2.6411
18000	-16.787	-2.4429	-2.5704	-2.7301	-2.2449	-2.6484	-2.3128	-2.4694	-2.5493	-2.5843	-2.6167
19000	-16.703	-2.3906	-2.5212	-2.6809	-2.1946	-2.2487	-2.2625	-2.4191	-2.4989	-2.5339	-2.5663
20000	-16.644	-2.261	-2.4894	-2.6491	-2.1617	-2.2136	-2.2296	-2.3862	-2.466	-2.5009	-2.5333

5.2.2 Approaching Equilibrium

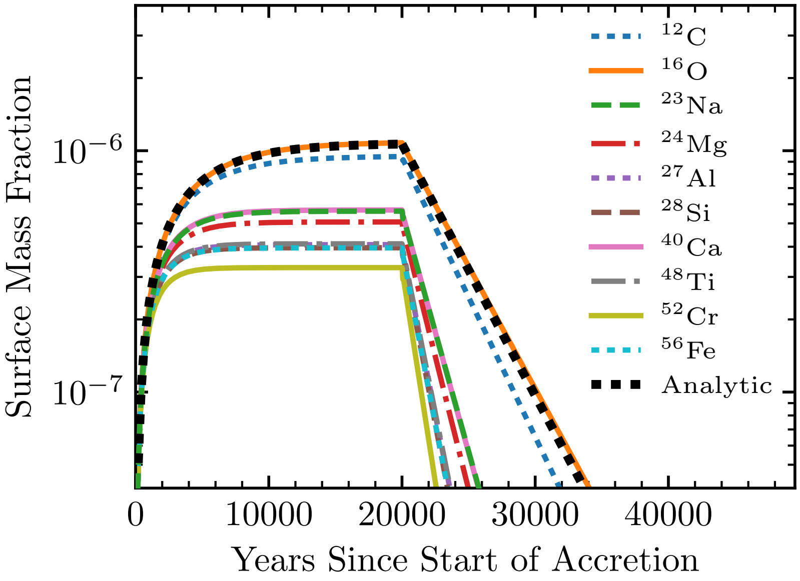

Figure 5.2: Mass fractions over time in a $0.6\,M_\odot$ WD model at $T_{\rm eff} = 8,000\,$K that accretes 10 isotopes at a rate of $10^7\,{\rm g\,s^{-1}}$ each for 20,000 years, after which accretion ends and the pollutants sediment away from the surface. The black dashed curve shows the analytic solution for ^{16}O with $\log(\tau_{\rm diff}/{\rm yr}) = 3.62$.

Figure 5.2 shows surface mass fractions for several accreting elements in a `MESA` model, first approaching equilibrium after accretion turns on and continues for many diffusion timescales, then sinking away after accretion shuts off. For comparison, this figure also shows the analytic solution described in Chapter 4 for this constant accretion rate for ^{16}O with a diffusion timescale of $\log(\tau_{\rm diff}/{\rm yr}) = 3.62$. This verifies that the metals approach the equilibrium surface mass fraction predicted by Equation (5.2) for the diffusion timescales given in Table 5.2. The accretion episode shown in Figure 5.2 has all elements accreting at equal rates ($10^7\,{\rm g\,s^{-1}}$ for each element) to illustrate the effects of the hierar-

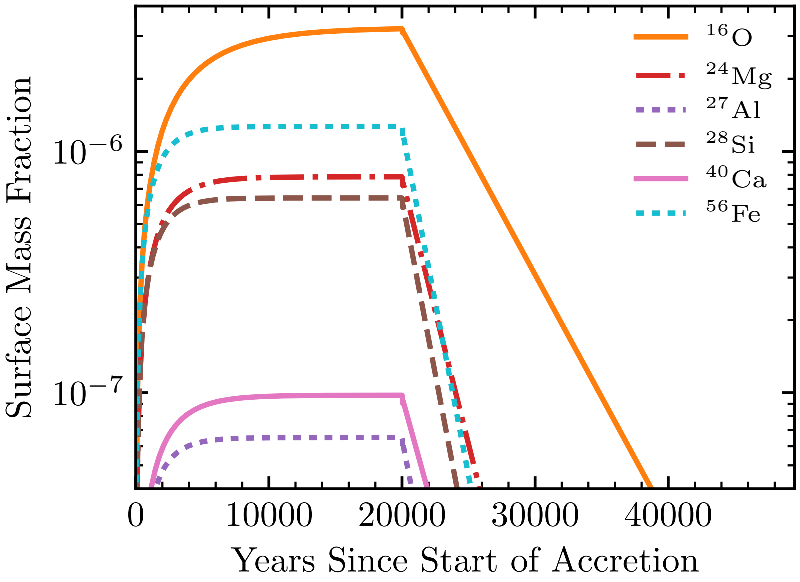

Figure 5.3: Mass fractions over time in a $0.6\,M_\odot$ WD model at $T_{\rm eff} = 8,000\,$K that accretes at a total rate of $10^8\,{\rm g\,s^{-1}}$ with bulk earth composition for $20,000$ years, after which accretion ends and the pollutants sediment away from the surface. Only the most abundant elements appear on the scale shown here.

chy of diffusion timescales. This manifests as a clear ordering of abundances, where those with the longest diffusion timescales appear as the most abundant over all phases. In contrast, Figure 5.3 shows a more realistic accretion scenario, where the elements accrete at the total rate $\dot{M}_{\rm acc} = 10^8\,{\rm g\,s^{-1}}$, but with the bulk earth abundance ratios of McDonough (2001). In this case, both the relative accreted mass fraction and diffusion timescale for each element play a role in establishing the final hierarchy of observed surface abundances. Neither of these calculations include thermohaline mixing (see Section 5.3.1).

5.2.3 Ionization States for Trace Metals

The partial ionization of metals in the surface layers relevant for pollution has important effects for the diffusion timescales. If we denote the background material in which diffusion takes place by the index 1 (hydrogen in the case of a DA WD atmosphere), and denote the pollutant by index 2, then in the limit of a trace pollutant ($n_2 \ll n_1$) its diffusion velocity can be expressed as (cf. Pelletier et al. 1986; Dupuis et al. 1992; Koester et al. 2014)

$$v_{\rm diff} = D_{12}\left[-\frac{\partial \ln c_2}{\partial r} + \left(\frac{Z_2}{Z_1}A_1 - A_2\right)\frac{m_{\rm p} g}{kT} + \left(\frac{Z_2}{Z_1} - 1\right)\frac{\partial \ln p_i}{\partial r} + \alpha_T \frac{\partial \ln T}{\partial r}\right] , \quad (5.3)$$

where $c_2 \equiv n_2/(n_1 + n_2)$ is the concentration of the pollutant, $p_i \equiv p_1 + p_2$ is the ion pressure, α_T is the thermal diffusion coefficient, and A and Z refer to the mass and charge of each species respectively. Note that this equation is appropriate for any degree of electron degeneracy (Pelletier et al., 1986), and it agrees with our `MESA` diffusion treatment based on the Burgers equations in the limit of trace particles diffusing in a hydrogen background. The charge of each species influences the diffusion velocity in two important ways: the direct influence on the forcing terms felt by each ion seen in Equation (5.3), and the influence of the charge of each particle on the Coulomb scattering that results in the diffusion coefficient D_{12}. The diffusion coefficient is related to the resistance coefficients used for `MESA` diffusion calculations described in Chapters 2 and 3 by $D_{ij} \propto K_{ij}^{-1}$. For Coulomb collisions, the resistance coefficients described in Chapter 2 scale with the charge approximately as $K_{ij} \propto (Z_i Z_j)^2$, and hence diffusion calculations can be very sensitive to the ionization treatment adopted for the partially ionized surface regions of WD models.

Formally, each ionization state of a given element may be treated as a separate species with its own integer charge Z_i for purposes of diffusion calculations. In order to simplify the problem, `MESA` calculations instead adopt an average state $\bar{Z}$ for each element as described in Chapters 2 and 3 so that each isotope corresponds to only one diffusion species. We use the ionization treatment of Paquette et al. (1986b) to find an average charge state for each diffusion species everywhere in the `MESA` model.[2]

Figure 5.4 displays some of the charges used as input for diffusion calculations reported in `MESA` WD models. Since the ionization procedure based on Paquette et al. (1986b) involves comparing ionization potentials to an effective threshold potential, it always selects an integer value for the average charge. This results in the stair-stepped profiles seen in Figure 5.4, which have been smoothed slightly to improve the numerical stability of diffusion calculations. The last columns of Table 5.1 present results from diffusion calculations for which the charge Z_2 is taken to be one larger or smaller than the value obtained from the Paquette et al. (1986b) routine. Comparison of these timescales quantifies the rough uncertainty associated with the average ionization calculations here.

Our diffusion calculations assume that every species is at least singly ionized. Diffusion coefficients for a neutral species require collision integrals for dipole scattering, which

---

[2] We note that the expression in Paquette et al. (1986b) for the depression of the continuum for ionization potentials contains a typo in Equation (21), where a factor of $\rho^{1/3}$ is missing from the last line. The `MESA` ionization routine instead follows Equation (3) of Dupuis et al. (1992), which correctly includes this factor. Our ionization treatment is very similar to that of Koester (2009), who also notes correcting the missing factor of $\rho^{1/3}$ for the most recent calculations hosted on his website (see link in Footnote 1).

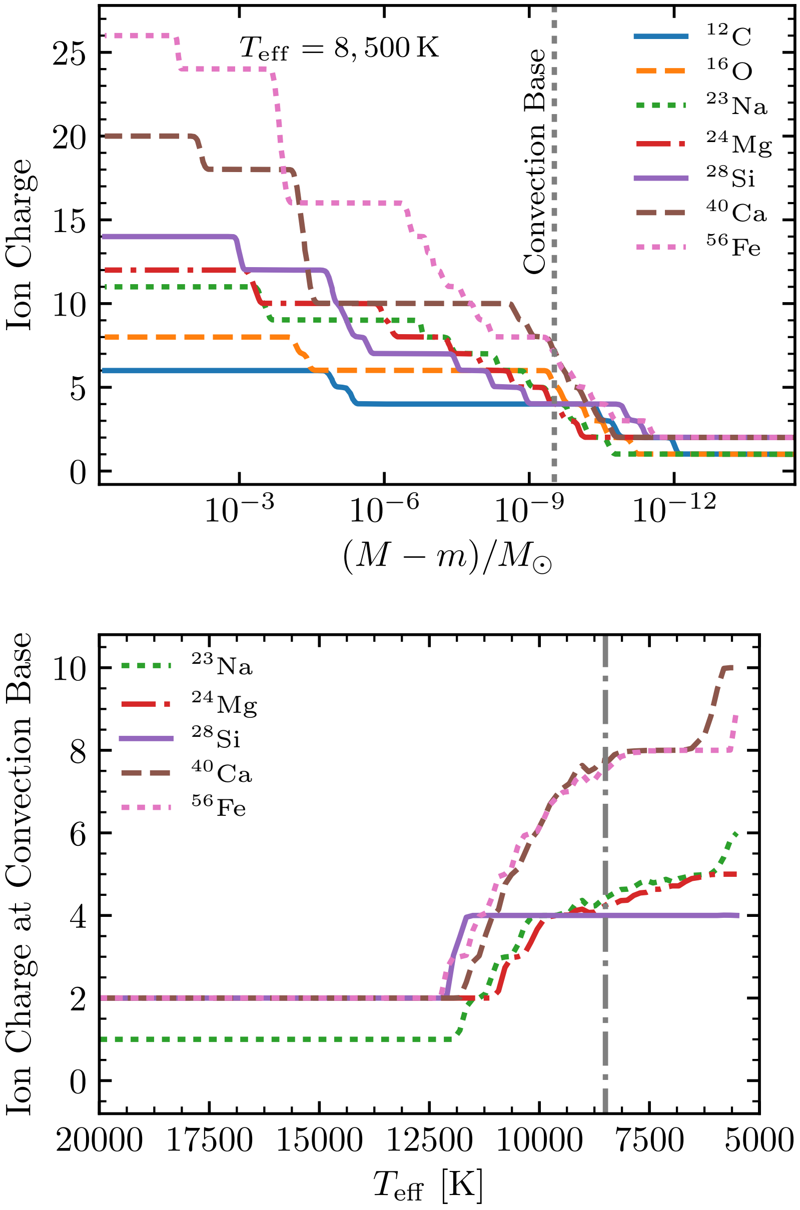

Figure 5.4: *Upper Panel:* Profiles of average ion charges in the outer layers of a $0.6\,M_\odot$ WD at $T_{\rm eff} = 8,500\,\rm K$. *Lower Panel:* Ion charges at the base of the convection zone as a function of WD temperature for a $0.6\,M_\odot$ WD. The gray dashed line indicates the temperature of the model shown in the upper panel.

result in significantly smaller collision cross sections and correspondingly faster diffusion timescales (Appendix C). Options for such diffusion coefficients are not currently available in `MESA`. Since diffusion fluxes for neutral elements can be much faster than those for singly ionized elements, even a small fraction of neutral particles in the relevant layer can significantly modify overall sedimentation timescales, and it is no longer appropriate to treat ionization with an average charge $\bar{Z} < 1$. Diffusion timescales presented in this work are only accurate for models where surface temperatures are hot enough or surface convection zones reach depths sufficient for at least single ionization of pollutants. Due to a thin or absent surface convection zone, these conditions fail to be satisfied around $T_{\rm eff} \approx 15,000\,{\rm K}$, and corresponding disagreement is evident between our results and those of Koester (2009) in Table 5.1 for this regime.

5.3 Other Mixing

We now explore additional mixing other than element diffusion beneath the convective layer. We focus on two fluid processes that can cause additional mixing: the thermohaline instability and convective overshoot.

5.3.1 Thermohaline Mixing

In the context of WD pollution, Deal et al. (2013) were the first to explore the possibility that accreted metals in WD atmospheres may lead to thermohaline instability. Subsequent work by Wachlin et al. (2017) confirmed the importance of the resulting mixing.

In Chapter 4, we extended the parameter space for polluted WDs where thermohaline instability may occur, finding that thermohaline mixing significantly modifies inferred accretion rates in hydrogen-atmosphere WDs with $T_{\rm eff} \gtrsim 10,000\,{\rm K}$, with some rates reaching $\dot{M}_{\rm acc} \approx 10^{13}\,{\rm g\,s^{-1}}$ for $T_{\rm eff} \gtrsim 15,000\,{\rm K}$. Our exploration in Chapter 4 was limited to WD models of mass $M = 0.6\,M_\odot$ ($\log g = 8.0$). We now expand upon that work with models of other masses to allow interpolation in $\log g$. We also adopt a refined treatment of thermohaline mixing based upon the work of Brown et al. (2013), which is calibrated against 3D simulations.

Two criteria must be satisfied for the thermohaline instability to be active. First, there must be an inverted molecular weight gradient in a region that is stable to convection:

$$\nabla_T - \nabla_{\rm ad} < \frac{\varphi}{\delta}\nabla_\mu < 0 \ , \tag{5.4}$$

where $\nabla_T = (\partial \ln T / \partial \ln P)$ is the temperature gradient, $\nabla_{\rm ad} = (\partial \ln T / \partial \ln P)_s$ is the adiabatic temperature gradient, $\nabla_\mu = (\partial \ln \mu / \partial \ln P)$ is the mean molecular weight gradient, $\varphi = (\partial \ln \rho / \partial \ln \mu)_{P,T}$, and $\delta = -(\partial \ln \rho / \partial \ln T)_{P,\mu}$. The instability is then driven by thermal exchange of perturbed fluid elements with their surroundings, whereupon a density contrast due to ∇_μ leads to further mixing. Thus, the second criterion for thermohaline instability is that the magnitude of the molecular weight gradient ∇_μ and the thermal diffusivity κ_T must be large enough to excite the instability before particle diffusivity κ_μ within a perturbed fluid element can adjust its composition (Baines & Gill, 1969; Garaud, 2018):

$$\frac{(\varphi/\delta)\nabla_\mu}{\nabla_T - \nabla_{\rm ad}} > \frac{\kappa_\mu}{\kappa_T} \ . \tag{5.5}$$

Assuming that heat transport is radiative, the thermal diffusivity is

$$\kappa_T = \frac{4acT^3}{3\kappa\rho^2 C_P} \ , \tag{5.6}$$

where κ is the opacity and C_P is the heat capacity. The particle diffusivity is derived from the diffusion coefficients of the various polluting metals that determine the molecular weight of a fluid element.

The mixing that results from thermohaline instability can be approximated with a coefficient that scales with thermal diffusivity and the molecular weight gradient (Kippenhahn et al., 1980):

$$D_{\rm th} = \alpha_{\rm th} \kappa_T \frac{3}{2} \frac{(\varphi/\delta)\nabla_\mu}{\nabla_T - \nabla_{\rm ad}} \ , \tag{5.7}$$

where $\alpha_{\rm th}$ is a dimensionless efficiency parameter. In Chapter 4, we explored inferences for polluted WD accretion rates using the mixing treatment of Equation (5.7) with $\alpha_{\rm th} = 1$. Note that this mixing treatment does not explicitly check the criterion for instability given in Equation (5.5), but in Chapter 4 we verified that it is satisfied for regions of interest in polluted WDs where thermohaline mixing may occur.

`MESA` also offers a thermohaline mixing treatment based on the work of Brown et al. (2013), which is calibrated against their 3D hydrodynamic simulations. This treatment explicitly accounts for the criterion in Equation (5.5) and produces a mixing coefficient designed to scale smoothly to zero as conditions approach the limit defined there. Figure 5.5 shows the surface Ca mass fraction in polluted $0.6\,M_\odot$ WD models after accreting for many diffusion timescales, with thermohaline mixing according to either Equation (5.7) or Brown et al. (2013). These `MESA` models also include element diffusion at all

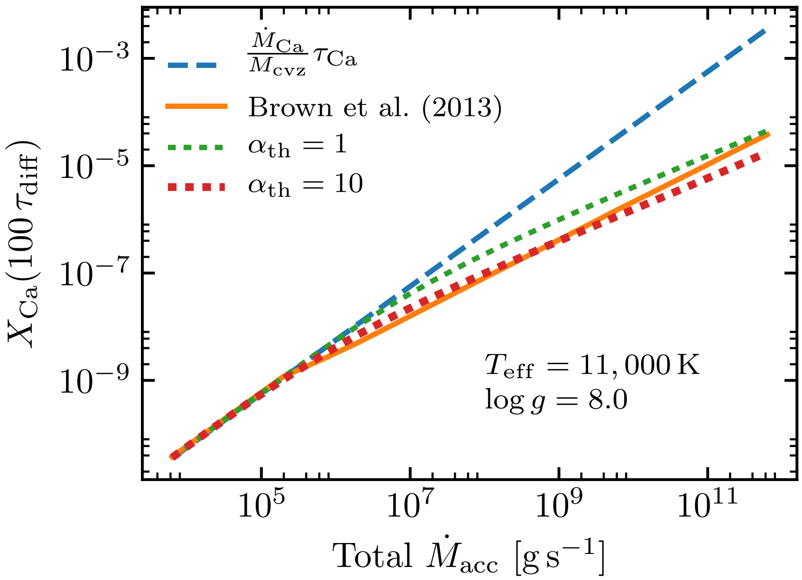

Figure 5.5: Surface Ca mass fraction after 100 diffusion timescales as a function of total metal accretion rate for a $0.6\,M_\odot$ ($\log g = 8.0$) WD model accreting metals in bulk earth ratios. Curves labeled with values of $\alpha_{\rm th}$ use the thermohaline mixing prescription of Equation (5.7), while the orange curve employs the Brown et al. (2013) routine in `MESA` version 11191. The blue dashed line shows the expectation according to Equation (5.2) if the diffusive sedimentation timescale governs surface abundances.

times. Figure 5.5 shows that results for polluted WD models using thermohaline mixing based on Brown et al. (2013) are qualitatively similar to those using Equation (5.7) with $1 \lesssim \alpha_{\rm th} \lesssim 10$.

For small accretion rates, thermohaline mixing is not active, and the equilibrium surface mass fractions shown in Figure 5.5 match the prediction of Equation (5.2) for the diffusion timescales given in Table 5.2. Above a critical accretion rate $\dot{M}_{\rm crit}$, the metal concentration at the surface builds up a sufficient magnitude of ∇_μ to excite thermohaline instability, and `MESA` models including thermohaline mixing diverge from the prediction of Equation (5.2). For a $T_{\rm eff} = 11,000\,{\rm K}$ WD, Figure 5.5 shows that this critical rate is

Table 5.3: Critical accretion rates in our $0.6\,M_\odot$ `MESA` WD models above which thermohaline mixing modifies the equilibrium surface mass fractions from the prediction of Equation (5.2). This assumes accretion of material with bulk earth composition (McDonough, 2001).

$T_{\rm eff}$ [K]	6,000	7,000	8,000	9,000	10,000	11,000	$> 12{,}000$
$\dot{M}_{\rm crit}$ [$\rm g\,s^{-1}$]	10^{12}	10^{10}	10^{9}	10^{8}	10^{7}	10^{6}	$< 10^{4}$

around $\dot{M}_{\rm crit} \approx 10^6\,{\rm g\,s^{-1}}$. Table 5.3 gives values of this critical rate for `MESA` WD models over a range of $T_{\rm eff}$. For models with $T_{\rm eff} > 12,000\,{\rm K}$, the surface convection zones are so small that thermohaline mixing is active for all accretion rates in the range that we explored ($\dot{M}_{\rm acc} > 10^4\,{\rm g\,s^{-1}}$).

The curve shown for the Brown et al. (2013) prescription in Figure 5.5 varies slightly from the similar plot shown in Figure 4.3 in the previous chapter. This is due to a small correction to the `MESA` implementation of this routine that affects the mixing coefficient in the regime near the limit of thermohaline instability. This correction was introduced after `MESA` release version 10398, which was used for Chapter 4, but it is present in `MESA` version 11191, which we use for all models that include thermohaline mixing in this chapter. The asymptotic analysis regimes presented in Appendix B of Brown et al. (2013) form the basis of the 1D mixing treatment. In particular, their Appendix B.3 addresses the regime in which the fluid is near the limit imposed by Equation (5.5). The method relies on an expansion in the parameter

$$\epsilon \equiv 1 - \frac{\kappa_\mu/\kappa_T}{(\varphi/\delta)\nabla_\mu/(\nabla_T - \nabla_{\rm ad})} \ , \tag{5.8}$$

which is assumed to be small. The implementation for this regime in `MESA` version 11191 ensures that this parameter is sufficiently small whenever applying the method of Brown et al. (2013) Appendix B.3, yielding more consistent results than version 10398. With these corrections, the `MESA` implementation shows more mixing near the boundary of thermohaline instability defined by Equation (5.5). Hence, models employing the Brown et al. (2013) routine in `MESA` version 11191 diverge from the prediction of diffusion alone at the lower accretion rates seen in Figure 5.5.

Using this updated thermohaline mixing treatment, we construct a large grid of accreting DA WD models as in Chapter 4. Effective temperatures of the models span the range $6,000\,\mathrm{K} < T_{\rm eff} < 20,500\,\mathrm{K}$, and accretion rates for each temperature span $10^4\,\mathrm{g\,s^{-1}} < \dot{M}_{\rm acc} < 10^{12}\,\mathrm{g\,s^{-1}}$. All models accrete bulk earth material (McDonough, 2001). We tabulate values of $X_{\rm Ca}$ present at the surface of each model after 100 diffusion timescales as defined by Table 5.2. We then interpolate on these tables to map observed values of $X_{\rm Ca}$ to total inferred accretion rates $\dot{M}_{\rm acc}$. We also expand upon the results of Chapter 4 by providing these tables for models with three different WD masses to allow interpolation in $\log g$: $M_{\rm WD}/M_\odot = 0.38, 0.60, 0.90$ ($\log g \approx 7.5, 8.0, 8.5$). These tables are available along with simple python interpolation routines at `https://doi.org/10.5281/zenodo.2541235` (Bauer, 2019).

Figure 5.6 shows inferred accretion rates based on these tables for the same sample of polluted DA WDs (Koester & Wilken, 2006) that was discussed in Chapter 4. In general, accretion rates are similar to the inferences made in Chapter 4, though the very highest inferences are slightly lower than the previous highest values. A few WDs also show

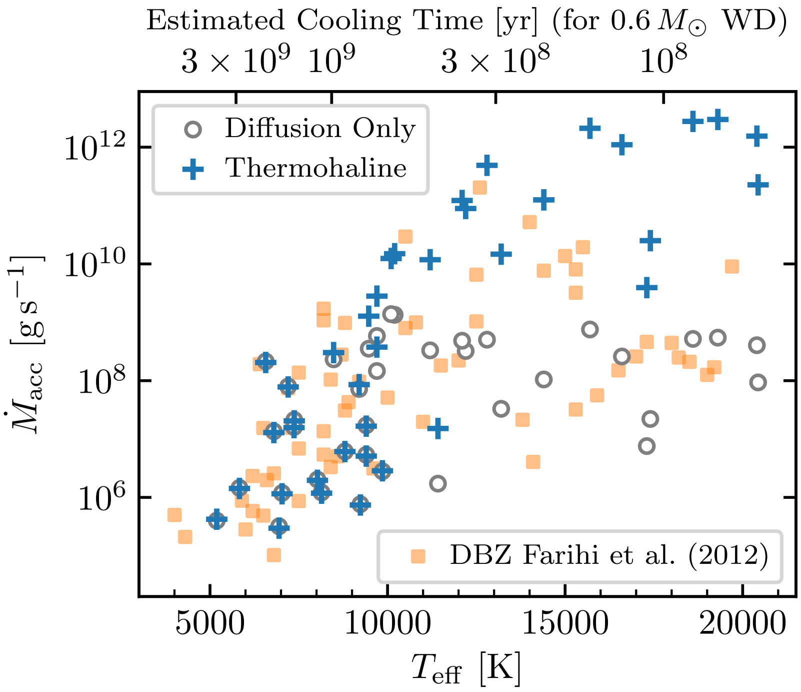

Figure 5.6: Accretion rates inferred with (blue crosses) and without (open circles) thermohaline mixing from the observed Ca abundances for the 38 WDs given in Table 1 of Koester & Wilken (2006). Models that include thermohaline mixing follow the prescription of Brown et al. (2013). Accreting material is assumed to have bulk earth composition. The orange points show the rates inferred for He-atmosphere WDs by Farihi et al. (2012) for comparison. The top axis shows estimated WD cooling time based on a `MESA` model of a 0.6 $M_\odot$ DA WD.

adjustments due to observed values of $\log g$ different from the value of 8.0 assumed in Chapter 4, especially for $9,000\,\mathrm{K} < T_{\mathrm{eff}} < 13,000\,\mathrm{K}$, where the surface convection zone masses are especially sensitive to $\log g$ (see Figure 5.1). However, the overall qualitative picture remains the same. Thermohaline mixing causes inferred accretion rates to increase by several orders of magnitude for WDs with $T_{\mathrm{eff}} > 10,000\,\mathrm{K}$!

Non-constant Accretion Rates

The previous section shows results when accretion occurs in a steady state for many diffusion timescales, allowing the surface metal pollution to approach equilibrium abundances. However, if the source of accretion supplied to the surface varies with time, this can introduce complexities in the ∇_μ profile that sets the conditions for thermohaline instability according to Equations (5.4) and (5.5). In particular, heavy elements must be continually supplied to the surface to maintain $\nabla_\mu < 0$ in the mixing region relevant to observable pollution. If the accretion rate decreases significantly, the gradient necessary for thermohaline instability can disappear, halting thermohaline mixing.

As a simple illustration, we show in Figure 5.7 a `MESA` model including thermohaline mixing that accretes at a constant rate until it approaches equilibrium, followed by a cessation of accretion after $10\,\mathrm{yr} \approx 100\tau_{\mathrm{diff}}$. Due to the sudden disappearance of an inverted ∇_μ in the surface region governing observable metal pollution, thermohaline mixing is no longer relevant. Instead, the diffusion timescales of Table 5.2 dictate the fast exponential decay of metal pollution at the photosphere. These results contrast with the diffusion-only `MESA` model shown in Figure 5.3, where the same diffusion timescale

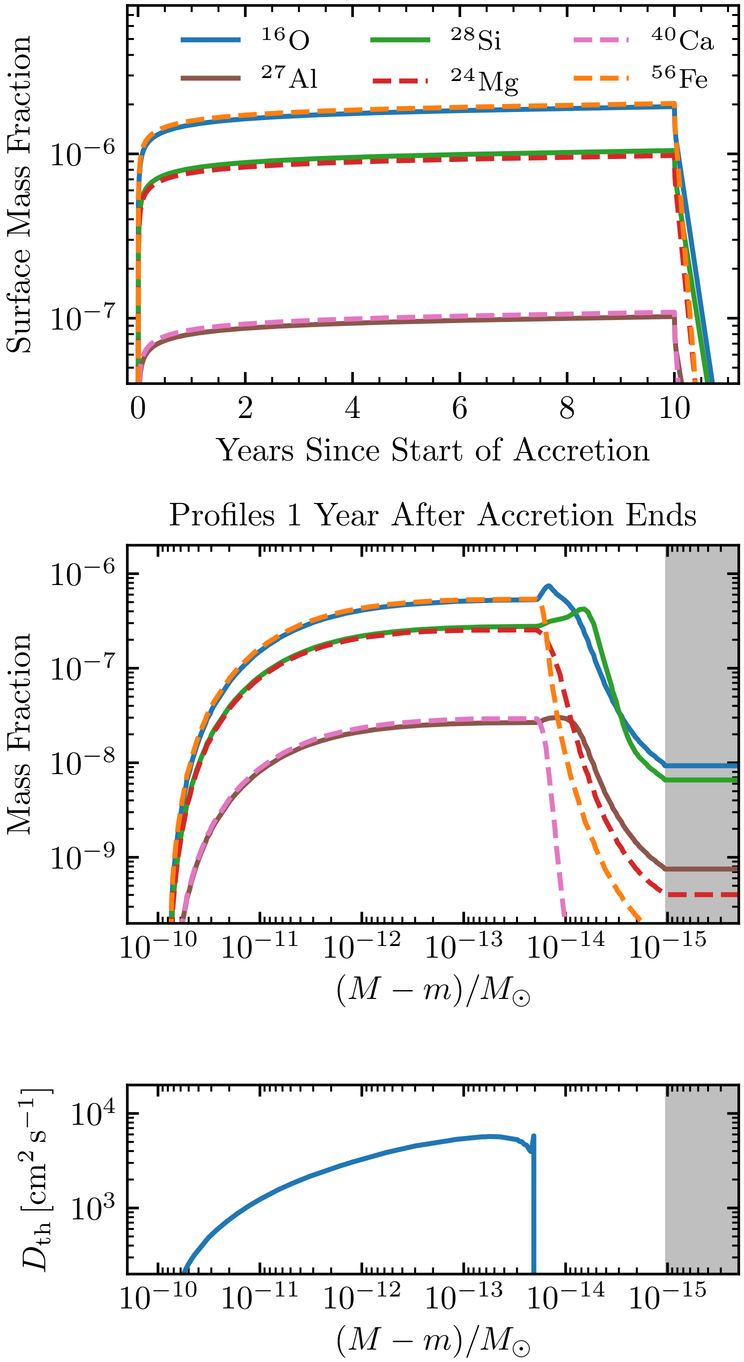

Figure 5.7: A $0.6\,M_\odot$, $T_{\rm eff} = 12,000\,$K `MESA` DA WD model including thermohaline mixing. This model accretes at a rate of $10^8\,{\rm g\,s^{-1}}$ for $10\,{\rm yr} \approx 100\tau_{\rm diff}$, after which accretion ends and metals sediment away from the photosphere. The lower panels show the interior profile of the model one year after accretion has ceased. The gray shaded region represents the fully mixed surface convection zone.

governs both the approach to equilibrium and exponential decay after accretion ceases.

Figure 5.7 also demonstrates important features involving differentiation of the accreted composition. When thermohaline mixing is active near the surface during the constant accretion phase, no composition differentiation occurs because fluid elements that dominate the mixing transport all elements together. However, once thermohaline mixing ceases near the surface, individual particle diffusion dominates, and significant differentiation quickly occurs within a few diffusion timescales. The middle panel of Figure 5.7 shows that the deeper layers where thermohaline mixing is still active reflect the accreted bulk earth composition (McDonough, 2001), but separate diffusion timescales for each element quickly rearrange the surface composition. Elements with the shortest diffusion timescales such as ^{56}Fe disappear from the surface much sooner, even when they were previously among the most abundant due to the accreted composition.

Helium-dominated Atmospheres

WDs with helium-dominated atmospheres do not experience the same corrections due to thermohaline mixing that hydrogen-dominated atmospheres do. Two effects conspire to greatly reduce the potential for a ∇_μ large enough to excite thermohaline instability. First, the mean molecular weight of the dominant background material (He) is more than double that in the case of a hydrogen atmosphere, so the contrast with accreting metals is not as severe. Second, surface convection zones for helium atmospheres contain much more mass than hydrogen at a given temperature (Koester, 2009). This dilutes accreted metals and prevents the buildup of a significant ∇_μ below the convection zone.

For example, we constructed a $0.59\,M_\odot$ `MESA` WD model with $T_{\rm eff} = 18,000\,{\rm K}$ and a pure He atmosphere. We found that the surface convection zone mass of this model was $M_{\rm cvz} = 8 \times 10^{-8}\,M_\odot$, and diffusion timescales for accreted metals were on the order of 10^5 years. These values agree with the tables of Koester (2009) for $\log g = 8.0$ DB WDs. We explored `MESA` runs for this WD model accreting bulk earth composition at rates in the range $10^4\,{\rm g\,s^{-1}} < \dot{M}_{\rm acc} < 10^{12}\,{\rm g\,s^{-1}}$. We included thermohaline mixing in the runs using the treatment of Equation (5.7) with $\alpha_{\rm th} = 10$ (the `MESA` treatment based on Brown et al. (2013) is not applicable here because it assumes a hydrogen-dominated background). Even for the highest accretion rates, we find adjustments of at most one order of magnitude to inferred accretion rates compared to calculations that assume no thermohaline mixing (Figure 5.8). Figure 5.6 shows that typical accretion rates inferred for DB WDs in this temperature range are 10^8–$10^{10}\,{\rm g\,s^{-1}}$, and our `MESA` models show negligible corrections due to thermohaline mixing in this regime. The surface convection zone grows up to three orders of magnitude larger for cooler WDs (Koester, 2009), and the largest rates inferred for DB WDs only reach $10^{11}\,{\rm g\,s^{-1}}$, so thermohaline mixing will be inconsequential for He-atmosphere WDs with $T_{\rm eff} \lesssim 18,000\,{\rm K}$.

Below $T_{\rm eff} \approx 16,000\,{\rm K}$, the cool, dense, neutral helium at the surface of the WD falls outside the regime covered by opacity tables currently available in `MESA` (see MESA I). The code is therefore not able to set a physical outer boundary condition for the model below this temperature. Tabulated outer boundary conditions such as those used in the case of hydrogen-dominated atmospheres (Section 5.1) have been implemented in other

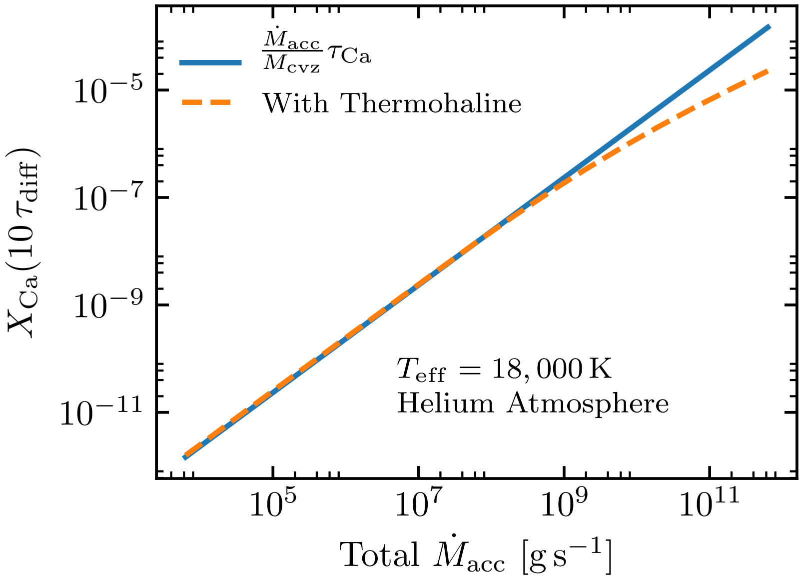

Figure 5.8: Surface Ca mass fraction after accreting bulk earth material for 10 diffusion timescales for a $T_{\rm eff} = 18,000\,{\rm K}$ `MESA` WD model with a helium-dominated atmosphere.

WD codes (e.g., Camisassa et al., 2017), but no such option is currently available in `MESA`. In the context of polluted WDs, it is also unclear whether atmosphere conditions tabulated for pure helium would be sufficient, since opacity may be sensitive to contaminating metals through effects such as $\rm He^-$ free-free absorption. Without the ability to set an appropriate outer boundary condition, `MESA` models cannot give reliable structures for the outer layers and depths of surface convection zones. A more thorough investigation of polluted WDs with helium-dominated atmospheres in `MESA` awaits extensions to atmosphere capabilities that can account for these issues.

Rotation

Rotational mixing and its interplay with other fluid processes can be important in stars (Sengupta & Garaud, 2018). This potential impact is quantified with the Rossby number $\mathrm{Ro} = U/2\Omega L$, where Ω is the rotational frequency, and U and L are the characteristic velocity and length scale for the relevant fluid process. Large values of the Rossby number indicate that rotation is not expected to have a strong influence, while $\mathrm{Ro} \lesssim 1$ indicates potential for significant modifications. Sengupta & Garaud (2018) studied the effect of rotation on thermohaline mixing in stellar interiors, where they derived the Rossby number in an actively mixing region as

$$\mathrm{Ro} \sim \sqrt{\frac{N^2}{4\Omega^2}\frac{(\varphi/\delta)\nabla_\mu}{\nabla_T - \nabla_{\mathrm{ad}}}} \ , \tag{5.9}$$

where N is the Brunt-Väisälä frequency. In a non-degenerate WD atmosphere, this frequency is of order $N^2 \sim g/H$, where $H = k_{\mathrm{B}}T/m_{\mathrm{p}}g$ is the local pressure scale height. For our polluted WD models experiencing moderate amounts of thermohaline mixing, we estimate $(\varphi/\delta)\nabla_\mu/(\nabla_T - \nabla_{\mathrm{ad}}) \sim 10^{-4}$ (cf. Chapter 4). We can therefore rewrite Equation (5.9) in terms of the critical rotation rate $\Omega_{\mathrm{crit}} = \sqrt{GM/R^3}$ as

$$\mathrm{Ro} \sim 10^{-2}\sqrt{\frac{R}{H}}\left(\frac{\Omega_{\mathrm{crit}}}{\Omega}\right) \ . \tag{5.10}$$

This requires $\Omega/\Omega_{\mathrm{crit}} \gtrsim 10^{-2}$ for rotation to be important ($\mathrm{Ro} \lesssim 1$). However, typical isolated WD rotation periods are around one day (Hermes et al., 2017), while the critical rotation period is on the order of a few seconds, so we do not expect rotation to influence the thermohaline mixing in typical polluted WDs.

Thermohaline mixing has also been discussed as a mechanism for explaining observed surface abundances in low-mass giant stars (Charbonnel & Zahn, 2007; Denissenkov & Pinsonneault, 2008; Cantiello & Langer, 2010), but this may require an implausibly large mixing efficiency $\alpha_{\rm th} > 100$ for implementations such as Equation (5.7). This mixing efficiency appears to be inconsistent with the mixing found in our models based on Brown et al. (2013). Sengupta & Garaud (2018) suggested that the interplay of rotation with thermohaline instability may enhance mixing near the cores of giant stars. Since we estimate that rotation would be irrelevant for thermohaline mixing in polluted WDs, this may alleviate the apparent tension between thermohaline mixing efficiency inferred in these different regimes.

5.3.2 Overshoot

Convective overshoot may cause fluid motions that can keep composition thoroughly mixed well below the formal boundary for convective instability according to the Ledoux criterion (Freytag et al., 1996; Koester, 2009; Tremblay et al., 2015), even in the absence of thermohaline instability. This will lead to a larger effectively mixed region and longer diffusion timescales for a given $T_{\rm eff}$ (Brassard & Fontaine, 2015; Tremblay et al., 2017).

To estimate mixing due to overshoot beneath the convective zone, we follow the results of Tremblay et al. (2015) and use a diffusion coefficient that decays exponentially with pressure scale height:

$$D_{\rm overshoot}(r) = D_0 \exp\left(-\frac{2|r - r_0|}{H_P}\right) \ , \tag{5.11}$$

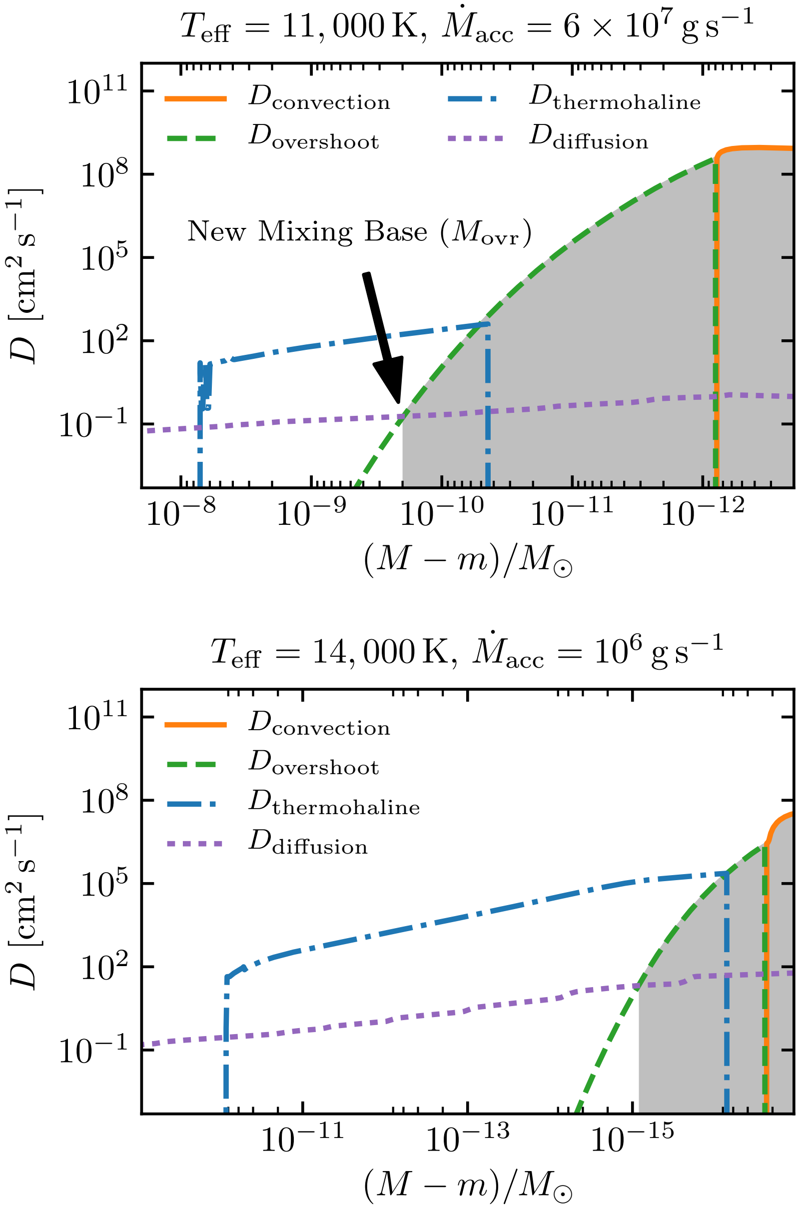

Figure 5.9: Mixing coefficient profiles for two `MESA` models. The gray shaded region represents the extent of surface layers that are expected to be fully mixed regardless of accretion rate, encompassing a mass of $M_{\rm ovr}$. The element diffusion coefficient shown for $D_{\rm diffusion}$ is that of iron in hydrogen. Choosing a different element to represent the particle diffusion coefficient would result in small changes to the crossover point that defines $M_{\rm ovr}$, but the steep decline of $D_{\rm overshoot}$ makes these variations negligible.

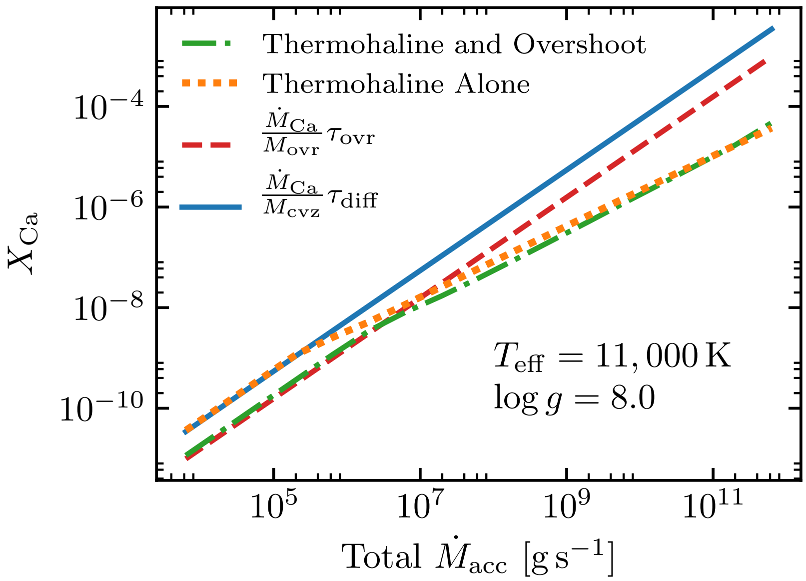

Figure 5.10: Surface Ca mass fraction after running `MESA` models for many diffusion timescales. All models accrete bulk earth composition. The models for thermohaline alone are the same as those in Section 5.3.1. The models including overshoot were run for $\approx 10\,\tau_{\rm ovr}$ due to the fact that $\tau_{\rm ovr} \gg \tau_{\rm diff}$.

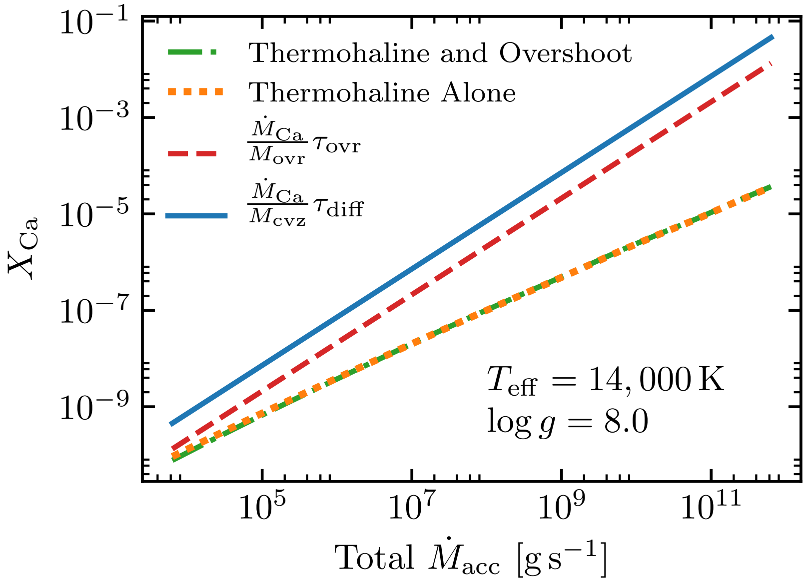

Figure 5.11: Same as Figure 5.10 but with a model at $T_{\mathrm{eff}} = 14{,}000\,\mathrm{K}$. Overshoot does not cause changes because significant thermohaline mixing occurs even at very low accretion rates.

where r_0 is the radial coordinate of the base of the convection zone, H_P is the pressure scale height there, and D_0 is the mixing coefficient from MLT near that location. Figure 5.9 shows the resulting diffusion coefficient profiles for two `MESA` models. In the absence of thermohaline mixing, this will lead to a new mass of the fully mixed surface region (M_{ovr}) defined by the location where the overshoot mixing decays to where element diffusion takes over ($D_{\mathrm{overshoot}} < D_{\mathrm{diffusion}}$, see Figure 5.9). There is then a corresponding new diffusion timescale for each element

$$\tau_{\mathrm{ovr},i} \equiv \frac{M_{\mathrm{ovr}}}{4\pi r^2 \rho v_{\mathrm{ovr},i}} \ , \tag{5.12}$$

where ρ, r, and $v_{\mathrm{ovr},i}$ are all evaluated at the base of the new mixing region defined by

$M_{\rm ovr}$. The equilibrium observable abundance of an accreted element will then be

$$X_{{\rm eq},i} = \frac{\dot{M}_i}{M_{\rm ovr}} \tau_{{\rm ovr},i} \tag{5.13}$$

instead of the analogous value given in Equation (5.2).

Figure 5.10 shows how observable abundances of accreting metals change when including this form of overshoot in our `MESA` models. For models at $T_{\rm eff} = 11,000\,{\rm K}$, the new diffusion timescale for Ca is $\tau_{\rm ovr} = 1300\,{\rm yr}$, almost 100 times larger than the timescale without overshoot. The larger mixing region means that accreted metals are more diluted for a given accretion rate, and so larger accretion rates are needed for thermohaline mixing to cause the observable abundances to diverge from the prediction of Equation (5.13). Still, for accretion rates of $\dot{M}_{\rm acc} > 10^7\,{\rm g\,s^{-1}}$, thermohaline mixing begins to dominate the final observed abundance, and overshoot causes only small adjustments when thermohaline mixing is active (see also the upper panel of Figure 5.9). For the case of a $T_{\rm eff} = 14,000\,{\rm K}$ WD shown in Figure 5.11, overshoot extends the small surface mixing region to $M_{\rm ovr} \approx 8 \times 10^{-16}\,M_\odot$ (see lower panel in Figure 5.9), but this is still so thin that thermohaline mixing dominates even for modest accretion rates.

While the results shown in this section may serve as a useful qualitative description of effects that can be expected from overshoot, it is likely that the overshoot mixing prescription given in Equation (5.11) is too simplistic for WD pollution applications. Simulations are beginning to probe regimes specific to convective overshoot in WDs (Montgomery & Kupka, 2004; Tremblay et al., 2015; Kupka et al., 2018), and they appear to show that a simple exponential decay in the diffusion coefficient is only accurate within a few scale heights of the convective boundary. Extrapolation down to the much smaller diffusion coefficients relevant for particle diffusion is likely inaccurate. Simulations by Lecoanet et al. (2016) found overshoot mixing that decays with a Gaussian profile ($D_{\text{overshoot}} \propto \exp[-(r-r_0)^2/2H^2]$ for some scale height H) rather than the exponential of Equation (5.11). A few more recent results appear to confirm this Gaussian overshoot profile in other contexts (Jones et al., 2017; Korre et al., 2019). This faster decay of the diffusion coefficient would imply that the extra extent of overshoot mixing is smaller than what is shown in Figure 5.9. We therefore refrain from a complete exploration of `MESA` models including overshoot until simulations can provide better constraints on overshoot mixing well below convective boundaries.

Our results are sufficient to conclude that overshoot will have negligible effects on most accretion rate inferences for $T_{\text{eff}} \gtrsim 12,000\,\text{K}$, where thin surface mixing regions result in strong concentrations of metals that make thermohaline mixing dominant. For lower temperatures, Figure 5.10 suggests that overshoot may cause significant adjustments to accretion rate inferences in cases where thermohaline mixing is not active. Even at higher temperatures, the new timescales due to overshoot may be important for decay phases where supply of fresh accreted material has ended and there is nothing to maintain the ∇_μ needed to drive thermohaline instability near the surface mixing region. In this case, the M_{ovr} and τ_{ovr} parameters will govern the exponential decay of observable surface abundances.

5.4 Discussion

A significant fraction of WDs show evidence of pollution (Koester et al., 2014), and if this fraction represents the fraction of the lifetime of each individual WD that it is polluted, then Figure 5.6 may be taken as approximately showing a complete history of accretion rates experienced over a WD lifetime. In this case, the total mass of planetesimal material accreted over a WD lifetime would be dominated by the high rates experienced by young WDs, yielding a high estimate of $M_{\rm tot} \sim (3 \times 10^8\,{\rm yr})(10^{12}\,{\rm g\,s^{-1}}) \sim 10^{28}\,{\rm g}$. However, Koester et al. (2014) point out that the Ca based sample used to construct Figure 5.6 may be biased toward objects that are especially heavily polluted, since the optical Ca lines used to select this sample require higher Ca abundances to be detectable for $T_{\rm eff} \gtrsim 15,000\,{\rm K}$ as total WD flux moves primarily into the UV. While this is unlikely to change the accretion rates inferred for the objects shown in Figure 5.6, it could hide a much larger intrinsic scatter in the accretion rates for young DA WDs. Therefore, $10^{28}\,{\rm g}$ could be an overestimate of the total mass accreted over a WD lifetime.

This sample of polluted WDs may reveal that some young WDs are undergoing short timescale bursts of accretion such as those suggested by Rafikov (2011b) and Metzger et al. (2012). This may help explain the discrepancy with DBZ WDs for $T_{\rm eff} \gtrsim 15,000\,{\rm K}$. The rates here are too high to be explained by Poynting-Robertson drag (Rafikov, 2011a), but rare runaway bursts would leave very different observational signatures for DA and DB WDs (Farihi et al., 2012). DA WDs approach a quasi-equilibrium surface abundance within days or years in this temperature range even for our `MESA` models including thermohaline mixing. On the other hand, the diffusion timescales in DB WDs are of order 10^5-10^6 years, and bursts lasting less than 10^4 years would never approach an equilibrium surface pollution level suggesting a high rate. Instead, DB WD surfaces may represent a more accurate estimate of accretion rates averaged over their much longer diffusion timescales. A more conservative mass estimate for total planetesimal material may then be $M_{\rm tot} \sim (3 \times 10^8\,{\rm yr})(10^{10}\,{\rm g\,s^{-1}}) \sim 10^{26}\,{\rm g}$.

Alternative processes could supply polluting material for longer timescales at rates higher than the limits of Poynting-Robertson drag, e.g., collisional cascades (Kenyon & Bromley, 2017a,b) or viscous evolution of earth-mass dust disks (van Lieshout et al., 2018). Hence, short bursts are not strictly necessary to explain the rates shown in Figure 5.6, but longer timescale processes may then require that the planetesimal environments form with significantly different amounts of mass around DA and DB WDs. Wyatt et al. (2014) found that stochastic accretion of a distribution of planetesimal sizes may be able to explain some discrepancies in inferred accretion rates for DA and DB WDs without the need to appeal to large bursts, but this analysis assumed accretion rates inferred without accounting for thermohaline mixing.

Finally, we note that some authors have pointed out trends of inferred accretion rates that decline with WD age over timescales of Gyr (e.g., Hollands et al., 2018; Chen et al., 2019), consistent with slow depletion of the planetesimal reservoirs that can obtain highly eccentric orbits on which they will eventually be tidally disrupted (e.g., Debes et al., 2012; Mustill et al., 2018). Our results appear to suggest that this decline may be more dramatic during the first Gyr of evolution when thermohaline mixing is accounted for. In particular, the broken power-law for accretion rates over time used by Chen et al. (2019) may not be necessary for rates inferred using our `MESA` models. Instead, a single power-law may work for all WD ages, consistent with the rate at which asteroids dynamically encounter the WD in the model of Chen et al. (2019).

5.5 Conclusions

We have confirmed the result of Chapter 4 that thermohaline mixing in polluted DA WDs with $T_{\rm eff} \gtrsim 10,000\,{\rm K}$ requires accretion rates several orders of magnitude larger than calculations assuming only gravitational sedimentation. We have provided results from an expanded grid of models to allow interpolation in $\log g$ as well as $T_{\rm eff}$ (`https://doi.org/10.5281/zenodo.2541235`, Bauer, 2019). We also find that thermohaline mixing is inconsequential in polluted DB WDs with $T_{\rm eff} \lesssim 18,000\,{\rm K}$ due to much more massive surface convection zones. Polluted DA WDs experience a regime of accretion rates low enough that thermohaline mixing is not active (Table 5.3), and so Table 5.2 provides diffusion timescales based on our `MESA` models. These timescales are also relevant for WDs where accretion is no longer ongoing, as they govern the exponential decay of metals sinking away from the surface where thermohaline mixing is no longer active, even when it was active during accretion. Finally, we have also provided a qualitative description of the effects of convective overshoot, though we refrain from a full exploration of its effects due to quantitative uncertainty in the overall extent of overshoot. However, we note that for WDs with thin surface convection zones ($T_{\rm eff} \gtrsim 12,000\,{\rm K}$), thermohaline mixing dominates down to layers deeper than overshoot can extend, and hence we do not expect significant modifications to inferred accretion rates in this regime.

Chapter 6

Electron Captures on ^{14}N as a Trigger for Helium Shell Detonations

Many accreting white dwarfs (WDs) are discovered when a thermonuclear instability (i.e. nova) occurs on their surface. These outcomes depend on the accreting fuel, the accretion rate, $\dot{M}$, and the WD mass. The growing AM CVn class of binaries are WDs accreting from a Roche lobe filling helium donor (Nelemans et al., 2004). No hydrogen is seen. Recent observations are beginning to unveil one possible class of progenitors for these systems, tight sdB+WD binaries ($P_{\rm orb} < 100\,{\rm min}$) that should make contact within the sdB star's helium burning lifetime (Geier et al., 2013; Kupfer et al., 2017). Due to the large He shells that are likely to accumulate prior to the onset of the initial thermonuclear instability, such systems are of interest as potential environments for helium detonations that can lead to ".Ia" supernovae or even double detonation supernovae (Nomoto, 1982;

Woosley & Weaver, 1994; Bildsten et al., 2007; Shen & Bildsten, 2009, 2014; Woosley & Kasen, 2011; Brooks et al., 2015).

When accreting from the outer, unburned layers of a He burning star, the isotope ^{14}N is present with a mass fraction set by the initial stellar metallicity, $X_{14} \approx 0.01(Z/0.02)$. When the accretor is a WD, this ^{14}N is an important isotope, as it captures an electron when densities above $1.25 \times 10^6\,\mathrm{g\,cm^{-3}}$ are reached. The resulting ^{14}C then undergoes the reaction $^{14}\mathrm{C}(\alpha,\gamma)^{18}\mathrm{O}$ that can trigger a thermonuclear flash (Hashimoto et al., 1986). This process, known as the NCO chain, requires the accumulation of a dense shell prior to the initiation of any thermonuclear instability, and is the subject of our study.

Hashimoto et al. (1986) showed that this reaction chain can lead to an earlier ignition than expected from the 3α reaction alone when accreting He onto a He WD, and Iben et al. (1987) and Shen & Bildsten (2009) noted its potential importance for accretion onto C/O WDs. Woosley & Weaver (1994) included the NCO chain in their models of sub-Chandrasekhar helium detonations. Piersanti et al. (2001) discussed the influence of NCO burning on the location of the ignition point for large, degenerate He envelopes on C/O WDs formed at constant $\dot{M} \approx 10^{-8}\,M_\odot\,\mathrm{yr}^{-1}$. They concluded that NCO burning only marginally decreased accumulated He layer mass, and noted that NCO burning did not lift degeneracy and prevent instability. Woosley & Kasen (2011) highlighted the role of the NCO chain in their survey of C/O WDs accreting He at $\dot{M} = (1-10) \times 10^{-8}\,M_\odot\,\mathrm{yr}^{-1}$, finding that the electron captures modify the neutron excess of the burned material and reduce the density at which the thermonuclear runaway initiates. This $\dot{M}$ and WD mass regime is coincident with that realized in the sdB donor star scenario (Iben et al., 1987; Brooks et al., 2015) and so needs a thorough investigation.

Our exploration of NCO ignitions in accreted He envelopes on C/O WDs using `MESA` confirms the importance of the NCO chain for systems accreting at rates corresponding to sdB+WD scenarios. Section 6.1 describes the relevant reaction rates used as input for `MESA`, relying on the recent work of Paxton et al. (2015) and Schwab et al. (2015) for the electron capture physics and Johnson et al. (2009) for α captures on ^{14}C. Section 6.2 shows `MESA` results for models at constant $\dot{M}$ to explore broad trends in the influence of the NCO chain. Section 6.3 shows `MESA` results that include binary evolution with resulting variable accretion rates. These binary results are qualitatively different from what is found at constant $\dot{M}$, demonstrating the importance of self-consistent evolution coupling detailed binary evolution and accretion histories to modeling of the accreting WD up to ignition of the He. The system CD $-30°11223$ (Geier et al., 2013) serves as a case study that naturally illustrates the importance of models including both NCO reactions and realistic binary accretion histories.

6.1 The NCO Reaction Chain

Unless otherwise specified, all modeling presented in this work relies on `MESA` version r8118 with reaction networks including weak reactions between ^{14}N and ^{14}C as well as α-capture onto ^{14}C. This section describes the details of the rates for these reactions, which together make up the complete NCO chain.

6.1.1 Weak Reactions for ^{14}N and ^{14}C

Tabulated rates for the electron-capture and beta-decay reactions linking ^{14}N and ^{14}C are not included in `MESA` version r8118. In order to incorporate these important rates, we used a modified version of `MESA`'s on-the-fly weak reaction rate capabilities[1] (Paxton et al., 2015; Schwab et al., 2015; Paxton et al., 2016; Schwab et al., 2016). The rate of interest is that of the ground state ($^{14}\mathrm{N} : J^{\pi} = 1^{+}$) to ground state ($^{14}\mathrm{C} : J^{\pi} = 0^{+}$) transition. This a has Q-value of $0.1565\,\mathrm{MeV}$, corresponding to a threshold density of $\rho_{\mathrm{th}} = 1.156 \times 10^{6}\,\mathrm{g\,cm^{-3}}$ for electron fraction $Y_{\mathrm{e}} = 0.5$. The ft-value for ^{14}C beta decay is $\log(ft/\mathrm{s}) = 9.04$ (Ajzenberg-Selove, 1991), with the ft-value for electron capture being a factor of 3 lower, corresponding to the ratio of the spin degeneracies $(2J_{\mathrm{N}} + 1)/(2J_{\mathrm{C}} + 1)$.

Previous application of these capabilities (Schwab et al., 2015; Martínez-Rodríguez et al., 2016) focused on the high-density regime where the degenerate electrons are ultra-relativistic, and therefore we must make one slight modification to the treatment included in `MESA` version r8118. The equations implemented assume that G, the Coulomb barrier factor, can be approximated as a constant and thus removed from the phase space integral. This is true in the ultra-relativistic regime, where $G = \exp(\pi\alpha Z) \approx 1.2$ as well as in the non-relativistic regime, where $G = 2\pi\alpha Z \approx 0.32$ (Fuller et al., 1980). However, the density where the electron Fermi energy $E_{\mathrm{F}} \approx m_{\mathrm{e}}c^{2}$ is $\rho \approx 2 \times 10^{6}\,\mathrm{g\,cm^{-3}}$ (for $Y_{\mathrm{e}} = 0.5$), near ρ_{th}. We are not in either limiting regime. Fuller et al. (1985) remove G from the integral by replacing it with a suitably defined average value, $\langle G \rangle$. These values

---

[1] Our inlists and patches for `MESA` r8118 are available at http://mesastar.org.

vary with density and temperature; however, we find the choice of a single average value $\langle G_\beta \rangle = 0.75$ (for beta decay) and $\langle G_{\rm ec} \rangle = 0.95$ (for electron capture) reproduces the rates calculated without removing G from the integral to within $\approx 10\%$ over the regime of interest ($5 \leq \log(\rho/{\rm g\,cm^{-3}}) \leq 7$ and $7 \leq \log(T/{\rm K}) \leq 9$).

Figure 6.1 shows these weak reaction rates. We confirmed that these rates agree with the rates in Hashimoto et al. (1986) to within $\approx 10\%$ at the relevant, near-threshold densities. The work of Woosley & Kasen (2011) used the Hashimoto et al. (1986) results. As discussed by Hashimoto et al. (1986), the most important aspect of these rates is the shift in equilibrium composition from ^{14}N (at $\rho < \rho_{\rm th}$) to ^{14}C (at $\rho > \rho_{\rm th}$) over a narrow range in density $\Delta \log \rho \approx (k_{\rm B}T)/E_{\rm F}$.

The rates in our `MESA` calculations include an additional correction not present in the rates shown in Figure 6.1; this "ion Coulomb correction" corresponds to the energetic cost to change the ion charge in the dense plasma. We evaluate the magnitude of this effect using the ion chemical potential from Potekhin et al. (2009). At the densities and temperatures of interest, this energy difference is $\Delta\mu_{\rm ion} \approx 7\,{\rm keV}$. This corresponds to an increase of the threshold density by $\Delta\rho_{\rm th} \approx 10^5\,{\rm g\,cm^{-3}}$. When referring to the threshold density for our `MESA` models, we use the value $\rho_{\rm th} = 1.25 \times 10^6\,{\rm g\,cm^{-3}}$ which accounts for this correction.

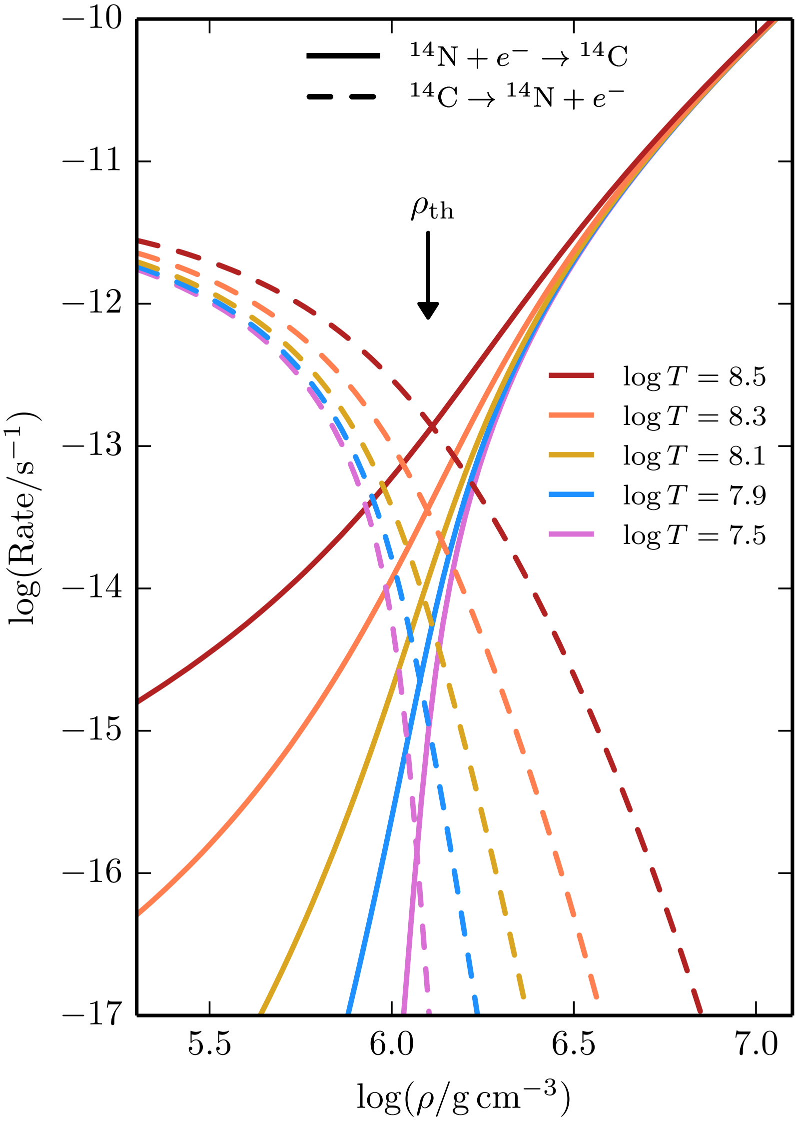

Figure 6.1: Rates for electron-capture and beta-decay reactions linking ^{14}N and ^{14}C (for $Y_{\mathrm{e}} = 0.5$). So as to compare with previous work, this plot neglects the Coulomb correction.

6.1.2 The ^{14}C$(\alpha,\gamma)^{18}$O Rate

Historically, the ^{14}C$(\alpha,\gamma)^{18}$O rate has been uncertain by several orders of magnitude due to a poorly constrained, near-threshold, 3^- resonance in ^{18}O at 6.404 MeV, which dominates the rate for temperatures $3\times10^7\,\mathrm{K} < T < 3\times10^8\,\mathrm{K}$. Figure 6.2 shows the rate given in equation (1) of Hashimoto et al. (1986), as well as the rate from Iliadis et al. (2010), via the JINA Reaclib database (Cyburt et al., 2010), that was adopted as the default rate in `MESA` (Paxton et al., 2011, 2013). The contrast between these rates illustrates the large historical uncertainty associated with the temperature regime dominated by the resonance.

For this work we use the measurements of Johnson et al. (2009) for the temperature regime $T > 3\times10^7\,\mathrm{K}$, where the rate is dominated by the 3^- and 4^+ resonances. We have adopted the rates given in their equation (12) for those resonances, with a claimed uncertainty of just 35% for the 3^- resonance. Thus, the historical uncertainty associated with the ^{14}C$(\alpha,\gamma)^{18}$O rate is now greatly reduced in the temperature regime relevant for our problem. The contributions from these resonances are plotted in Figure 6.2 for comparison to the other full rates. For lower temperatures where these resonances do not dominate, we switch back to using the rate from Iliadis et al. (2010) for simplicity, though the rate is so small in this region that it will not be significant. The lower panel of Figure 6.2 shows the total resulting rate that we have adopted for this work relative to the default rate found in `MESA` version r8118 from Iliadis et al. (2010).

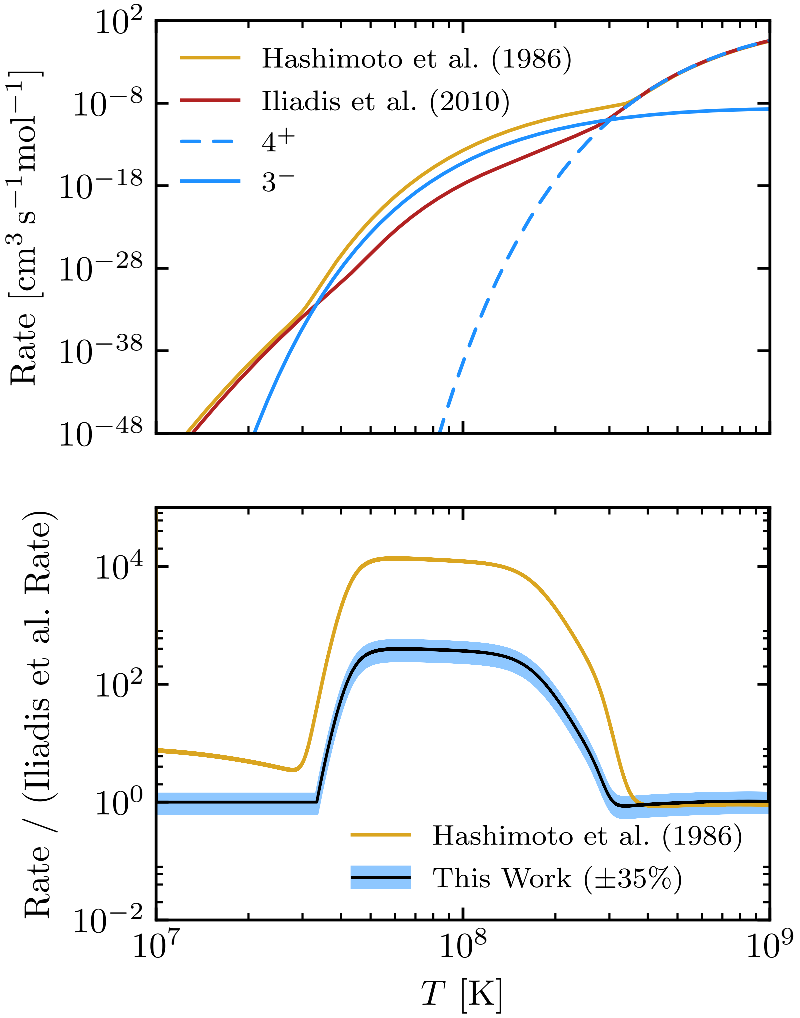

Figure 6.2: *Upper Panel:* The ^{14}C$(\alpha,\gamma)^{18}$O rates from Hashimoto et al. (1986) and Iliadis et al. (2010), along with the specific resonances that dominate for $T > 3 \times 10^7$ K as measured by Johnson et al. (2009). *Lower Panel:* The ^{14}C$(\alpha,\gamma)^{18}$O rates from this work and Hashimoto et al. (1986) relative to the rate from Iliadis et al. (2010).

6.1.3 Example of He Accretion onto a He WD

To exhibit how `MESA` compares to prior work, we used `MESA` to reproduce the He WD evolution scenarios described in section 4 and figure 5 of Hashimoto et al. (1986). A $0.3\,M_\odot$ He WD model accretes He until the center is compressed and heated enough to undergo an NCO induced thermonuclear runaway. In Figure 6.3, we compare cases with different rates for the $^{14}\mathrm{C}(\alpha,\gamma)^{18}\mathrm{O}$ step in the NCO chain, as well as a case where NCO reactions are omitted from the network. For higher accretion rates, the temperature of the core is high enough that electron captures are the rate limiting step for the NCO chain, and hence we see no difference in the evolution tracks when using different $^{14}\mathrm{C}(\alpha,\gamma)^{18}\mathrm{O}$ rates. For lower accretion rates, however, the core evolution tracks reach well beyond the threshold density for electron captures, so that electron captures are no longer the rate limiting step for the NCO chain. Instead, the tracks lie in a temperature region where $^{14}\mathrm{C}$ burning dominates the net NCO rate, and we see that the improved $^{14}\mathrm{C}(\alpha,\gamma)^{18}\mathrm{O}$ rate (Johnson et al., 2009) substantially changes the final outcome for case B. In case C, He burning triggers the thermonuclear runaway before NCO has a chance, so the $^{14}\mathrm{C}(\alpha,\gamma)^{18}\mathrm{O}$ rate ends up being irrelevant for igniting the flash.

6.2 NCO Reactions and Helium Accretion

Due to the steep density dependence of the electron capture rates, we expect the NCO chain to play a significant role only when the density at the base of an accreted He shell reaches values above the threshold density of $\rho_{\mathrm{th}} = 1.25 \times 10^6\,\mathrm{g\,cm^{-3}}$ prior to

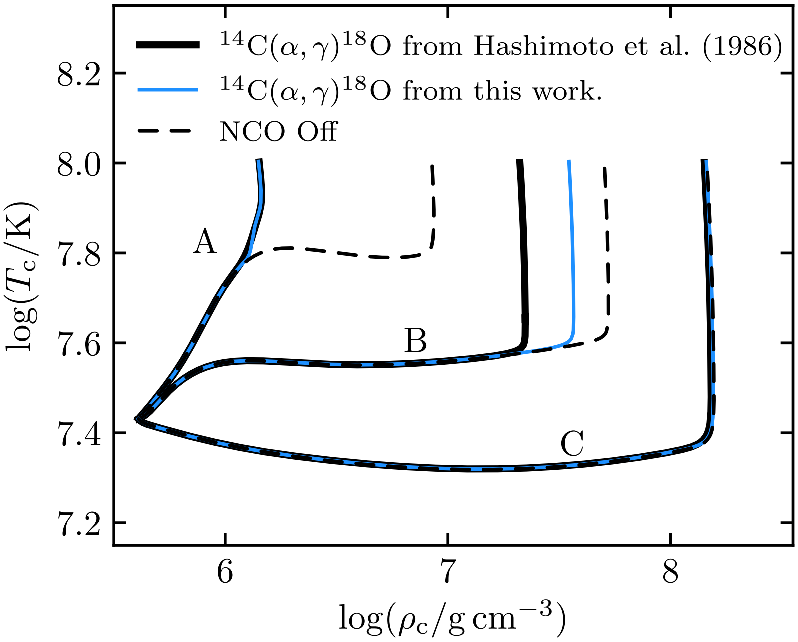

Figure 6.3: `MESA` models of He accretion onto a He WD reproducing those shown by figure 5 in Hashimoto et al. (1986). Solid black lines show core ignition via the NCO chain using the ^{14}C$(\alpha,\gamma)^{18}$O rate given by Hashimoto et al. (1986) equation (1). Dashed lines show ignition when NCO burning is ignored and only 3α plays a role. Solid blue lines show the result from NCO ignition using the ^{14}C$(\alpha,\gamma)^{18}$O rate described in Section 6.1.2 of this work. The three different cases are constant He accretion rates of (A) $10^{-8}\,M_\odot\,\mathrm{yr}^{-1}$, (B) $10^{-9}\,M_\odot\,\mathrm{yr}^{-1}$, and (C) $3\times10^{-10}\,M_\odot\,\mathrm{yr}^{-1}$.

thermonuclear ignition. The rate at which NCO burning occurs can be governed by the electron captures on ^{14}N (and hence the local density), but most of the energy production from the chain is supplied by the subsequent burning of ^{14}C. Once the right conditions are reached for electron captures onto ^{14}N, alpha captures occur on the freshly produced ^{14}C, releasing $Q = 6.227\,\mathrm{MeV}$ per ^{14}C consumed. At constant pressure and for ions strongly in the liquid state, complete consumption of the ^{14}C at abundance $X_{14} \ll 1$ in a helium background leads to a temperature change of

$$\Delta T = \frac{2}{21}\frac{Q}{k_{\mathrm{B}}}X_{14} \approx 7 \times 10^{7}\,\mathrm{K}\left(\frac{X_{14}}{0.01}\right). \tag{6.1}$$

This entropy input is often large enough to trigger a full He burning runaway, and 3α burning quickly takes over as the dominant energy source once NCO has raised the temperature enough to initiate a runaway.

In contrast, when NCO reactions are ignored and ignition depends on 3α reactions alone, the models experience a later ignition in a different location. Helium burning via 3α is much more temperature sensitive than the electron captures that initiate the NCO chain, which depend primarily on the density. Despite previous work on mixing and viscous heating due to shear instabilities for white dwarfs accreting helium (Yoon & Langer, 2004a; Yoon et al., 2004; Yoon & Langer, 2004b), we ignore these effects in our models. Recent work by Piro (2015) suggests that this should be justified due to the baroclinic instability inhibiting development of shear instabilities at depths relevant for helium ignition.

6.2.1 Constant $\dot{M}$ Without NCO

As a baseline for comparison, we first created a grid of WD models over a range of constant He accretion rates until they reached 3α ignition in their shells. During the accretion phase, the location of peak temperature lies outside the base of the accreted envelope due to the generic feature of a temperature inversion at these accretion rates, where electron conduction competes with the compressional heating by draining heat into the core and cooling the most dense inner layers of the envelope (Nomoto, 1982). Since temperature inversions can cause a 3α based runaway to happen at a location in the accumulated material other than the base, the convective shell mass can be less than the total accreted mass. The top panel of Figure 6.4 shows the mass of the accumulated (solid) and convective (dashed) He shells at the moment of the instability triggered by the 3α reactions alone. The convective shell mass is defined here as all mass exterior to the location of the thermonuclear runaway, which will be swept up in the convection that occurs as a result of unstable ignition.

Models to the left of the solid point in Figure 6.4 accumulated sufficiently large He envelopes to achieve a density above $1.25 \times 10^6\,\mathrm{g\,cm^{-3}}$ at the base of the He layer prior to 3α ignition, implying that for $\dot{M} < 4 \times 10^{-8}\,M_\odot\,\mathrm{yr}^{-1}$, the NCO reaction chain should provide extra heat near the dense base of the envelope. For all models accreting at constant $\dot{M}$, we assume an initial core temperature of $T_\mathrm{c} = 2 \times 10^7\,\mathrm{K}$, appropriate for sdB+WD binary scenarios where the WD certainly has $10 - 100\,\mathrm{Myr}$ to cool before the system makes contact. Lower core temperatures do not significantly impact the results.

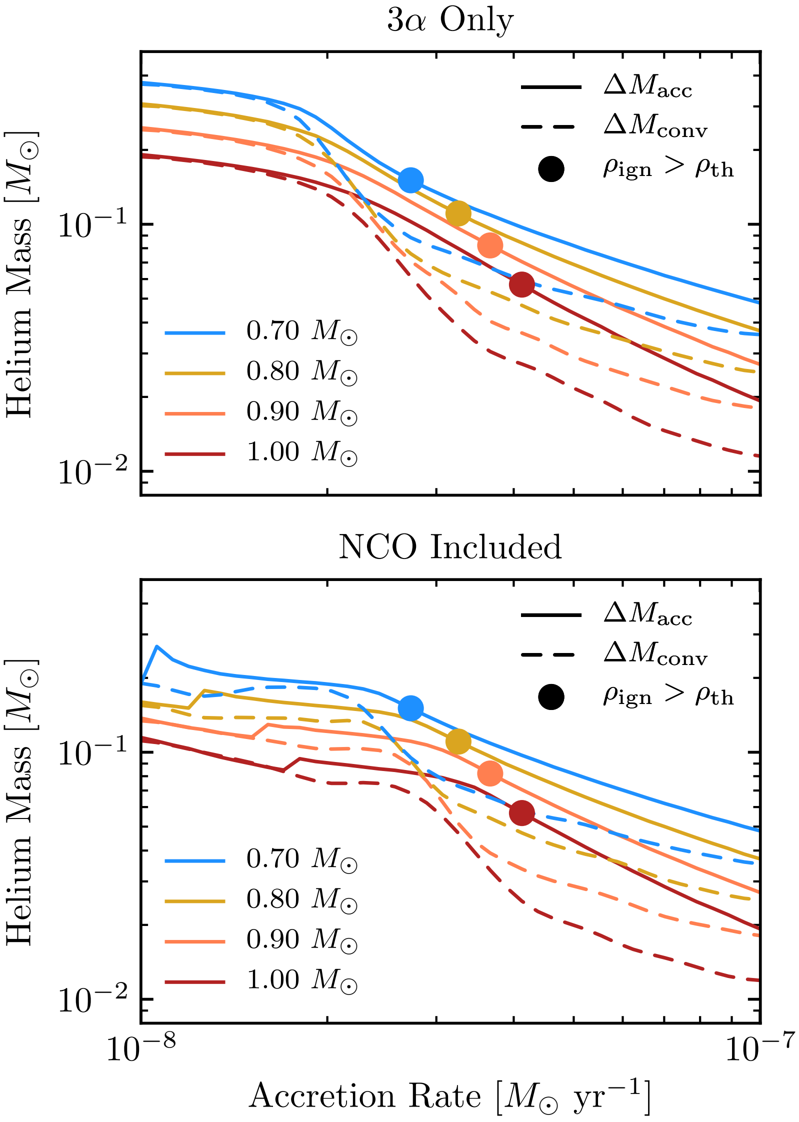

Figure 6.4: Accumulated helium shell masses and convective shell masses for flashes on various WD masses over a range of constant accretion rates. The upper panel shows flashes ignited by 3α alone, while the lower panel shows flashes when NCO reactions are included. Points indicate the first flash where the density at the base of the accreted material was above $\rho_{\rm th} = 1.25 \times 10^6 \, \mathrm{g \, cm^{-3}}$.

6.2.2 Constant $\dot{M}$ With NCO

A set of models similar to those shown in the top panel of Figure 6.4, but now including NCO reactions, is shown in the lower panel of Figure 6.4. For the region where density is beyond the threshold for NCO, we can see that the total accreted mass is somewhat lower due to earlier ignition, but in some cases the convective shell can still encompass more total mass due to the ignition occurring deeper in the accreted material.

The discontinuous feature in total accreted mass at low $\dot{M}$ in the lower panel of Figure 6.4 is due to failed NCO ignitions for certain accretion rates. The finite supply of ^{14}C at $X_{14} \approx 0.01$ can be exhausted before NCO burning can fully ignite a 3α runaway. Due to the highly degenerate conditions at the base of He envelopes that are dense enough for NCO to occur, electron conduction can carry significant amounts of heat inward toward the cooler core as $^{14}\mathrm{C}(\alpha,\gamma)^{18}\mathrm{O}$ begins to run away. This leads to a ΔT smaller than that predicted by equation (6.1). Figure 6.5 shows the envelope $\rho - T$ evolution of two models at very similar $\dot{M}$, where one experiences a failed NCO runaway at its base before eventually experiencing a true 3α runaway at the peak temperature location further out in the accreted He envelope.

The metallicity sets the total amount of ^{14}N available for NCO reactions. Since ΔT from complete NCO consumption scales with X_{14} in equation (6.1), variation in metallicity directly corresponds to variation in the total thermal impact that NCO reactions can have. Varying only the initial ^{14}N content in the grid of constant $\dot{M}$ models reveals a strong dependence on metallicity. These results are shown in Figure 6.6. For simplicity,

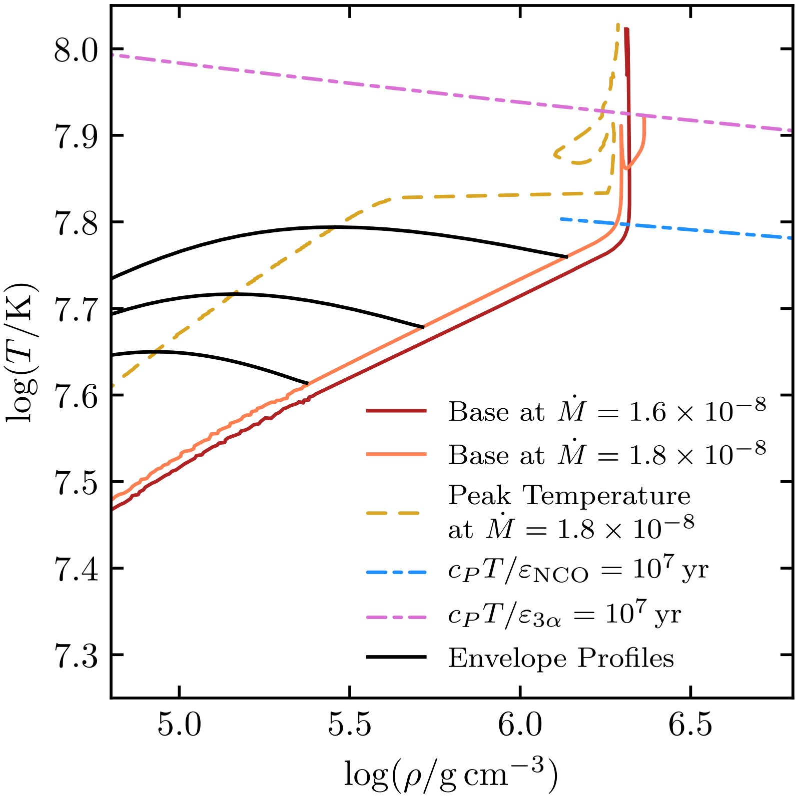

Figure 6.5: Density-temperature evolution of the accreted layer for a $1.0\,M_\odot$ WD accreting at two different rates. These two models correspond to the discontinuity in the red line in the lower panel of Figure 6.4.

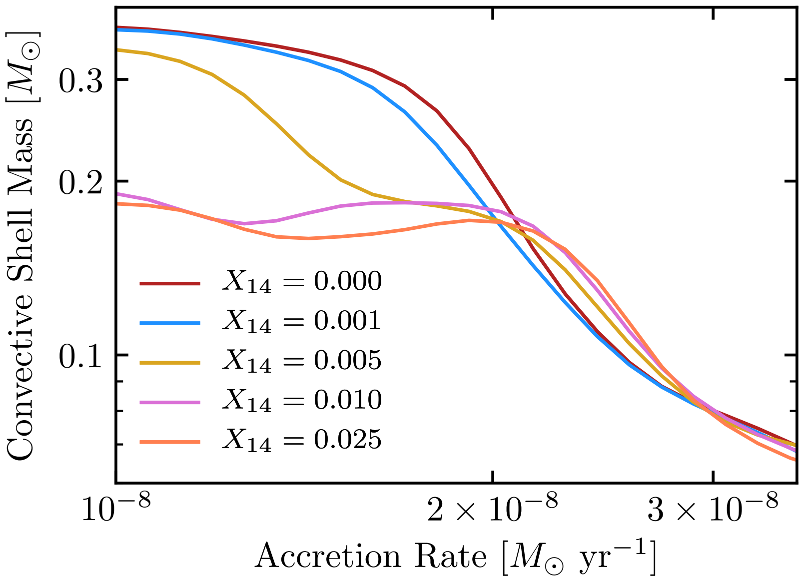

Figure 6.6: Convective shell masses at ignition as a function of constant accretion rate onto a $0.70\,M_\odot$ WD for varying metallicity. The lines shown here for $X_{14} = 0.000$ and $X_{14} = 0.010$ correspond to the dashed blue lines in Figure 6.4.

we only present the variation in runs for the $0.7\,M_\odot$ WD accretor model. Results for other accretor masses are similar. We assume that both the donor and accretor were born with the same metallicity, and that all CNO elements from the initial metallicity eventually end up as ^{14}N in both stars due to CNO burning in the evolution that produces them. Hence the initial mass fraction of ^{14}N in the He envelope of the WD is correlated with that in the He accreted from the donor. Since the initial He envelope ends up as the base of the He layer after accretion, it contributes to the energy produced in the dense layers where NCO reactions occur.

Larger convective shell masses are associated with denser ignition locations that may be expected to experience dynamical burning. This provides the potential for developing detonation fronts that can give rise to interesting phenomenology such as .Ia supernovae (Bildsten et al., 2007; Shen & Bildsten, 2009) or double detonation type Ia supernovae (Woosley & Weaver, 1994) if the detonation can transition into the C/O core. The threshold envelope mass for dynamical burning is on the order of $\sim 0.1\,M_\odot$. Because the NCO chain increases the convective shell mass in some regions, and the lower accretion rate regime is associated with large total accumulation masses, we see that NCO reactions are important for systems that have the potential to ignite dynamically.

Realistic binary systems often have accretion rates that vary across the boundary for high-density ignition shown by solid dots in Figure 6.4. Furthermore, Figure 6.4 shows that small variations in accretion rate around $2-4\times10^{-8}\,M_\odot\,\mathrm{yr}^{-1}$ can significantly impact the final convective shell mass, determining the dynamical fate of ignition. Clearly the constant $\dot{M}$ approximation is a concern, so we now use the robust binary capabilities present in `MESA` to test a range of realistic parameters and scenarios for NCO ignitions.

6.3 Realistic Mass Transfer Scenarios

We now show that NCO burning plays a significant role in the initial flash encountered in He star or sdB donor systems when the WD builds up a large He envelope. Our results at constant $\dot{M}$ in Section 6.2.2 suggest that the main impact of NCO reactions is to decrease both total accreted mass and convective envelope mass at low $\dot{M}$. However, our simulations of realistic binary evolution scenarios indicate that NCO burning can be much more significant than the constant $\dot{M}$ results suggest. Neunteufel et al. (2016) studied systems like these using detailed binary evolution and accretion rates while drawing on Woosley & Kasen (2011) for ignition outcomes of WDs treated as point mass accretors. However, our results indicate that the constant $\dot{M}$ results have limited predictive power in binary systems. Both the system and the WD must be evolved.

6.3.1 The First Flash after Contact

Brooks et al. (2015) used `MESA`'s binary evolution capabilities to model AM CVn systems, including realistic accretion histories for systems that are brought into contact by gravitational wave radiation, with self-consistent binary stellar evolution tracked through the accretion phase. Their study included many cycles of accretion, ignition, and flashes, but NCO reactions were not included. For many of the flashes, they found accumulated masses that were insufficient for the He layer to reach densities required for NCO reactions. A few of the flashes, however, did accumulate sufficient mass, particularly those occuring after the system first comes into contact and has not yet been warmed by previous flash episodes. In this section, we re-examine two of these binary scenarios where NCO reactions can play a role. The first is a $0.4\,M_\odot$ He star donating onto a $0.8\,M_\odot$ WD, and the second is the same donor model with a $1.0\,M_\odot$ WD accretor. These correspond to panels 2 and 4 in figures 12 and 13 from Brooks et al. (2015).

The accretion rate is primarily governed by the physics of the donor star, and our study here leaves this unmodified, so we use the same $\dot{M}$ histories as presented in figure 12 of Brooks et al. (2015) up to the point of ignition. With an identical starting model for

Table 6.1: Accreted and convective masses for the first helium flash

Accreted Mass ($\Delta M_{\rm acc}$)	Without NCO	With NCO
$0.4\,M_\odot$ He + $0.8\,M_\odot$ WD	$0.107\,M_\odot$	$0.107\,M_\odot$
$0.4\,M_\odot$ He + $1.0\,M_\odot$ WD	$0.082\,M_\odot$	$0.078\,M_\odot$
CD $-30°11223$	$0.175\,M_\odot$	$0.163\,M_\odot$
Convective Mass ($\Delta M_{\rm conv}$)	**Without NCO**	**With NCO**
$0.4\,M_\odot$ He + $0.8\,M_\odot$ WD	$0.055\,M_\odot$	$0.064\,M_\odot$
$0.4\,M_\odot$ He + $1.0\,M_\odot$ WD	$0.039\,M_\odot$	$0.054\,M_\odot$
CD $-30°11223$	$0.084\,M_\odot$	$0.153\,M_\odot$

the WD accretor and the accretion rate as specified by previous `MESA` binary runs, it is sufficient to follow the single star evolution in `MESA` for the accretor, with no further need to invoke `MESA` binary.

Figure 6.7 and Table 6.1 show that NCO reactions can modify the thermal structure prior to ignition, and more importantly, lead to ignition in the much deeper layers near the base of the accreted He. This effect is more pronounced for some systems than others, and the accretion rate from binary evolution plays a large role in determining the thermal structure of the accreting WD, which governs the impact of NCO reactions. The accretion rate varies from $2-4\times10^{-8}\,M_\odot\,{\rm yr}^{-1}$ over the course of accumulation leading to the first flash (see e.g. figures 11 and 12 in Brooks et al., 2015). Since this $\dot{M}$ range is precisely where Figure 6.4 shows the most significant variation in convective shell mass, there appears to be no reliable way to estimate the impact of NCO on ignition based on results at constant $\dot{M}$. Thus, accretion histories from full, self-consistent binary evolution such as those provided here need to be used to assess the condition at the time of thermal runaway.

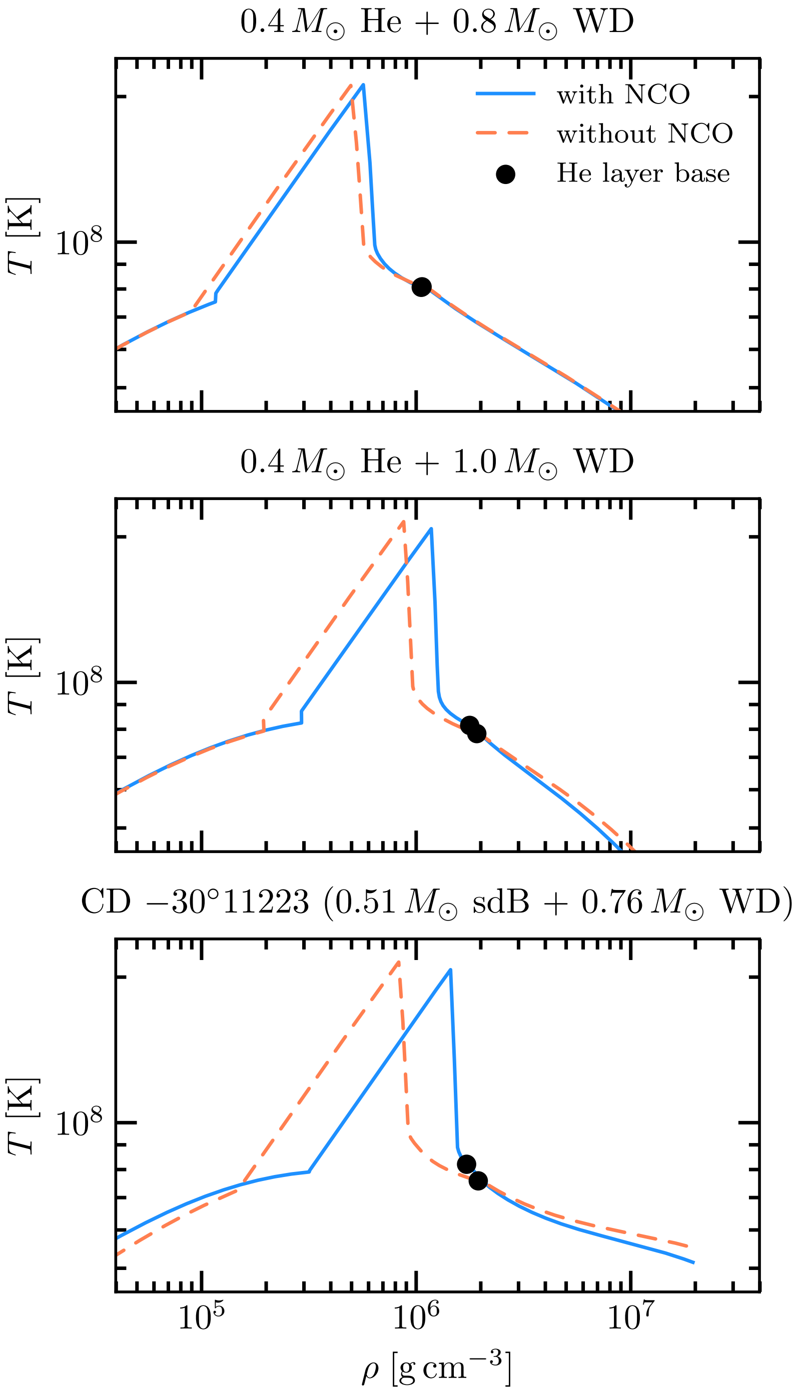

Figure 6.7: Profiles from models of the accreting WD in several binary systems after the flash has ignited. Models that include NCO reactions ignite in the deeper, denser region. In the case of CD −30°11223, the outer envelope has been noticeably warmed by additional heat from NCO burning prior to thermonuclear runaway.

6.3.2 The First Flash in CD $-30°11223$

CD $-30°11223$ (Geier et al., 2013) is a sdB+WD binary system with an orbital period of 70.5 minutes that will make contact in 40 Myr, likely while the sdB star's core is still burning He. Brooks et al. (2015) used `MESA` to model the binary evolution of this system as a $0.510\,M_\odot$ sdB star donating onto a $0.762\,M_\odot$ WD, with initial conditions tuned to match the observations of Geier et al. (2013) assuming that the sdB star is just beginning helium core burning. They predicted that the WD would accumulate a large He envelope ($\Delta M_{\rm acc} \approx 0.175\,M_\odot$) which will then experience 3α ignition above the base of envelope, leading to a smaller convective envelope ($\Delta M_{\rm conv} \approx 0.084\,M_\odot$). For more information on the details of the modeling of this binary system, see section 3.2 in Brooks et al. (2015). Using the same accretion history and starting model, we modeled the evolution of the accreting WD both with and without NCO reactions. If we do not include the reactions necessary for the NCO chain in our network, our results match those described by Brooks et al. (2015). In contrast, with NCO burning included in the network, the extra heat injected in the deeper, denser layers of the envelope leads to an earlier ignition of a slightly smaller ($\Delta M_{\rm acc} = 0.163\,M_\odot$) He envelope triggered by ^{14}C. However, since the ignition is triggered much deeper in the accreted envelope, as seen in Figure 6.7, this results in a much larger, and more dynamically important, convective envelope of mass $\Delta M_{\rm conv} = 0.153\,M_\odot$.

This near doubling of the convective shell mass has no parallel from the results at constant $\dot{M}$ shown in Section 6.2.2. In fact the trend seen there is in the opposite

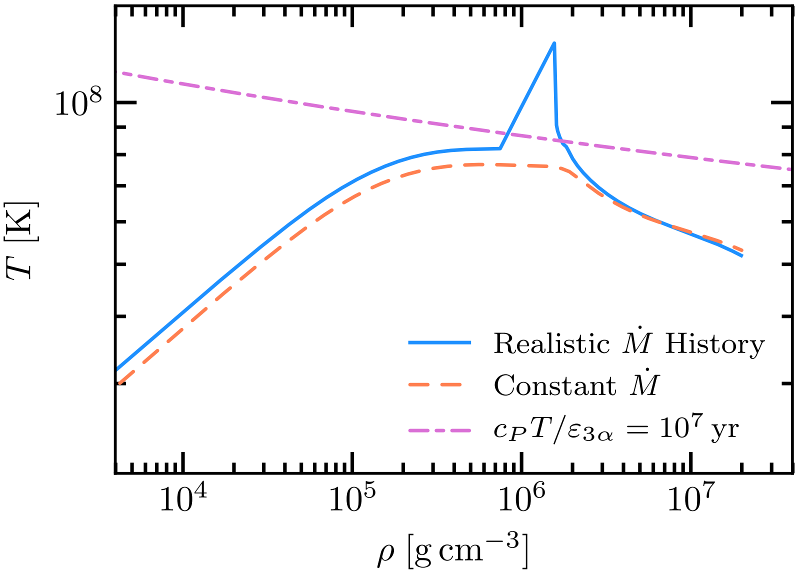

Figure 6.8: Effect of varying accretion history for CD $-30°11223$. The solid density-temperature profile shows the model evolved with a realistic accretion history from binary evolution. The dashed profile shows a model with a constant $\dot{M}$, corresponding to the time-average of the realistic history. The profiles are shown when the models reach a total mass of $M = 0.925\,\mathrm{M}_\odot$.

direction, where Figure 6.4 shows that NCO ignitions mostly tend to suppress the size of the convective shell by causing an earlier ignition while less total helium has had a chance to accumulate. This qualitatively different result of a much larger convective shell further motivates the use of full binary calculations in `MESA` to avoid the approximation of constant $\dot{M}$.

Figure 6.8 shows the contrast between modeling of CD $-30°11223$ including realistic accretion histories and modeling that makes the approximation of constant $\dot{M}$. The latter case assumes $\dot{M} = 1.93 \times 10^{-8}\,M_\odot\,\mathrm{yr}^{-1}$, the time-average of the accretion rate from the binary evolution calculations of Brooks et al. (2015). Both models here include the NCO reaction chain. After accumulating the same amount of mass to reach $M = 0.925\,M_\odot$, the model with constant $\dot{M}$ has not yet reached 3α ignition, while the realistic $\dot{M}$ model has. Indeed, the constant $\dot{M}$ model must accumulate 3% more mass before reaching ignition at a final mass of $M = 0.930\,M_\odot$.

6.3.3 Metallicity and ^{14}N Abundance in sdB Donors

For sdB star donors, the interior abundance of ^{14}N may be somewhat lower due to burning during the helium core flash having processed some of the ^{14}N to ^{18}O and ^{22}Ne. `MESA` models of the helium core flash show about half of the ^{14}N in the interior of the He core will be consumed, leaving behind $X_{14} \approx 0.005$ of the original $X_{14} \approx 0.01$ for resulting sdB models (at solar metallicity). The abundance remains $X_{14} \approx 0.01$ only in the unprocessed outer $\sim 0.01\,M_\odot$; see Figure 2.4. This means that after the first $0.01\,M_\odot$ of material donated, the abundance of ^{14}N in the donated material will drop to $X_{14} \approx 0.005$. However, NCO reactions are primarily significant in material from the initial He envelope of the accretor and first donated material, which will eventually form the most dense region of the He layer at its base. As Table 6.1 shows, these NCO reactions at the base of the He layer can provide sufficient heating to ignite the envelope within $\approx 0.01\,M_\odot$ of its base, so the lower abundance of ^{14}N in the accreted material further out should not significantly impact the outcome, and we ignore this change in abundance for all models presented in this work.

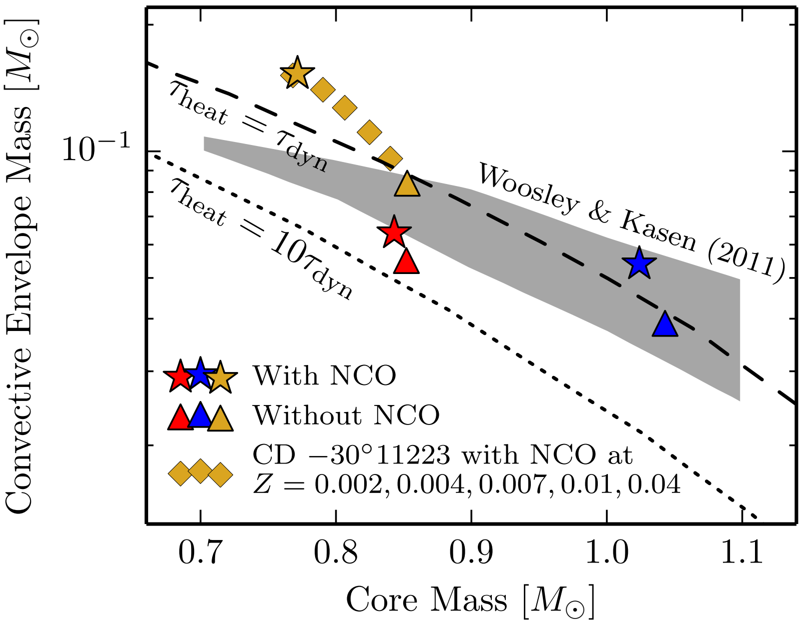

Figure 6.9: Masses from Table 6.1 showing that NCO burning pushes convective shells toward masses that will be more dynamical. Red points are for the $0.4\,M_\odot$ He + $0.8\,M_\odot$ WD system, and blue points are for the $0.4\,M_\odot$ He + $1.0\,M_\odot$ WD system. Gold points are for CD −30°11223, with diamonds used to show models with metallicity other than solar. The gray shaded region shows the minimum allowed envelope masses for detonation or deflagration found by Woosley & Kasen (2011) for a range of core temperatures. Note that core mass in this figure is defined as all of the mass inside the convective shell.

6.4 Dynamical Burning in Large Helium Envelopes

Following Bildsten et al. (2007), we study the possibility of dynamical burning that may transition into a detonation by plotting the convective shell masses from Table 6.1 along with lines comparing the dynamic timescale to the heating timescale from burning in Figure 6.9. These timescales are defined as $\tau_\mathrm{dyn} = H/c_\mathrm{sound}$ and $\tau_\mathrm{heat} = c_P T/\varepsilon_\mathrm{nuc}$, where $H = P/\rho g$, and ε_nuc is dominated by 3α burning that takes over once the thermonuclear runaway is initiated. These quantities are evaluated at the base of the convective burning shell. These lines are taken from figure 5 in Shen & Bildsten (2009). See also figure 7 in Brooks et al. (2015) for comparison, which has three points matching the three triangular symbols on our Figure 6.9, corresponding to binary models that did not include NCO reactions. For comparison, we also include the range of minimum allowed convective envelope masses for detonation or deflagration found by Woosley & Kasen (2011) in their extensive grid of constant $\dot{M}$ models.

The solar metallicity model for CD $-30°11223$ (gold star in Figure 6.9) is likely to reach especially dynamical burning conditions. At 0.1 s before the most rapid evolution occurs in the `MESA` model, $\tau_{\rm heat}$ becomes shorter than $\tau_{\rm dyn}$. If allowed to evolve beyond that point, peak burning reaches $\tau_{\rm heat} \approx 0.1\tau_{\rm dyn}$, and convective velocities reach nearly the sound speed. We expect that a detonation should develop around this point, but hydrostatic 1D `MESA` calculations are not reliable for evolution beyond this point. For more detailed study of the conditions of dynamical burning and convection leading to potential ignition of a detonation, see the recent work of Jacobs et al. (2016). The outcomes of their 3D hydrodynamical simulations appear to be broadly consistent with our expectations based on Figure 6.9, but further study is warranted.

The models for binary systems described in Sections 6.3.1 and 6.3.2 assumed solar metallicity for both the donor star and the WD progenitor, but the metallicity of CD $-30°11223$ is not known. Varying the metallicity of the system changes the amount of time necessary for the NCO chain to deposit enough heat to initiate a runaway, and hence the metallicity influences both total accreted mass and convective shell mass. This trend is clear in the diamond symbols showing convective shell masses in Figure 6.9, which represent the binary system described in Section 6.3.2 modeled with NCO reactions over a range of metallicities. For $Z \lesssim 0.02$, there is a continuous progression toward larger convective shell masses as metallicity increases for this system. However, once $Z \gtrsim 0.02$, there is plenty of ^{14}N present for the NCO chain to ignite runaway burning quickly after electron captures get underway past the threshold density, and hence higher metallicity does not significantly change the burning outcome past this point of saturation around solar metallicity.

6.5 Conclusions

Our results show that NCO reactions play an important role in triggering envelope ignitions for WDs accreting He at rates in the range $1 - 5 \times 10^{-8}\, M_\odot/\mathrm{yr}$. Binary systems composed of an sdB star donating He onto a WD naturally give rise to accretion rates that vary within this range. Because the thermal time is comparable to the accretion time in these He envelopes, it is necessary to model systems in a way that consistently tracks both the full accretion rate history and the evolution of the WD in response. Extrapolations from results using constant accretion rates are inadequate.

Though studies at constant $\dot{M}$ have concluded that NCO reactions provide only minor corrections with no qualitative differences, binary evolution with $\dot{M}$ that varies over the accumulation phase shows that NCO can be more important than previously thought. Models for the observed system CD $-30^\circ 11223$ illustrate the most pronounced qualitative differences that can arise as a result of NCO triggered ignitions during binary evolution, with a convective envelope mass that is twice as large in the case that includes NCO reactions. The recent discovery by Kupfer et al. (2017) of another system with a tight (87 min) sdB+WD binary demonstrates that detailed binary modeling with NCO reactions will continue to remain important as more of these systems are discovered.

The dynamical nature of the most extreme flashes presented here suggests that NCO triggered ignitions can lead to He detonations. We have also found that metallicity is directly correlated with the potential outcomes in these systems, with solar metallicity progenitors providing ample fuel for the NCO chain, while lower metallicities predictably soften its effects. Helium shell detonations are still possible in low metallicity environments without NCO triggers, but they appear less likely according to Figure 6.9. Though we have not exhaustively studied this trend, it may suggest a correlation between higher metallicity environments and observations involving events with thick helium shell detonations.

Future exploration should include modeling of additional variables that can impact the binary evolution of sdB+WD systems. Models presented here assumed that the sdB star in CD $-30^{\circ}11223$ is at the beginning of core He burning, but this age is not constrained. If the sdB star has a different He core burning age, the system will make contact at a different stage of the sdB life cycle, and the resulting accretion rate will vary accordingly. Since our results here show that the details of the accretion rate are crucial, variations in the $\dot{M}$ predicted by binary evolution may lead to different results for the total convective shell mass ignited on the WD. We anticipate a potential variation of predicted outcomes for the final fate of any given system where the sdB star age is not known.

More work is also necessary to strengthen our understanding of evolution beyond the onset of dynamical burning. Understanding the transition into detonation and the resulting effects on both the envelope and core will be crucial for making a specific prediction about the ultimate observable nature of these NCO triggered events.

Chapter 7

Conclusions and Future Work

Mixing timescales on the surfaces of white dwarf stars are the key theoretical ingredients needed to unlock the potential of observed systems for revealing properties of their surroundings. In this dissertation, I have shown how carefully quantifying these timescales enables inferring accretion rates that approach $\dot{M}_{\rm acc} \approx 10^{13}\,{\rm g\,s^{-1}}$, with rocky compositions similar to bulk earth material. Based on these accretion rates, inferences about populations of polluted white dwarfs imply that some white dwarfs have mass reservoirs of rocky material perhaps as large as an Earth mass. The work presented here has focused on white dwarfs with hydrogen-dominated atmospheres, but these are not the only sample of observed polluted white dwarfs. White dwarfs with helium-dominated atmospheres have longer mixing timescales, and their observations therefore probe a different regime of accretion timescales. Further work to resolve apparent discrepancies between systems with hydrogen and helium dominated atmospheres may yield deeper insight into the physical nature of the accretion processes that supply material onto white dwarf surfaces. The data point to a need for a more complete physical picture that can unify our understanding of these two observational classes, such as bursts of accretion that occur over a characteristic timescale yielding distinct observable signatures depending on the white dwarf surface mixing timescales.

Eliminating remaining theoretical uncertainties for polluted white dwarfs may require further work to constrain the physics of helium-dominated atmospheres. Opacities are difficult to calculate in the regime of cool, dense, neutral helium, and this makes it challenging to set appropriate surface boundary conditions in stellar models with such atmospheres. These boundary conditions have a large impact on the extent of surface convection zones. Opacities are further complicated by the introduction of even small amounts of polluting metals, and trace amounts of hydrogen can also cause modifications. The EOS for cool, partially ionized helium is uncertain as well, and this also has an impact on stellar modeling of convective boundaries. With further work to constrain these physical uncertainties, we may be able to produce a set of `MESA` models for white dwarfs with helium-dominated atmospheres to complement the hydrogen-dominated models presented here.

Convective overshoot is another area of uncertainty for model input physics. Our primary grid of models presented in Chapter 5 neglected overshoot. We demonstrated that overshoot has negligible effects in the regime where thermohaline mixing dominates near the white dwarf surface, but some cooler white dwarfs with lower accretion rates do not experience significant thermohaline instability, and therefore may require corrections due to overshoot. For now, the full extent of overshoot mixing beneath white dwarf surface convection zones is poorly understood, but simulations are expected to begin providing constraints on this extent soon. Once information is available to calibrate overshoot mixing regions in 1D simulations, it will be possible to produce a new generation of `MESA` models for polluted white dwarfs that fully accounts for convective overshoot along with diffusion, convection, and thermohaline mixing.

The tools for white dwarf surface mixing studied in this dissertation also have potential for application beyond the regime of planetary debris accretion. As shown in Chapter 6, a white dwarf accreting from a binary companion can experience a thermonuclear detonation. This can cause the accreting white dwarf to explode as a supernova, polluting its companion donor star with heavy elements from the ejecta. In the case where the donor star is initially a helium-burning sdB star as in Chapter 6, it can donate enough material that its central burning ceases. Liberated from the binary with a high orbital velocity at the time of explosion, the donor star will then cool as a low-mass white dwarf with a heavily polluted surface composition. Supernovae may also occur in binary systems where the donor star is initially a white dwarf. White dwarf remnants thought to originate from systems such as these have recently been identified (Shen et al., 2018; Raddi et al., 2018a,b, 2019), and theoretical modeling is needed to help understand the timescales over which observable ejecta pollution may remain at the surface. Models may help distinguish between potential stellar evolution channels that can produce high velocity objects with anomalous surface compositions.

Finally, models for white dwarf cooling are another natural next step based on the tools developed in this work. Though not a primary focus of this dissertation, the physics of white dwarf cooling appears in connection with many of the details discussed in Chapter 3 and Appendix B. With the extensive groundwork laid in those discussions, `MESA` is now in a position to offer grids of detailed white dwarf cooling tracks and isochrones with unprecedented resolution. These may be especially useful as a continuous extension of main sequence and giant branch `MESA` model grids that already exist (e.g. Dotter, 2016; Choi et al., 2016). Robust and flexible tools for white dwarf evolution within the open-source `MESA` framework will provide enhanced capacity to adapt and expand modeling as growing data sets present new challenges.

Appendix A

Diffusion Implementation Details

This appendix provides implementation details not contained in Chapter 3. Equations (3.2)–(3.4) and (3.9) give the full set of diffusion equations that must be solved to obtain diffusion velocities. For S total species in the plasma (including electrons), Equation (3.9) provides $S-1$ equations (one for each ion species), Equation (3.2) provides S equations (one for each species including electrons), and Equations (3.3) and (3.4) each provide one additional equation, for a total of $2S+1$ independent equations. The $2S+1$ unknowns are S diffusion velocities w_s, S heat flow vectors r_s, and the electric field E.

The inputs provided from the `MESA` model are the number densities n_s, temperature T, gradients of each of these quantities $\mathrm{d}\ln n_s/\mathrm{d}r$ and $\mathrm{d}\ln T/\mathrm{d}r$, species mass in atomic units A_s, species mean charge as an average ionization state $\bar{Z}_s$, and resistance coefficients K_{st}, z_{st}, z'_{st}, z''_{st} (defined in Equation 2.6). The coefficients are calculated as described in Section 3.3. Together with the mean ionization states, these are the key pieces of input physics that determine the diffusion of all ions. Extra acceleration terms $g_{\mathrm{rad},s}$ for radiative levitation are either set to zero by default, or calculated as in Hu et al. (2011) when the option to include radiative levitation is enabled.

In the spirit of Thoul et al. (1994), Equations (3.2)–(3.4) and (3.9) are grouped into a single matrix equation:

$$\beta_{\mathrm{rad},i} + \alpha_i m_{\mathrm{p}} g + \nu_i k_{\mathrm{B}} T \frac{\mathrm{d} \ln T}{\mathrm{d}r} + k_{\mathrm{B}} T \sum_j \gamma_{ij} \frac{\mathrm{d} \ln n_j}{\mathrm{d}r} = \sum_j \Delta_{ij} W_j. \tag{A.1}$$

The vectors capturing the driving terms are

$$\alpha_i = \begin{cases} n_i A_i & i = 1, \ldots, S-1, \\ 0 & i = S, \ldots, 2S+1, \end{cases} \tag{A.2}$$

$$\nu_i = \begin{cases} n_i & i = 1, \ldots, S-1, \\ \frac{5}{2} n_i & i = S, \ldots, 2S-1, \\ 0 & i = 2S, 2S+1, \end{cases} \tag{A.3}$$

$$\gamma_{ij} = \begin{cases} n_i \delta_{ij} & i = 1, \ldots, S-1, \\ 0 & i = S, \ldots, 2S+1, \end{cases} \tag{A.4}$$

$$\beta_{\mathrm{rad},i} = \begin{cases} -n_i A_i m_{\mathrm{p}} g_{\mathrm{rad},i} & i = 1, \ldots, S-1, \\ 0 & i = S, \ldots, 2S+1. \end{cases} \tag{A.5}$$

The vector containing the unknowns is

$$W_j = \begin{cases} w_j & j = 1, \ldots, S, \\ r_j & j = S+1, \ldots, 2S, \\ eE & j = 2S+1. \end{cases} \tag{A.6}$$

For $i = 1, \dots, S-1$, the right hand side matrix of Equation (A.1) is

$$\Delta_{ij} = \begin{cases} -\sum_{l \neq j} K_{il} & j = i, \\ K_{ij} & j = 1, \dots, S \text{ and } j \neq i, \\ \sum_{l \neq j} K_{il} z_{il} A_l / (A_i + A_l) & j = i + S, \\ -K_{i,j-S} z_{i,j-S} A_i / (A_i + A_{j-S}) & j = S+1, \dots, 2S \text{ and } j \neq i + S, \\ n_i \bar{Z}_i & j = 2S + 1. \end{cases} \tag{A.7}$$

For $i = S, \dots, 2S-1$, the matrix terms are

$$\Delta_{ij} = \begin{cases} \dfrac{5}{2} \displaystyle\sum_{l \neq j} K_{i-S,l} z_{i-S,l} \frac{A_l}{A_{i-S} + A_l} & j = i - S, \\ -\dfrac{5}{2} K_{i-S,j} z_{i-S,j} \dfrac{A_j}{A_{i-S} + A_j} & j = 1, \dots, S \text{ and } j \neq i - S, \\ \left. \begin{aligned} & -\sum_{l \neq j-S} K_{i-S,l} \Bigg[\frac{3A_{i-S}^2 + A_l^2 z'_{i-S,l}}{(A_{i-S} + A_l)^2} \\ & \qquad\qquad + \frac{4}{5} \frac{A_{i-S} A_l}{(A_{i-S} + A_l)^2} z''_{i-S,l} \Bigg] \\ & -\frac{2}{5} K_{i-S,i-S} z''_{i-S,i-S} \end{aligned} \right\} & j = i, \\ \left. \begin{aligned} & K_{i-S,j-S} \frac{A_{i-S} A_{j-S}}{(A_{i-S} + A_{j-S})^2} \\ & \qquad \times \left(3 + z'_{i-S,j-S} - \frac{4}{5} z''_{i-S,j-S} \right) \end{aligned} \right\} & j = S+1, \dots, 2S \text{ and } j \neq i, \\ 0 & j = 2S + 1. \end{cases} \tag{A.8}$$

For $i = 2S$,

$$\Delta_{ij} = \begin{cases} n_j A_j & j = 1, \dots, S, \\ 0 & j = S+1, \dots, 2S+1. \end{cases} \tag{A.9}$$

For $i = 2S + 1$,

$$\Delta_{ij} = \begin{cases} n_j \bar{Z}_j & j = 1, \dots, S, \\ 0 & j = S+1, \dots, 2S+1. \end{cases} \tag{A.10}$$

Indices $i = 1 \dots S-1$ capture the $S-1$ equations (3.9) for the ions. Indices $i = S \dots 2S-1$

capture the S equations (3.2). Indices $i = 2S, 2S+1$ capture the two constraints in Equations (3.3) and (3.4).

For a generic driving term that takes the form of an extra force f_s on ions of species s, a term $-n_s f_s$ appears on the left hand side of Equation (3.9). This can be accounted for in the matrix setup by adding another vector $\beta_{f,i}$ to the left hand side of Equation (A.1) with the form

$$\beta_{f,i} = \begin{cases} -n_i f_i & i = 1, \ldots, S-1, \\ 0 & S, \ldots, 2S+1. \end{cases} \tag{A.11}$$

One such extra driving force that may be explored with `MESA` in the future is Coulomb separation in dense matter arising from non-ideal corrections for the ions (Chang et al., 2010; Beznogov & Yakovlev, 2013; Diaw & Murillo, 2016).

The diffusion velocities are separated into two terms capturing the distinct effects of gravitational settling and ordinary diffusion in the tradition of Equation (11) of Iben & MacDonald (1985):

$$w_i = w_i^g - \sum_j \sigma_{ij} \frac{\mathrm{d} \ln C_j}{\mathrm{d}r}, \tag{A.12}$$

where $C_j \equiv n_j / n_\mathrm{e}$ following the notation of Thoul et al. (1994). These separate terms are constructed by inverting the matrix Δ_{ij} and then solving Equation (A.1) for just one of α, β, ν, and $\gamma_{*,j}$ at a time on the left hand side. These results can then be linearly combined to construct w_i^g and σ_{ij} such that the the full sum in Equation (A.12) gives a solution that satisfies the complete set represented by Equation (A.1).

When electrons become degenerate, we drop all S Equations (3.2) and set the S heat flow vectors to $r_s = 0$. Equation (A.1) then represents a system of just $S + 1$

equations and the vectors and matrices simplify considerably, dropping all entries for indices $i = S \ldots 2S - 1$ or $j = S + 1 \ldots 2S$ in the definitions given in Equations (A.2)–(A.10). To avoid discontinuities, we employ a blend that smoothly transitions between the diffusion velocity solutions over a range in $\eta \equiv \mu_{\mathrm{e}}/k_{\mathrm{B}}T$, where μ_{e} is the electron chemical potential. By default, the blend is centered around $\eta \approx 1$, with user controls available to adjust the range of this blending region.

Appendix B

Energy Accounting in Stellar Evolution

MESA I describes the stellar structure equations and their implementation in `MESA`. In order to provide physically and numerically accurate solutions of these equations, it is often necessary to evaluate them in different ways depending on the details of the star being simulated. In particular, there are a number of different ways to formulate and evaluate the equations solved by `MESA` that encode local and global energy conservation. The goal of this section is to clarify the available options, discuss when and why they are used, and describe how various forms of energy are tracked and accounted for in stellar evolution.

In Section B.1 we describe the fundamental equations we are solving, and in Section B.2 we describe choices associated with their numerical implementation. In Section B.3 we clarify how the energy associated with ionization is included in `MESA`. In Section B.4 we describe the numerical approach necessary to ensure that the latent heat associated with crystallization in a white dwarf (WD) is included in `MESA`. In Section B.5 we discuss the difficulties introduced by the necessity to blend between different equations of state (EOS) as the thermodynamic conditions in the stellar interior change, and how `MESA` minimizes artifacts associated with these blends. In Section B.6 we discuss the energy associated with gravitational settling.

B.1 Fundamental Equations

In the stellar structure equations (e.g., Cox & Giuli, 1968; Kippenhahn et al., 2012), energy conservation is typically formulated by considering the energy flow in and out of a fluid parcel. In this Lagrangian picture, to understand how the energy of a fluid parcel is changing, we account for the specific (i.e., per unit mass) rate of energy injection into the parcel, ϵ, and the specific rate of energy flow through the boundaries ($\partial L/\partial m$; $L(m)$ is the luminosity profile and m the Lagrangian mass coordinate). The specific heating rate ($\mathrm{D}q/\mathrm{D}t$) for the parcel must then satisfy

$$\frac{\mathrm{D}q}{\mathrm{D}t} = \epsilon - \frac{\partial L}{\partial m}, \tag{B.1}$$

where $\mathrm{D}/\mathrm{D}t$ is the Lagrangian time derivative. Except in the case of implicit hydrodynamics (where a total energy equation is solved; see MESA IV), the basic equation to be solved is always some form of Equation (B.1). By tradition, the negative of the left-hand side of Equation (B.1) is called ϵ_{grav}.

Thermodynamics relates the heating of material to the changes in its properties. The first law of thermodynamics states that the total heat added δQ for a parcel is

$$\delta Q \equiv \mathrm{d}E + P\mathrm{d}V, \tag{B.2}$$

where E is the internal energy, P is the pressure, and V is the volume. Let N_i be the number of particles of species i in the parcel. Then expanding E in terms of the independent thermodynamic basis variables (S, V, N_i) yields the following thermodynamic identity:

$$\mathrm{d}E + P\mathrm{d}V = T\mathrm{d}S + \sum_i \mu_i \mathrm{d}N_i \ , \tag{B.3}$$

where S is the entropy, and T is the temperature. The sum runs over all species present, and

$$\mu_i \equiv \left(\frac{\partial E}{\partial N_i}\right)_{S,V} \tag{B.4}$$

is the chemical potential for species i.

The number abundance of every species is defined with reference to the total number of baryons N_B as $Y_i \equiv N_i/N_\mathrm{B}$. Denoting Avogadro's number by N_A, the atomic mass unit is $m_\mathrm{amu} = 1\,\mathrm{g}/N_\mathrm{A}$. The specific (i.e., per unit mass) form of Equation (B.3) is then given by multiplying by the invariant $N_\mathrm{A}/N_\mathrm{B}$ to find

$$\delta q \equiv \mathrm{d}e + P\mathrm{d}\left(\frac{1}{\rho}\right) = T\mathrm{d}s + \sum_i \left(\frac{\partial e}{\partial Y_i}\right)_{s,\rho} \mathrm{d}Y_i \ . \tag{B.5}$$

The total baryonic mass density is ρ, so that $1/\rho$ is the specific volume, and e and s are specific energy and entropy respectively. Local thermodynamic equilibrium (LTE) determines a unique solution for the ionization state of each isotope. Thus, composition is completely specified by a set of number abundances $\{Y_i\}$ for all nuclear isotopes.

Equation (B.5) is relativistically correct when the rest mass is included in the energy and the chemical potentials. Therefore, in principle, changes in nuclear rest masses due to nuclear reactions could be accounted for via this equation. However, in `MESA`, the energetic effects associated with composition changes due to nuclear reactions are not included in $\epsilon_{\rm grav}$. Instead, these important terms are accounted for via $\epsilon_{\rm nuc}$ (the specific energy generation rate of nuclear reactions) which is evaluated separately and included as part of the local source term ϵ in Equation (B.1) (see MESA I).

It is often convenient to specify compositions in terms of the baryonic mass fractions $\{X_i\}$ via the relation $X_i = A_i Y_i$, where A_i is the mass number for isotope i. Since rest-mass changes due to nuclear reactions are handled separately from $\epsilon_{\rm grav}$, ρ and $\{X_i\}$ can be treated as independent basis variables without introducing any ambiguity into the chemical potential term in Equation (B.5). Some EOS options express the composition dependence in terms of aggregate quantities; examples include hydrogen abundance X, helium abundance Y, metallicity Z, average mass number $\bar{A}$, and average atomic number $\bar{Z}$.

The value for $\epsilon_{\rm grav}$ can be computed beginning from either the left or right hand side of the equals sign in Equation (B.5). Usually, some form of the left hand side is used, but in Section B.4 we will describe a case where it is more convenient to use the right hand side.

B.2 Implementation

Basic variables are those quantities directly calculated by `MESAstar`'s solver. Examples include velocity, radius, and the thermodynamic variables. `MESA` offers options for selecting $(\rho, T, \{X_i\})$ or $(P_{\rm gas}, T, \{X_i\})$ as the thermodynamic variables. The EOS routines calculate other thermodynamic quantities as a function of the chosen variables, e.g., $e = e(\rho, T, \{X_i\})$. `MESA` solves the stellar structure equations implicitly, thus it is possible to approximate total time derivatives of any quantity calculated in the stellar model simply by differencing its value at the start and end of a timestep. Therefore, one way to evaluate $\epsilon_{\rm grav}$ would be to directly calculate the time derivatives in Equation (B.5). Two possible versions of $\epsilon_{\rm grav}$ would then be

$$-\epsilon_{\rm grav} = T\frac{{\rm D}s}{{\rm D}t} + \sum_i \frac{\partial e}{\partial Y_i}\frac{{\rm D}Y_i}{{\rm D}t} \ , \tag{B.6}$$

and

$$-\epsilon_{\rm grav} = \frac{{\rm D}e}{{\rm D}t} + P\frac{\rm D}{{\rm D}t}\left(\frac{1}{\rho}\right) \ . \tag{B.7}$$

While simple to construct, the finite differences necessary to calculate these equations are often numerically problematic.

To see the potential numerical issues, consider the implementation of Equation (B.1) using Equation (B.7) in cell k with mass dm_k over a timestep δt. The derivative of a quantity ${\rm D}y/{\rm D}t$ is typically constructed as a finite difference of y over the timestep, so after integrating over the mass of zone k, we have

$$0 = \left(\epsilon_k - \frac{e_{k,\rm end} - e_{k,\rm start}}{\delta t} - P_k\frac{1/\rho_{k,\rm end} - 1/\rho_{k,\rm start}}{\delta t}\right) dm_k - (L_k - L_{k+1}) \ . \tag{B.8}$$

The implicit solver scheme in `MESA` attempts to reduce the residual from evaluating the right hand side of this equation below some tolerance.

While the implicit scheme in `MESA` may sometimes find acceptable results for an equation such as Equation (B.8), finite numerical precision can result in troublesome behavior for the time derivatives involving subtractions. In particular, over a small timestep where the change in e_k or ρ_k is small compared to the overall magnitude of these quantities, floating point arithmetic can suffer significant loss of precision. When energy scales arising from these types of finite difference derivatives are comparable to ϵ_k, the implicit solver may be unable to converge to an acceptable solution.

To avoid these problems, the equations can be cast in terms of derivatives that are not evaluated using subtractions. Such derivatives are available only for the basic variables, since the Jacobian matrix for an evolution step satisfying the equations of stellar structure in `MESA` is written in terms of the basic variables and their derivatives (see MESA I, Section 6.2 and MESA II, Section B.2 and Figure 47). For `MESA`, ρ and T serve as default variables.

Modifying Equation (B.7) to take advantage of ρ as a basic variable yields

$$-\epsilon_{\rm grav} = \frac{{\rm D}e}{{\rm D}t} - \frac{P}{\rho}\frac{{\rm D}\ln\rho}{{\rm D}t} \ , \tag{B.9}$$

but the change in e is still evaluated using subtraction. Another related form, obtained by application of mass continuity, is

$$-\epsilon_{\rm grav} = \frac{{\rm D}e}{{\rm D}t} + P\frac{\partial}{\partial m}(v\mathcal{A}) \ , \tag{B.10}$$

where v is the cell velocity and $\mathcal{A}$ is the area of the cell face. This is the form used in the artificial viscosity based hydrodynamics options described in MESA III.

Expanding the total derivative of energy and thus eliminating the subtraction motivates the following alternative forms. Expanding e in terms of its dependence on the basic variables ρ and T and dropping the dependence on composition gives

$$-\epsilon_{\rm grav} = c_V T \frac{{\rm D}\ln T}{{\rm D}t} + \left[\rho\left(\frac{\partial e}{\partial\rho}\right)_T - \frac{P}{\rho}\right]\frac{{\rm D}\ln\rho}{{\rm D}t}\ , \tag{B.11}$$

where $c_V \equiv (\partial q/\partial T)_\rho = (\partial e/\partial T)_\rho$. One can also choose to expand e in terms of its dependence on P and T (dropping composition dependence) and then convert to a form given in terms of ρ instead of P to obtain

$$-\epsilon_{\rm grav} = c_P T\left[(1-\nabla_{\rm ad}\chi_T)\frac{{\rm D}\ln T}{{\rm D}t} - \nabla_{\rm ad}\chi_\rho\frac{{\rm D}\ln\rho}{{\rm D}t}\right]\ , \tag{B.12}$$

where $c_P \equiv (\partial q/\partial T)_P$ and $\nabla_{\rm ad} \equiv (\partial\ln T/\partial\ln P)_s$. The derivation for this expression in terms of P and T is given in Chapter 4 of Kippenhahn et al. (2012), from which it is straightforward to obtain Equation (B.12) using $\chi_T \equiv (\partial\ln P/\partial\ln T)_\rho$ and $\chi_\rho \equiv (\partial\ln P/\partial\ln\rho)_T$.

Since ρ and T are basic variables, the time derivatives appearing in Equations (B.11) or (B.12) involve no subtractions. Hence, solving Equation (B.1) with $\epsilon_{\rm grav}$ as defined by those two equations will not be susceptible to the same losses of numerical precision as other forms, at the cost of dropping the composition terms. Similarly, Equation (4.47) of Kippenhahn et al. (2012) will yield the same stability when P and T are used as basic variables. When $P_{\rm gas}$ and T are selected as basic variables, the identification

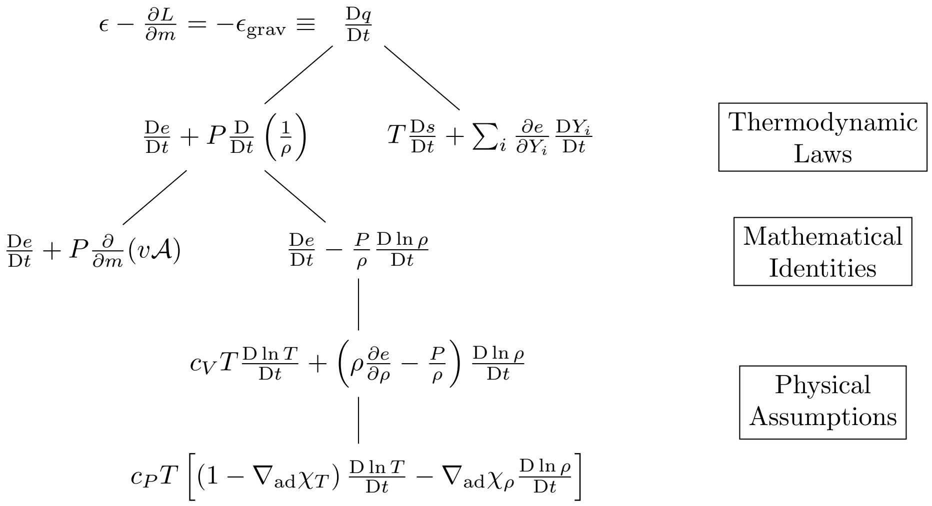

Figure B.1: Schematic showing the relationships in Equations (B.6)–(B.12).

$P = P_{\rm gas} + aT^4/3$ allows writing

$$-\epsilon_{\rm grav} = c_P T\left[\left(1 - 4\nabla_{\rm ad}\frac{P_{\rm rad}}{P}\right)\frac{{\rm D}\ln T}{{\rm D}t} - \nabla_{\rm ad}\frac{P_{\rm gas}}{P}\frac{{\rm D}\ln P_{\rm gas}}{{\rm D}t}\right]. \tag{B.13}$$

Section 4.5 in Kippenhahn et al. (2012) also shows how this local energy treatment of $\epsilon_{\rm grav}$ results in global energy conservation, including total gravitational potential energy from which the name $\epsilon_{\rm grav}$ is derived.

The superior numerical stability of Equations (B.11)–(B.13) comes at the cost of using derivative quantities such as c_V and χ_ρ. The Jacobian matrix of an implicit method thus requires the partial derivatives of c_V and χ_ρ. An EOS must therefore be capable of returning the state functions P, e, and s along with their first derivatives (e.g., c_V and χ_ρ) and second derivatives (e.g., $\partial c_V/\partial T$).

As noted above, Equations (B.11)–(B.13) drop the composition terms, which is justifiable if the derivatives $(\partial e/\partial X_i)({\rm D}X_i/{\rm D}t)$ are negligible for each X_i. Dropping com-

Table B.1: Summary of $\epsilon_{\rm grav}$ Options

Inlist Option	$\epsilon_{\rm grav}$
`use_PdVdt_form_for_eps_grav`	(B.7)
`use_dlnd_dt_form_for_eps_grav`	(B.9)
`use_dedt_form_of_energy_eqn`	(B.10)
`use_dEdRho_form_for_eps_grav`	(B.11)
`MESA` default (all other inlist options `.false.`)	(B.12)
`lnPgas_flag` (and other inlist options `.false.`)	(B.13)
`use_lnS_for_eps_grav`	(B.14)

position terms is often justified in stellar evolution scenarios where timescales for these changes are very slow or their associated energies are negligible, such as main-sequence (MS) burning where energy release from nuclear burning dominates any small changes in internal energy due to composition evolution over a single step (Kippenhahn et al., 1965; García-Berro et al., 2008). Making this assumption, `MESA` also offers an option for calculating $\epsilon_{\rm grav}$ in terms of a simplified form of Equation (B.6):

$$-\epsilon_{\rm grav} = T\frac{{\rm D}s}{{\rm D}t}\ , \tag{B.14}$$

which drops composition dependence to offer an expression that is more convenient to evaluate.

However, even after composition dependence related to nuclear burning is accounted for with a separate $\epsilon_{\rm nuc}$ term as discussed in Section B.1, other processes that change abundances (e.g., mixing) may be important. In cases where dropping these terms is not justifiable, it may be necessary to add a compensating local source term ϵ in Equation (B.1).

In summary, `MESA` currently offers options for solving Equation (B.1) with $\epsilon_{\rm grav}$ defined in any of the ways given in Equations (B.7)–(B.14). Figure B.1 schematically summarizes the relationships between these equations and Table B.1 shows the inlist commands necessary for invoking each of these options. Usually, the superior numerical stability gained by using Equation (B.12) is to be preferred, and hence it is the `MESA` default, but users should be aware of the possibility that other forms may be necessary to capture important physics. One such case for Equation (B.14) is described in Section B.4. Another is the artificial viscosity-based implicit hydrodynamics described in MESA III (see Section 4, Equation 41), where choosing Equation (B.10) helps ensure intrinsic energy conservation.

B.3 Ionization

The internal energy reported by the EOS should include the energy associated with ionization[1] and molecular dissociation. The assumption of LTE specifies the ionization state given $(\rho, T, \{X_i\})$. Since `MESA` does not regard a change in ionization as a change in composition, it is not necessary to include separate composition derivatives in $\epsilon_{\rm grav}$ in order to account for the energetic effects of changes in ionization state.

To demonstrate a specific scenario where `MESA` accounts for ionization energy, we evolve a $1\,{\rm M}_\odot$ pre-MS model composed of pure H. We compare quantities calculated by `MESA` with other, simpler estimates. We calculate the thermal energy assuming a

---

[1] Since this energy is released upon recombination, it is also often referred to as "recombination energy".

monatomic ideal gas,

$$e_{\text{thermal}} = \frac{3N_{\text{A}}k_{\text{B}}T}{2\mu} \ . \tag{B.15}$$

We calculate the ionization energy for pure H as

$$e_{\text{ion}} = (1 - f_{\text{H}})N_{\text{A}}E_{\text{H}} + \frac{N_{\text{A}}E_{\text{H2}}}{2} \ , \tag{B.16}$$

where we assume the ionization fraction of H is given by the Saha equation. The variable f_{H} represents the neutral fraction of H. The H ionization energy is $E_{\text{H}} = 13.6\,\text{eV}$ and Equation (B.16) also includes the dissociation energy of molecular H ($E_{\text{H2}} = 4.52\,\text{eV}$) assuming that no H is in the molecular state.

During the evolution, we record ϵ_{grav} calculated by `MESA` using Equation (B.12). We also evaluate the quantity

$$\underbrace{\frac{\mathrm{D}}{\mathrm{D}t}\left(e_{\text{thermal}}\right)}_{\epsilon_{\text{thermal}}} + \underbrace{\frac{\mathrm{D}}{\mathrm{D}t}\left(e_{\text{ion}}\right)}_{\epsilon_{\text{ion}}} + \underbrace{P\frac{\mathrm{D}}{\mathrm{D}t}\left(\frac{1}{\rho}\right)}_{\epsilon_{\text{PdV}}}$$

that separates out the thermal and ionization energy. In Figure B.2 we compare these two approaches, making it clear that all three terms in the above expression play an important role. Their sum agrees with the `MESA` ϵ_{grav}, indicating that each of these terms is accounted for in the `MESA` calculation.

Figure B.3 shows the history of the material at the Lagrangian coordinate $(M - m)/\text{M}_{\odot} = 10^{-5}$. We plot e reported by the `MESA` EOS along with e_{thermal} and e_{ion} (calculated in same manner as above). At this location, the specific internal energy is dominated by the ionization energy. The lower panel of this figure shows the neutral fraction of H; towards the left of the plot, the H is fully neutral. In this region the

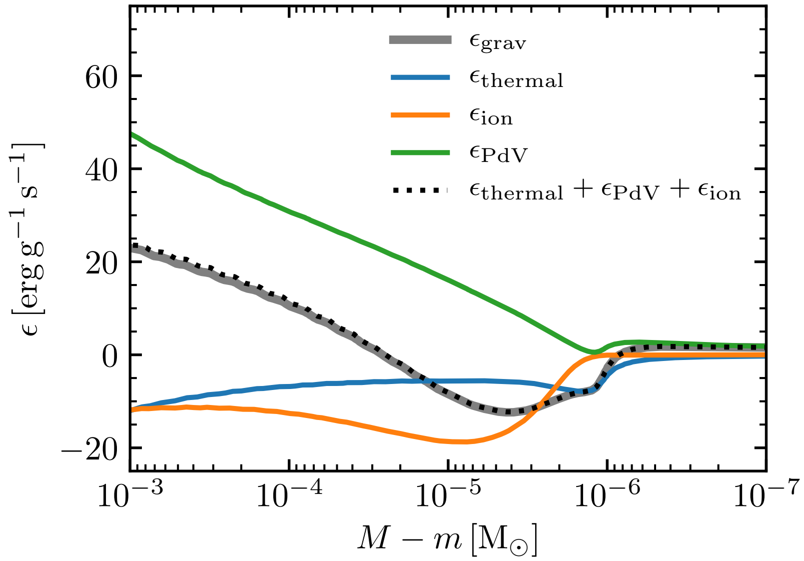

Figure B.2: The value of $\epsilon_{\rm grav}$ in the pure-H pre-MS model, evaluated over a region near the stellar surface that includes an ionization zone (where $\epsilon_{\rm ion} \neq 0$). The solid colored lines indicate the individual energy terms. Their sum (dotted black line) agrees with the value calculated by `MESA` (solid gray line).

ionization energy plateaus at the dissociation energy of molecular H (see Equation B.16).

For a star in hydrostatic equilibrium, the virial theorem states that

$$-\frac{1}{2}\int_0^M \frac{Gm}{r}dm + \int_0^M \frac{3P}{2\rho}dm = 0\ . \tag{B.17}$$

The right term's integrand, $3P/(2\rho)$, is the specific thermal energy of an ideal monatomic ideal gas. Figure B.4 shows the total internal energy and gravitational potential energy reported by `MESA` for the pure-H pre-MS model. On the same scale we show half the total potential energy plus the internal energy. This quantity is not zero; rather, by the virial theorem, it should sum to the non-thermal and non-ideal internal energy (e.g., the ionization energy). This value, recorded from the `MESA` model, agrees well with our

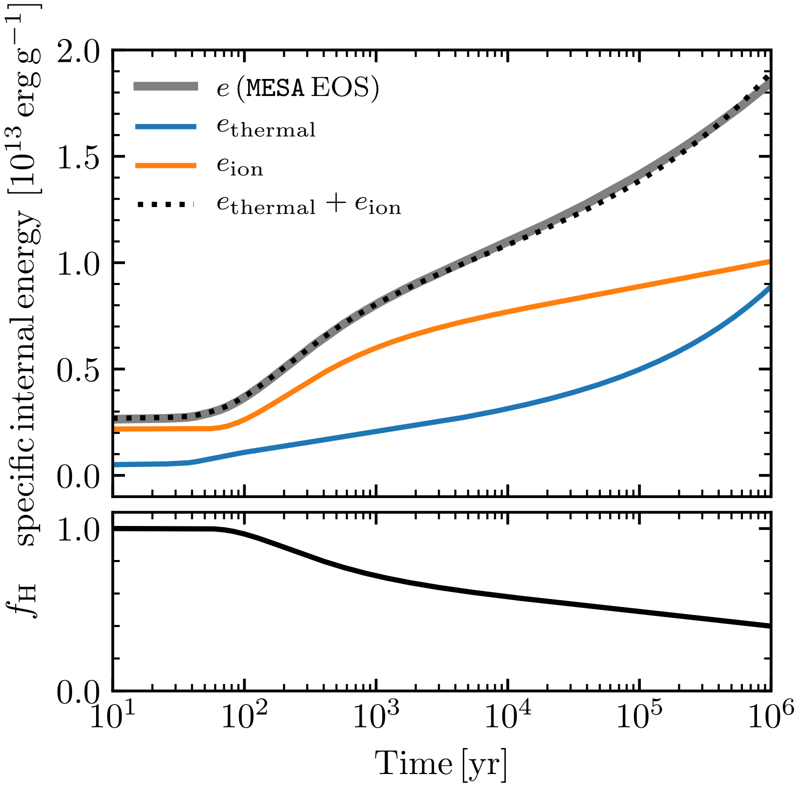

Figure B.3: Specific internal energy at a fixed Lagrangian coordinate in the pre-MS model (upper panel). The solid colored curves indicate the individual energy terms. The internal energy reported by `MESA` (solid gray curve) exceeds the thermal energy because of the ionization energy. The lower panel shows the neutral fraction of the H.

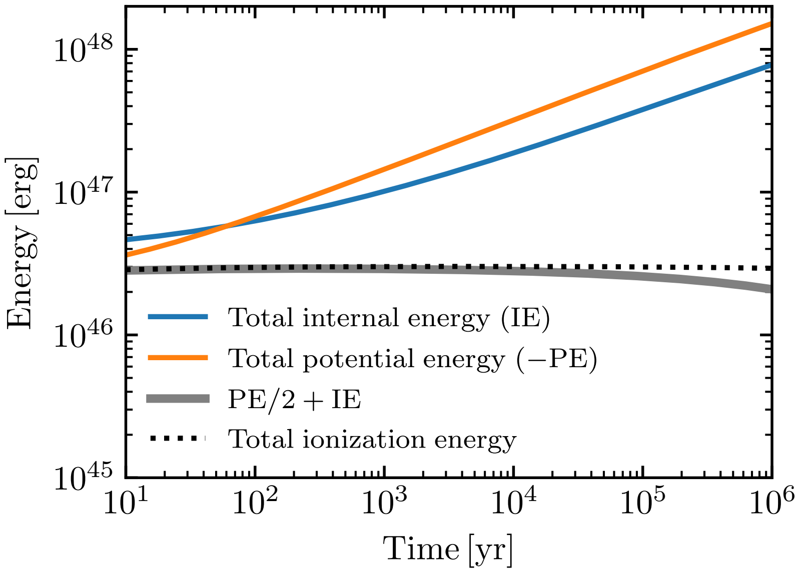

Figure B.4: Total potential and internal energy in the pure-H pre-MS model. The sum of half the total potential energy plus the internal energy (solid gray curve), which by the virial theorem should be the non-thermal internal energy, agrees well with our estimate of the ionization energy (dashed black curve). The deviation at $\gtrsim 10^5$ yr is caused by non-ideal gas effects.

estimate of the ionization energy. Also note that at early times the total energy of the star (internal + potential, not shown) is positive. The phenomenon of positive total energy when ionization energy is included also occurs for envelopes of stars on the asymptotic giant branch (AGB; Paczyński & Ziółkowski, 1968). Figure B.5 shows the total energy in the envelope of a $1.0\,\mathrm{M}_\odot$ `MESA` model on the AGB. This confirms that the ionization energy is included when `MESA` reports the total energy of a model.

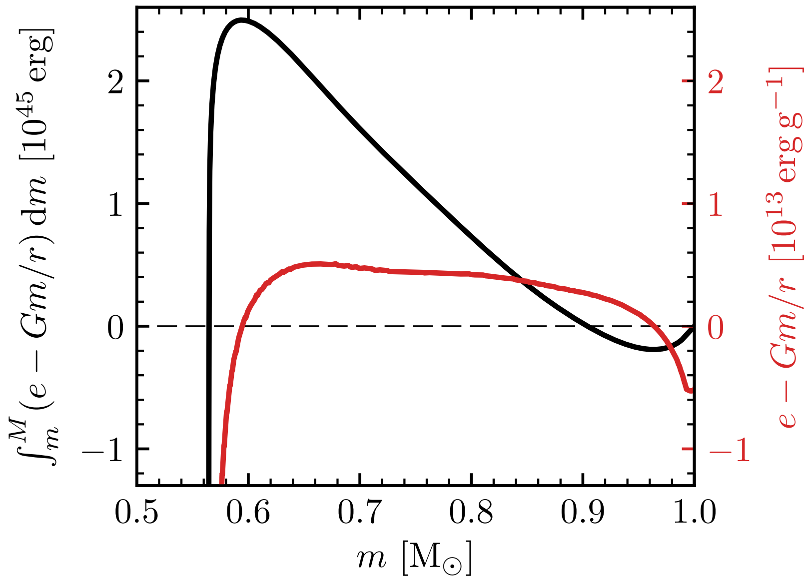

Figure B.5: Specific (red) and cumulative (black) total energy (IE + PE) in the envelope of an AGB model ($M = 1.0\,\mathrm{M}_\odot$, $L = 4.97 \times 10^3\,\mathrm{L}_\odot$, $T_{\rm eff} = 2,920\,\mathrm{K}$, $R = 276\,\mathrm{R}_\odot$). This energy is positive in the envelope due to the inclusion of ionization energy in the internal energy reported by `MESA`.

B.4 Latent Heat

MESA II discusses the inclusion of the latent heat of crystallization for long term WD cooling. Crystallization is a first-order phase transition that manifests in the PC EOS (Potekhin & Chabrier, 2010) as an entropy discontinuity at a plasma coupling parameter of $\Gamma = 175$, and can be captured in stellar evolution with $\epsilon_{\rm grav}$ in the form of Equation (B.14). Since the publication of MESA II, controls have been added to `MESA` to allow smoothing out the injection of latent heat in $\epsilon_{\rm grav}$ over a user-specified range of Γ. By default, the range for crystallization is softened to $150 \leq \Gamma \leq 175$ to avoid numerical difficulties with sudden energy injection associated with a sharp transition at $\Gamma = 175$. The controls allow for tightening this range for more precise timing on the occurrence

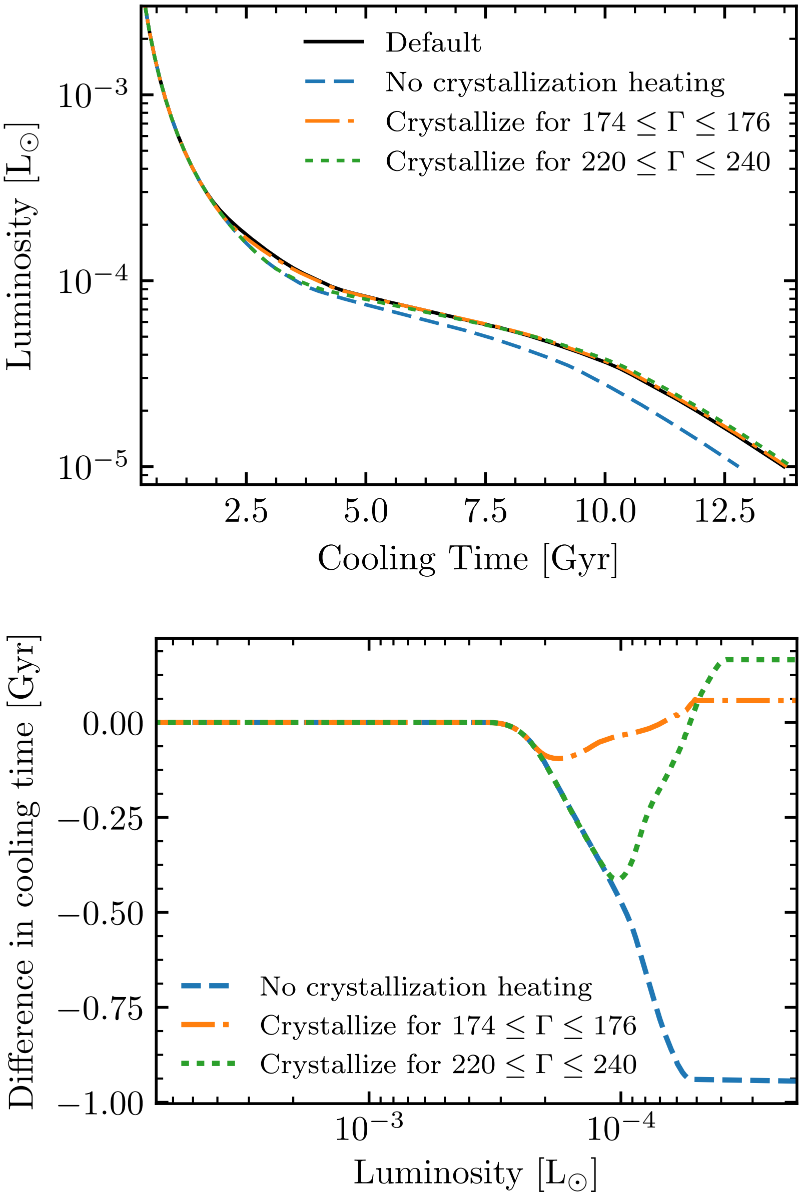

Figure B.6: Cooling for a $0.6\,\mathrm{M}_\odot$ C/O WD ($M_\mathrm{H} = 2.7 \times 10^{-5}\,\mathrm{M}_\odot$, $M_\mathrm{He} = 1.5 \times 10^{-2}\,\mathrm{M}_\odot$) with different treatments of the latent heat of crystallization. The default treatment smoothly injects the latent heat over the range $150 \leq \Gamma \leq 175$. The lower panel shows differences in cooling time (relative to the default shown in the upper panel) required to reach a given luminosity for other treatments.

of crystallization if necessary. Figure B.6 shows the small impact on cooling time for a $0.6\,\mathrm{M}_\odot$ WD from spreading the latent heat over this broader range of Γ relative to a tighter phase transition for $174 \leq \Gamma \leq 176$.

The spreading of the phase transition is accomplished by calculating both the liquid and solid solutions within the PC EOS and linearly blending the entropy s and internal energy e over the specified range of Γ. With ϵ_{grav} expressed in the form of Equation (B.14), the energy of the phase transition is captured as fluid elements smoothly traverse from liquid-phase to solid-phase. By default `MESA` automatically switches to using ϵ_{grav} in the form of Equation (B.14) for $\Gamma > 150$. This choice ensures the capture of latent heat release.

Theoretical and observational work has suggested that crystallization in C/O mixtures may occur at higher Γ than the classical one component plasma value of $\Gamma = 175$ (Horowitz et al., 2007; Winget et al., 2009; Medin & Cumming, 2010; Althaus et al., 2012). Our updated crystallization controls allow for investigating the effect on stellar evolution of crystallization at $\Gamma \approx 240$. Figure B.6 shows the potential effects on WD cooling times of varying the Γ for crystallization. Because the heating from crystallization is released very late in the WD evolution, its effects on cooling times are on the order of Gyr, and variations in crystallization treatment can lead to changes that are a significant fraction of this timescale.

The composition terms in Equation (B.6) that were dropped to form Equation (B.14) are negligible as long as there is no mixing in the crystallization region. Phase separation may violate this assumption and require a modified treatment, but we do not consider this process here. Detailed phase-diagrams for crystallization and the possible associated phase-separation effects are not currently supported in `MESA`, so our investigation here is limited to the effects of crystallization as a function of a fixed Γ range.

B.5 EOS Blending

As shown in Figure 1 of MESA I, `MESA` employs a patchwork of several EOSs to provide coverage of a maximal amount of $\rho - T$ space. When blending from one EOS region into another, care is required to avoid introducing spurious contributions into $\epsilon_{\rm grav}$. At high density, `MESA` blends from the Helmholtz EOS (HELM, Timmes & Swesty, 2000) for $\Gamma < 10$ to the PC EOS (Potekhin & Chabrier, 2010) for $\Gamma > 20$ by default. This default has been changed from the original default of $40 \leq \Gamma \leq 80$ given in MESA I due to the optimal agreement between relevant quantities shown in Figure B.8, as explained below. Overall, the two EOSs agree well on thermodynamic quantities in the blending region ($\sim 1\%$ for e and s), but Figure B.7 shows that the absolute magnitude of the disagreement can still be large enough to influence $\epsilon_{\rm grav}$ for a cooling WD when $\epsilon_{\rm grav}$ is expressed in the form of Equations (B.6)–(B.10).

The upper panel of Figure B.7 indicates that typically the internal energy difference is $\Delta e \sim 10^{15}\,{\rm erg\,g^{-1}}$, while $c_P T \sim 10^{14} - 10^{15}\,{\rm erg\,g^{-1}}$ in the region of the blend. As a WD model cools, most of its $\sim 10^{33}\,{\rm g}$ of mass must eventually pass through this transition. If the energy equation is being solved in the form of Equation (B.8), $\sim 10^{48}\,{\rm erg}$ of spurious

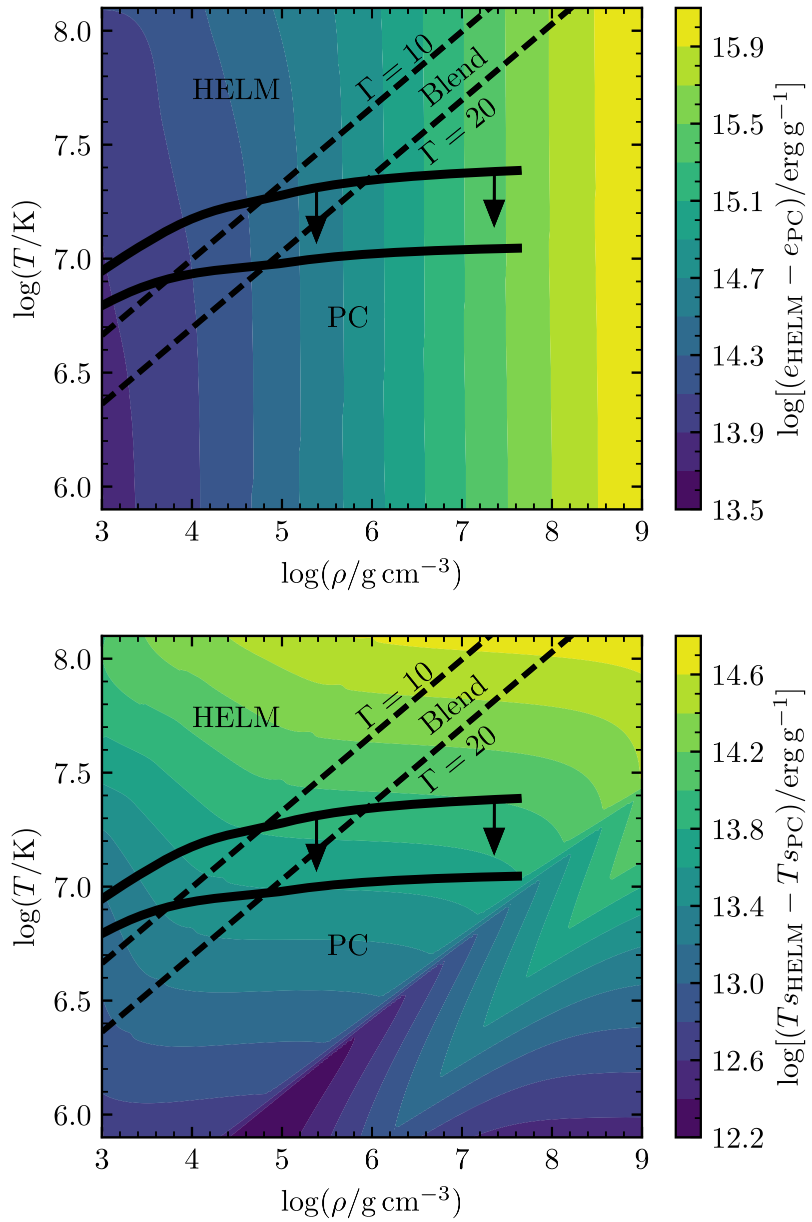

Figure B.7: Magnitude of the energy differences between the HELM and PC EOS for specific internal energy e (top) and entropy s (bottom) in a 50/50 C/O mixture. Dashed lines show the EOS blending boundaries for $10 \leq \Gamma \leq 20$, and the solid black lines show representative profiles for a $1.0\,\mathrm{M}_\odot$ WD cooling from $T_{\mathrm{eff}} = 26,000\,\mathrm{K}$ to $T_{\mathrm{eff}} = 17,000\,\mathrm{K}$.

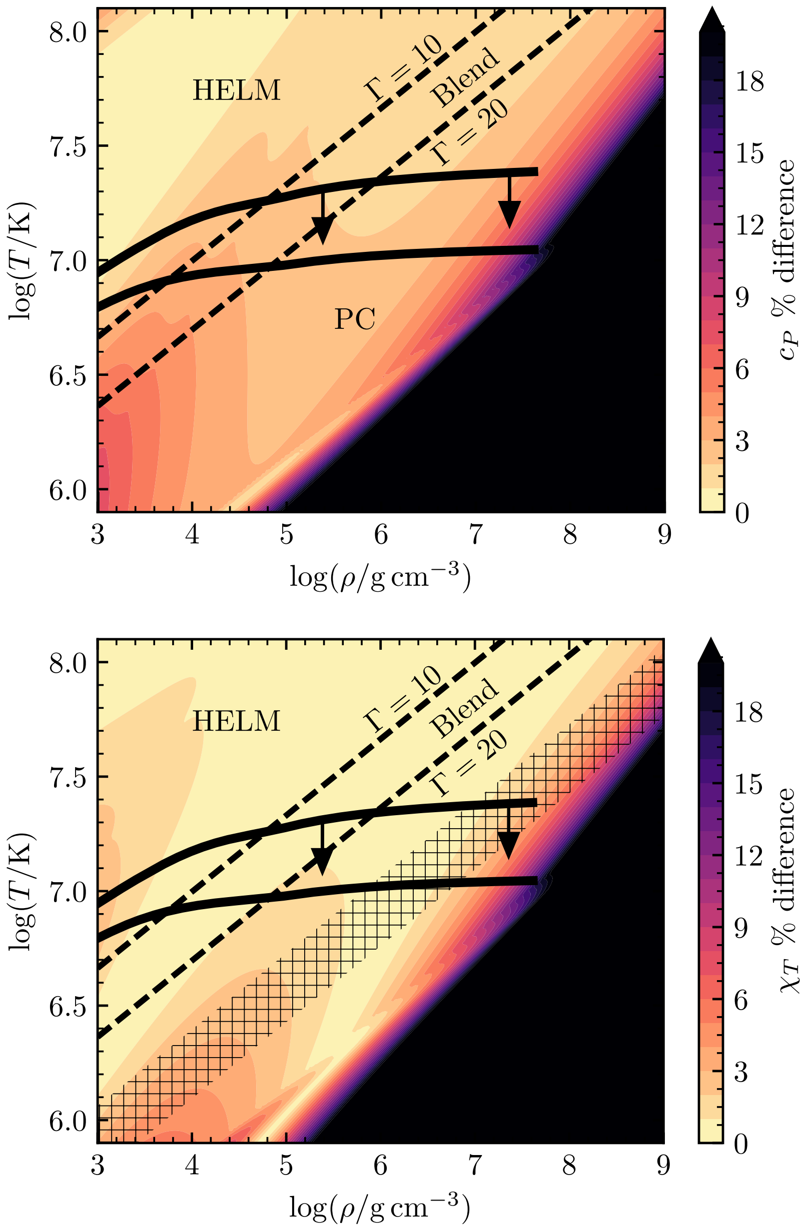

Figure B.8: Percent difference between HELM and PC EOS for c_P (top) and χ_T (bottom). Dashed lines show the EOS blending boundaries for $10 \le \Gamma \le 20$, and the hatched region in the lower panel shows the previous default blending range $40 \le \Gamma \le 80$. The new EOS blending region disagree by only a few percent for these quantities.

energy would be introduced into the model by EOS blending. Since much of this blending happens after the WD model has cooled to a luminosity of $L \lesssim 0.1\,\mathrm{L}_\odot$, this extra energy corresponds to $\Delta t \gtrsim 100\,\mathrm{Myr}$ of extra WD cooling time.

The default form of $\epsilon_{\rm grav}$ given in Equation (B.12) does not suffer from this spurious heating, since it is expressed in terms of thermodynamic derivatives from the EOS rather than e and s. For this form of $\epsilon_{\rm grav}$, the differences between e or s do not directly enter the equations. Instead, changes in e with $\mathrm{D}\ln\rho/\mathrm{D}t$ and $\mathrm{D}\ln T/\mathrm{D}t$ are tracked with quantities such as c_P and χ_T, and Figure B.8 shows that these agree well for the EOS blend region. Since the implementation of Equation (B.12) does not involve any derivatives constructed as finite differences, the fact that quantities such as c_P agree to within a few percent guarantees that $\epsilon_{\rm grav}$ will be consistent across the blend, with no significant spurious energy injected due to blending. Crucially, the release of latent heat described in Section B.4 requires switching to $\epsilon_{\rm grav}$ in the form of Equation (B.14) only for zones with $\Gamma > 150$, so both EOS blending and crystallization simultaneously receive appropriate treatments with different forms of $\epsilon_{\rm grav}$ in different stellar regions.

B.6 Gravitational Settling

Equation (B.12) for $\epsilon_{\rm grav}$ ignores changes in internal energy e due to composition changes. García-Berro et al. (2008) point out that a self-consistent evolutionary approach to WD cooling including the effects of ^{22}Ne settling requires accounting for composition changes due to element diffusion in $\epsilon_{\rm grav}$. They adopt pure ^{12}C or ^{16}O core compositions with trace ^{22}Ne and no other isotopes. While this approach is useful for rigorous study of self-consistent WD evolution with diffusion fully coupled to evolution, it is not well suited for a general treatment of realistic mixed core compositions.

`MESA` splits element diffusion into a separate step before the main structural solve, and hence diffusive effects are not included in $\epsilon_{\rm grav}$. We ensure that the energy associated with ^{22}Ne settling is not included in $\epsilon_{\rm grav}$ by using Equation (B.12), and we compensate by including an extra heating term ϵ_{22} in Equation (B.1). This term is calculated using velocities saved from the element diffusion step as described in Section 3.5. Our results for the effects of ^{22}Ne settling on WD cooling agree well with García-Berro et al. (2008) and with Deloye & Bildsten (2002) who adopt a heating term similar to our approach.

Appendix C

Diffusion Coefficients for Neutral Atoms

When diffusion occurs near the surface of a star, even a very small fraction of neutral particles for a given species can have a dramatic effect on the net diffusion flux for the element. The Coulomb collision formalism for diffusion coefficients no longer applies for neutral atoms, and induced dipole scattering of the neutral atoms with background ions becomes the relevant physical process for diffusion (Vennes et al., 2011a,b). `MESA` does not currently offer options for diffusion coefficients based on dipole scattering, but Chapter 2 describes much of the formalism necessary to construct them. Referring to Chapter 2, we see that the relevant coefficients for the Burgers (1969) diffusion equations are expressed in terms of

$$\Sigma_{st}^{(lj)} = \frac{4\pi}{\pi^{3/2}} \int_0^\infty dv \, \exp\left(\frac{-v^2}{\alpha_{st}^2}\right) \frac{v^{2j+3}}{\alpha_{st}^{2j+4}} S_{st}^{(l)} \ , \tag{C.1}$$

where $\alpha_{st} = 2k_BT/\mu_{st}$, $\mu_{st} = m_sm_t/(m_s + m_t)$ is the reduced mass of the scattering particles, and

$$S_{st}^{(l)} = 2\pi \int_0^\infty (1 - \cos^l \chi_{st}) b \, db \tag{C.2}$$

are the traditional scattering cross section integrals. The scattering angle χ_{st} is a function of both impact parameter b and relative velocity v, depending on the physics of the scattering process between particles s and t. For dipole scattering, Chapter 2 in Draine (2011) gives the scattering cross section of an ion with a polarizable neutral atom as

$$S_{st}^{(1)} = 2.41\pi Ze \left(\frac{\alpha_N}{\mu_{st}}\right)^{1/2} \frac{1}{v} \ , \tag{C.3}$$

where Z is the charge of the ion and α_N is the polarizability of the neutral atom. The result for $\Sigma_{st}^{(11)}$ is then

$$\Sigma_{st}^{(11)} = 3.62\pi \frac{Ze}{\alpha_{st}} \left(\frac{\alpha_N}{\mu_{st}}\right)^{1/2} \ . \tag{C.4}$$

Hence the result for the resistance coefficient for ions scattering with induced dipoles of neutral atoms is

$$K_{st} = \frac{2}{3} n_s n_t \mu_{st} \alpha_{st} \Sigma_{st}^{(11)} = 2.41\pi n_s n_t Ze \left(\mu_{st}\alpha_N\right)^{1/2} \ . \tag{C.5}$$

For comparison, the resistance coefficient given by Burgers (1969) for diffusion of ions with other ions is

$$K_{st} = \frac{16\sqrt{\pi}}{3} \frac{n_s n_t Z_s^2 Z_t^2 e^4}{\mu_{st}\alpha_{st}^3} \ln\Lambda \ , \tag{C.6}$$

where $\ln\Lambda$ is the Coulomb logarithm. Diffusion velocities scale inversely with the resistance coefficients K_{st}, so we can use these expressions to estimate the relative speeds of neutral and ionized metals.

Consider the case of a mixture of singly ionized oxygen and neutral oxygen diffusing in an ionized Hydrogen background. The above equations give that the ratio of the ion-neutral coefficient to the ion-ion coefficient is

$$\frac{K_{st}^{(\mathrm{dipole})}}{K_{st}^{(\mathrm{coulomb})}} = \frac{3.62(2k_BT)^{3/2}\left(\pi\alpha_N\right)^{1/2}}{8e^3\ln\Lambda} \ . \tag{C.7}$$

The polarizability of neutral oxygen is given in Table 2.1 of Draine (2011) as $\alpha_N = 5.326a_0^3$, where a_0 is the Bohr radius. For $T = 15,000\,\mathrm{K}$, we find that the resistance coefficient ratio is

$$\frac{K_{st}^{(\mathrm{dipole})}}{K_{st}^{(\mathrm{coulomb})}} = \frac{0.054}{\ln\Lambda} \ . \tag{C.8}$$

For conditions near the surface of a WD, we estimate the Coulomb logarithm as $\ln\Lambda \approx 5$ (Spitzer, 1962, Table 5.1). The final result for the ratio of coefficients is

$$\frac{K_{st}^{(\mathrm{dipole})}}{K_{st}^{(\mathrm{coulomb})}} \sim 10^{-2} \ . \tag{C.9}$$

This means that the neutral oxygen particles will have diffusion velocities approximately 100 times faster than the singly ionized particles. A mere 1% of particles being neutral for a particular element can therefore significantly modify the net diffusion flux for that element. This effect would be most noticeable for metals with relatively high first ionization potentials.

Since the physics of scattering is fundamentally different for charged and neutral particles, the diffusion and resistance coefficients do not scale in a meaningful way as $Z \to 0$. It is hence meaningless to adopt an average charge for an element for purposes of diffusion calculations in the case of $\bar{Z} < 1$. This is why the diffusion implementation in `MESA` currently assumes that all diffusing particles are at least singly ionized. Extending the implementation to account for neutral particles would require two improvements: a) the ability to separate neutral particles off as distinct diffusion classes, and b) incorporating tables of atomic polarizabilities to use with Equation (C.5) for the resistance coefficients to use in the Burgers equations.

Bibliography

Ajzenberg-Selove, F. 1991, Nuclear Physics A, 523, 1

Althaus, L. G., & Benvenuto, O. G. 2000, MNRAS, 317, 952

Althaus, L. G., García-Berro, E., Isern, J., Córsico, A. H., & Miller Bertolami, M. M. 2012, A&A, 537, A33

Althaus, L. G., Miller Bertolami, M. M., & Córsico, A. H. 2013, A&A, 557, A19

Althaus, L. G., Serenelli, A. M., & Benvenuto, O. G. 2001, MNRAS, 323, 471

Althaus, L. G., Serenelli, A. M., Córsico, A. H., & Montgomery, M. H. 2003, A&A, 404, 593

Arcoragi, J.-P., & Fontaine, G. 1980, ApJ, 242, 1208

Baalrud, S. D., & Daligault, J. 2013, PhRvL, 110, 235001

—. 2014, Physics of Plasmas, 21, 055707

Baines, P. G., & Gill, A. E. 1969, Journal of Fluid Mechanics, 37, 289

Bauer, E. B. 2019, Zenodo, evbauer/DA_Pollution_Tables, MESA Polluted WDs

Bauer, E. B., & Bildsten, L. 2018, ApJL, 859, L19

—. 2019, ApJ, 872, 96

Bauer, E. B., Schwab, J., & Bildsten, L. 2017, ApJ, 845, 97

Beznogov, M. V., & Yakovlev, D. G. 2013, PhRvL, 111, 161101

Beznogov, M. V., & Yakovlev, D. G. 2014, PhRvE, 90, 033102

Bildsten, L., & Hall, D. M. 2001, ApJL, 549, L219

Bildsten, L., Shen, K. J., Weinberg, N. N., & Nelemans, G. 2007, ApJL, 662, L95

Bohm, K. H., & Cassinelli, J. 1971, A&A, 12, 21

Brassard, P., & Fontaine, G. 2015, in Astronomical Society of the Pacific Conference Series, Vol. 493, 19th European Workshop on White Dwarfs, ed. P. Dufour, P. Bergeron, & G. Fontaine, 121

Brooks, J., Bildsten, L., Marchant, P., & Paxton, B. 2015, ApJ, 807, 74

Brown, J. M., Garaud, P., & Stellmach, S. 2013, ApJ, 768, 34

Buchler, J. R., & Yueh, W. R. 1976, ApJ, 210, 440

Burgers, J. M. 1969, Flow Equations for Composite Gases (Academic Press)

Camisassa, M. E., Althaus, L. G., Rohrmann, R. D., et al. 2017, ApJ, 839, 11

Cantiello, M., & Langer, N. 2010, A&A, 521, A9

Cassisi, S., Potekhin, A. Y., Pietrinferni, A., Catelan, M., & Salaris, M. 2007, ApJ, 661, 1094

Chang, P., Bildsten, L., & Arras, P. 2010, ApJ, 723, 719

Charbonnel, C., & Zahn, J.-P. 2007, A&A, 467, L15

Chayer, P. 2014, MNRAS, 437, L95

Chayer, P., Fontaine, G., & Wesemael, F. 1995a, ApJS, 99, 189

Chayer, P., Vennes, S., Pradhan, A. K., et al. 1995b, ApJ, 454, 429

Chen, D.-C., Zhou, J.-L., Xie, J.-W., et al. 2019, Nature Astronomy, 3, 69

Choi, J., Dotter, A., Conroy, C., et al. 2016, ApJ, 823, 102

Chugunov, A. I., Dewitt, H. E., & Yakovlev, D. G. 2007, PhRvD, 76, 025028

Córsico, A. H., Benvenuto, O. G., Althaus, L. G., & Serenelli, A. M. 2002, MNRAS, 332, 392

Cox, J. P., & Giuli, R. T. 1968, Principles of Stellar Structure (Gordon and Breach, New York)

Cyburt, R. H., Amthor, A. M., Ferguson, R., et al. 2010, ApJS, 189, 240

Daligault, J., Baalrud, S. D., Starrett, C. E., Saumon, D., & Sjostrom, T. 2016, PhRvL, 116, 075002

Daligault, J., & Murillo, M. S. 2005, PhRvE, 71, 036408

Deal, M., Deheuvels, S., Vauclair, G., Vauclair, S., & Wachlin, F. C. 2013, A&A, 557, L12

Debes, J. H., Walsh, K. J., & Stark, C. 2012, ApJ, 747, 148

Deloye, C. J., & Bildsten, L. 2002, ApJ, 580, 1077

Denissenkov, P. A., & Pinsonneault, M. 2008, ApJ, 684, 626

Diaw, A., & Murillo, M. S. 2016, ApJ, 829, 16

Dotter, A. 2016, ApJS, 222, 8

Draine, B. T. 2011, Physics of the Interstellar and Intergalactic Medium (Princeton University Press, Princeton, NJ)

Dufour, P., Kilic, M., Fontaine, G., et al. 2010, ApJ, 719, 803

—. 2012, ApJ, 749, 6

Dupuis, J., Fontaine, G., Pelletier, C., & Wesemael, F. 1992, ApJS, 82, 505

—. 1993, ApJS, 84, 73

Eggleton, P. P. 1983, ApJ, 268, 368

Farihi, J. 2016, NewAR, 71, 9

Farihi, J., Gänsicke, B. T., & Koester, D. 2013, Science, 342, 218

Farihi, J., Gänsicke, B. T., Wyatt, M. C., et al. 2012, MNRAS, 424, 464

Farihi, J., Jura, M., & Zuckerman, B. 2009, ApJ, 694, 805

Farihi, J., Fossati, L., Wheatley, P. J., et al. 2018, MNRAS, 474, 947

Ferguson, J. W., Alexander, D. R., Allard, F., et al. 2005, ApJ, 623, 585

Fontaine, G., Brassard, P., & Bergeron, P. 2001, PASP, 113, 409

Fontaine, G., & Michaud, G. 1979, in IAU Colloq. 53: White Dwarfs and Variable Degenerate Stars, ed. H. M. van Horn & V. Weidemann, 192

Freytag, B., Ludwig, H.-G., & Steffen, M. 1996, A&A, 313, 497

Fuller, G. M., Fowler, W. A., & Newman, M. J. 1980, ApJS, 42, 447

—. 1985, ApJ, 293, 1

Gänsicke, B. T., Koester, D., Farihi, J., et al. 2012, MNRAS, 424, 333

Garaud, P. 2018, Annual Review of Fluid Mechanics, 50, 275

García-Berro, E., Althaus, L. G., Córsico, A. H., & Isern, J. 2008, ApJ, 677, 473

García-Berro, E., Torres, S., Althaus, L. G., et al. 2010, Nature, 465, 194

Geier, S., Marsh, T. R., Wang, B., et al. 2013, A&A, 554, A54

Girven, J., Brinkworth, C. S., Farihi, J., et al. 2012, ApJ, 749, 154

Grad, H. 1949, Communications on Pure and Applied Mathematics, 2, 331

Graham, J. R., Matthews, K., Neugebauer, G., & Soifer, B. T. 1990, ApJ, 357, 216

Hansen, B. 2004, PhR, 399, 1

Hashimoto, M. A., Nomoto, K. I., Arai, K., & Kaminisi, K. 1986, ApJ, 307, 687

Hermes, J. J., Gänsicke, B. T., Kawaler, S. D., et al. 2017, ApJS, 232, 23

Hollands, M. A., Gänsicke, B. T., & Koester, D. 2018, MNRAS, 477, 93

Horowitz, C. J., Berry, D. K., & Brown, E. F. 2007, PhRvE, 75, 066101

Hu, H., Tout, C. A., Glebbeek, E., & Dupret, M.-A. 2011, MNRAS, 418, 195

Iben, I., Nomoto, K., Tornambe, A., & Tutukov, A. V. 1987, ApJ, 317, 717

Iben, Jr., I., Fujimoto, M. Y., & MacDonald, J. 1992, ApJ, 388, 521

Iben, Jr., I., & MacDonald, J. 1985, ApJ, 296, 540

Iglesias, C. A., & Rogers, F. J. 1993, ApJ, 412, 752

—. 1996, ApJ, 464, 943

Iliadis, C., Longland, R., Champagne, A. E., Coc, A., & Fitzgerald, R. 2010, Nuclear Physics A, 841, 31

Istrate, A. G., Fontaine, G., Gianninas, A., et al. 2016a, A&A, 595, L12

Istrate, A. G., Marchant, P., Tauris, T. M., et al. 2016b, A&A, 595, A35

Itoh, N., Hayashi, H., Nishikawa, A., & Kohyama, Y. 1996, ApJS, 102, 411

Jacobs, A. M., Zingale, M., Nonaka, A., Almgren, A. S., & Bell, J. B. 2016, ApJ, 827, 84

Johnson, E. D., Rogachev, G. V., Mitchell, J., Miller, L., & Kemper, K. W. 2009, PhRvC, 80, 045805

Jones, S., Andrassy, R., Sandalski, S., et al. 2017, MNRAS, 465, 2991

Jura, M. 2003, ApJL, 584, L91

Jura, M., & Young, E. D. 2014, Annual Review of Earth and Planetary Sciences, 42, 45

Kenyon, S. J., & Bromley, B. C. 2017a, ApJ, 844, 116

—. 2017b, ApJ, 850, 50

Kippenhahn, R., Ruschenplatt, G., & Thomas, H.-C. 1980, A&A, 91, 175

Kippenhahn, R., Thomas, H. C., & Weigert, A. 1965, ZA, 61, 241

Kippenhahn, R., Weigert, A., & Weiss, A. 2012, Stellar Structure and Evolution, Astronomy and Astrophysics Library (Berlin, Heidelberg: Springer-Verlag)

Koester, D. 2009, A&A, 498, 517

—. 2010, MmSAI, 81, 921

Koester, D. 2015, in Astronomical Society of the Pacific Conference Series, Vol. 493, 19th European Workshop on White Dwarfs, ed. P. Dufour, P. Bergeron, & G. Fontaine, 129

Koester, D., Gänsicke, B. T., & Farihi, J. 2014, A&A, 566, A34

Koester, D., Girven, J., Gänsicke, B. T., & Dufour, P. 2011, A&A, 530, A114

Koester, D., Provencal, J., & Shipman, H. L. 1997, A&A, 320, L57

Koester, D., & Wilken, D. 2006, A&A, 453, 1051

Korre, L., Garaud, P., & Brummell, N. H. 2019, MNRAS, 484, 1220

Kupfer, T., van Roestel, J., Brooks, J., et al. 2017, ApJ, 835, 131

Kupka, F., Zaussinger, F., & Montgomery, M. H. 2018, MNRAS, 474, 4660

Langanke, K., & Martínez-Pinedo, G. 2000, Nuclear Physics A, 673, 481

Lecoanet, D., Schwab, J., Quataert, E., et al. 2016, ApJ, 832, 71

Liebert, J. 1980, ARA&A, 18, 363

Martínez-Rodríguez, H., Piro, A. L., Schwab, J., & Badenes, C. 2016, ApJ, 825, 57

McDonough, W. F. 2001, in EarthQuake Thermodynamics and Phase Transformations in the Earth's Interior, ed. E. R. Teisseyre & E. Majewski (San Diego: Academic Press), 3

Medin, Z., & Cumming, A. 2010, PhRvE, 81, 036107

Metzger, B. D., Rafikov, R. R., & Bochkarev, K. V. 2012, MNRAS, 423, 505

Montgomery, M. H., & Kupka, F. 2004, MNRAS, 350, 267

Mustill, A. J., Villaver, E., Veras, D., Gänsicke, B. T., & Bonsor, A. 2018, MNRAS, 476, 3939

Nelemans, G., Yungelson, L. R., & Portegies Zwart, S. F. 2004, MNRAS, 349, 181

Neunteufel, P., Yoon, S.-C., & Langer, N. 2016, A&A, 589, A43

Noerdlinger, P. D. 1977, A&A, 57, 407

—. 1978, ApJS, 36, 259

Nomoto, K. 1982, ApJ, 253, 798

Oda, T., Hino, M., Muto, K., Takahara, M., & Sato, K. 1994, Atomic Data and Nuclear Data Tables, 56, 231

Paczyński, B., & Ziółkowski, J. 1968, AcA, 18, 255

Paquette, C., Pelletier, C., Fontaine, G., & Michaud, G. 1986a, ApJS, 61, 177

—. 1986b, ApJS, 61, 197

Paxton, B., Bildsten, L., Dotter, A., et al. 2011, ApJS, 192, 3

Paxton, B., Cantiello, M., Arras, P., et al. 2013, ApJS, 208, 4

Paxton, B., Marchant, P., Schwab, J., et al. 2015, ApJS, 220, 15

—. 2016, ApJS, 223, 18

Paxton, B., Schwab, J., Bauer, E. B., et al. 2018, ApJS, 234, 34

Paxton, B., Smolec, R., Gautschy, A., et al. 2019, arXiv e-prints, arXiv:1903.01426 [astro-ph.SR]

Pelletier, C., Fontaine, G., Wesemael, F., Michaud, G., & Wegner, G. 1986, ApJ, 307, 242

Piersanti, L., Cassisi, S., & Tornambé, A. 2001, ApJ, 558, 916

Piro, A. L. 2015, ApJ, 801, 137

Pols, O. R., Tout, C. A., Eggleton, P. P., & Han, Z. 1995, MNRAS, 274, 964

Potekhin, A. Y., & Chabrier, G. 2010, Contributions to Plasma Physics, 50, 82

Potekhin, A. Y., Chabrier, G., & Rogers, F. J. 2009, PhRvE, 79, 016411

Raddi, R., Gänsicke, B. T., Koester, D., et al. 2015, MNRAS, 450, 2083

Raddi, R., Hollands, M. A., Gänsicke, B. T., et al. 2018a, MNRAS, 479, L96

Raddi, R., Hollands, M. A., Koester, D., et al. 2018b, ApJ, 858, 3

—. 2019, arXiv e-prints, arXiv:1902.05061 [astro-ph.SR]

Rafikov, R. R. 2011a, ApJL, 732, L3

—. 2011b, MNRAS, 416, L55

Ranganathan, S., Johnson, R., & Woodward, C. 2003, Physics and Chemistry of Liquids, 41, 123

Ritter, H. 1988, A&A, 202, 93

Rogers, F. J., & Nayfonov, A. 2002, ApJ, 576, 1064

Rohrmann, R. D., Althaus, L. G., García-Berro, E., Córsico, A. H., & Miller Bertolami, M. M. 2012, A&A, 546, A119

Roussel-Dupré, R. 1981, ApJ, 243, 329

Saumon, D., Chabrier, G., & van Horn, H. M. 1995, ApJS, 99, 713

Schatzman, E. 1945, Annales d'Astrophysique, 8, 143

—. 1948, Nature, 161, 61

Schwab, J., Quataert, E., & Bildsten, L. 2015, MNRAS, 453, 1910

Schwab, J., Quataert, E., & Bildsten, L. 2016, MNRAS, 458, 3613

Sengupta, S., & Garaud, P. 2018, ApJ, 862, 136

Shaffer, N. R., Baalrud, S. D., & Daligault, J. 2017, PhRvE, 95, 013206

Shen, K. J., & Bildsten, L. 2009, ApJ, 699, 1365

—. 2014, ApJ, 785, 61

Shen, K. J., Boubert, D., Gänsicke, B. T., et al. 2018, ApJ, 865, 15

Soraisam, M. D., Bildsten, L., Drout, M. R., et al. 2018, ApJ, 859, 73

Spitzer, L. 1962, Physics of Fully Ionized Gases (Interscience Publishers, New York)

Stanton, L. G., & Murillo, M. S. 2016, PhRvE, 93, 043203

Thoul, A. A., Bahcall, J. N., & Loeb, A. 1994, ApJ, 421, 828

Timmes, F. X., & Swesty, F. D. 2000, ApJS, 126, 501

Timmes, F. X., Townsend, R. H. D., Bauer, E. B., et al. 2018, ApJL, 867, L30

Traxler, A., Garaud, P., & Stellmach, S. 2011, ApJL, 728, L29

Tremblay, P.-E., Ludwig, H.-G., Freytag, B., et al. 2015, ApJ, 799, 142

Tremblay, P.-E., Ludwig, H.-G., Freytag, B., Koester, D., & Fontaine, G. 2017, MmSAI, 88, 104

Tremblay, P.-E., Ludwig, H.-G., Steffen, M., & Freytag, B. 2013, A&A, 559, A104

van Lieshout, R., Kral, Q., Charnoz, S., Wyatt, M. C., & Shannon, A. 2018, MNRAS, 480, 2784

Vanderburg, A., Johnson, J. A., Rappaport, S., et al. 2015, Nature, 526, 546

Vauclair, G., Vauclair, S., & Greenstein, J. L. 1979, A&A, 80, 79

Vauclair, S., & Théado, S. 2012, ApJ, 753, 49

Vennes, S., Kawka, A., & Németh, P. 2011a, in American Institute of Physics Conference Series, Vol. 1331, American Institute of Physics Conference Series, ed. S. Schuh, H. Drechsel, & U. Heber, 246

Vennes, S., Kawka, A., & Németh, P. 2011b, MNRAS, 413, 2545

Veras, D. 2016, Royal Society Open Science, 3, 150571

Wachlin, F. C., Vauclair, G., Vauclair, S., & Althaus, L. G. 2017, A&A, 601, A13

Winget, D. E., Kepler, S. O., Campos, F., et al. 2009, ApJL, 693, L6

Woosley, S. E., & Kasen, D. 2011, ApJ, 734, 38

Woosley, S. E., & Weaver, T. A. 1994, ApJ, 423, 371

Wyatt, M. C., Farihi, J., Pringle, J. E., & Bonsor, A. 2014, MNRAS, 439, 3371

Xu, S., Jura, M., Koester, D., Klein, B., & Zuckerman, B. 2014, ApJ, 783, 79

Yoon, S.-C., & Langer, N. 2004a, A&A, 419, 645

—. 2004b, A&A, 419, 623

Yoon, S.-C., Langer, N., & Scheithauer, S. 2004, A&A, 425, 217

Zuckerman, B., Koester, D., Melis, C., Hansen, B. M., & Jura, M. 2007, ApJ, 671, 872

Zuckerman, B., Koester, D., Reid, I. N., & Hünsch, M. 2003, ApJ, 596, 477